ABSTRACT

Title of Dissertation: INVESTIGATION OF AMORPHOUS HYDROGENATED Si AS A RESIST FOR VACUUM-COMPATIBLE LITHOGRAPHY OF HgCdTe/CdTe FILMS

Randolph Nicholas Jacobs,
Doctor of Philosophy, 2005

Dissertation directed by: Professor Lourdes Salamanca-Riba,
Department of Materials Science and Engineering

The vision of achieving a completely in-vacuum process for fabricating HgCdTe Infrared detector arrays is contingent on the availability of a vacuum-compatible lithography technology. One such technology for vacuum-lithography involves the use of amorphous hydrogenated Si (a-Si:H) as a dry photoresist. The basic concept has recently been demonstrated whereby a-Si:H resists were deposited via plasma enhanced chemical vapor deposition (PECVD), and then patterned using an excimer laser. The patterns were then hydrogen plasma developed to remove unirradiated areas. Finally, an Ar/H_2 electron cyclotron resonance (ECR) plasma was used to transfer patterns to underlying $Hg_{1-x}Cd_xTe$ film layers.

This thesis presents a continued investigation of a-Si:H as a resist material wherein the resists are deposited using an Ar-diluted silane precursor. To determine the best conditions for the technique, the effects of different laser fluences, and exposure environments were studied. Analysis via transmission electron microscopy (TEM) reveals that the excimer-exposed surfaces are polycrystalline in nature,

indicating that the mechanism for pattern generation in this study is based on melting and crystallization of the exposed areas. To reduce undesirable surface roughness induced by laser irradiation, a step-wise crystallization/dehydrogenation technique is demonstrated. Fundamental aspects of pattern transfer (via ECR plasma etching) to CdTe and HgCdTe films are also demonstrated, where etch selectivities of 8:1 and 16:1 (respectively) are observed. These values represent a significant improvement to etch selectivities obtained using commercially available organic resists. To address concerns regarding possible damage to HgCdTe caused by the a-Si:H dry lithography process, preliminary studies were carried out using double-crystal rocking curve X-Ray diffraction and high-resolution TEM. The results indicate no evidence of microstructural damage to the HgCdTe film. Other characterization techniques used throughout this thesis include Fourier transform infrared spectroscopy (FTIR), scanning electron microscopy (SEM), and stylus profilometry.

The implementation of the a-Si:H dry lithography process represents a crucial step toward achieving totally integrated fabrication of HgCdTe IR detector arrays. In addition this lithography technique is both low temperature and contamination-free, so that other semiconductor microfabrication processes could potentially benefit from its use.

INVESTIGATION OF AMORPHOUS HYDROGENATED Si AS A RESIST FOR VACUUM-COMPATIBLE LITHOGRAPHY OF HgCdTe/CdTe FILMS

By

Randolph Nicholas Jacobs

Dissertation submitted to the Faculty of the Graduate School of the
University of Maryland, College Park, in partial fulfillment
of the requirements for the degree of
Doctor of Philosophy
2005

Advisory Committee:
Professor Lourdes Salamanca-Riba, Chair
Dr. John H. Dinan
Professor Chris Lobb
Associate Professor Luz Martinez-Miranda
Associate Professor Isabel K. Lloyd

Dedication

To my loving children Jackson and Rhaya,
whose joyous laughter has lifted my spirits even
after the most difficult days.

Acknowledgements

First I acknowledge my Advisor Dr. Lourdes Salamanca-Riba, for the expert advice and direction she has provided during my graduate career. Her encouragement has been extremely important, particularly in my decision to pursue a Ph.D. degree. I am also grateful for the initial training and assistance I've received from past members of my Graduate Advisor's electron microscopy research group; Ying-Hai Li, Chris Kang, Wendy Sarney, Hao Li and technician, Tim Zhang. I thank University of Maryland Professors, Dr. Lobb, Dr. Martinez-Miranda, and Dr. Lloyd for serving on my committee and for providing useful suggestions on my dissertation.

I am most grateful for the opportunity I've been given by the U.S. Army Night Vision & Electronic Sensors Directorate (NVL), through which I've performed most of my PhD research. Dr. Jack H. Dinan (at NVL) has been an excellent advisor and mentor, and I've admired and been inspired by his constant enthusiasm and positive attitude towards this project. My deepest appreciation also goes to Andy Stoltz who has served as a patient teacher, mentor, collaborator and a trusting friend. He not only provided training, but is also responsible for the ECR work in this thesis. Special thanks also to Ernest Robinson for his important contributions during the two summers he interned at NVL and worked on this project. Other NVL collaborators include Dr. Tony Almeida (II-VI growth), and Justin Markunas (XRD). I also extend my appreciation to collaborators at the Army Research Laboratory; Phil Boyd (SEM/EDX), Unchul Lee and Jay C. Molstad (AES). Phil Boyd with his extensive knowledge of numerous materials characterization techniques, has been an enormous inspiration to myself and many underrepresented minorities in the sciences. NVL personnel including; John Varesi, Dr. M. Martinka, Dr. J.D. Benson, Dr. L. Bubulac, Dr. K. McCormack, Andy Kaleczyc and Dr. W. Mason are experts in the IR technology field and have also contributed to this work through helpful suggestions. I also acknowledge Ed Smith of Raytheon Vision Systems for helpful discussions. Finally, I am thankful for technical support from NVL's Ken Brogden and Jerry Bratton.

Of course, special thanks goes to my beautiful and incredibly intelligent wife for her constant support and sacrifice particularly while writing this dissertation. I also thank my wonderful parents and family for unconditional support throughout all the good, and not so good decisions I've made in the past. My dearest friends (they know who they are) have also been extremely helpful in providing different perspectives and social outlets when I most needed them.

Last but certainly not least I thank my Lord and Savior for physical and mental health, without which none of this would have been possible.

Table of Contents

List of Tables

List of Figures

Chapter 1

Introduction and Background

1.1 Fabrication of HgCdTe Focal Plane Arrays

Over the past 40 years, infrared focal plane arrays (FPAs) have seen substantial use particularly for astronomy and military applications. NASA for example, has used infrared FPAs for earth satellite missions, and attention has also been placed on monitoring long-term changes in climate [1]. The military has long recognized that infrared (IR) sensing provides critical tactical advantages on the battlefield. The need for a detection and identification range in excess of an adversary's has helped to propel three generations of IRFPA devices [2].

FPAs have a hybrid structure, consisting of a detector array mated to a read out integrated circuit (ROIC) multiplexor. The detector is essentially an array of IR absorbing pixel elements on an IR transparent substrate. Figure 1.1 shows the basic architecture for a detector array and also indicates the major process steps carried out during its fabrication. The hybrid FPA device is then constructed by cold welding the individual elements of the detector array to an ROIC multiplexor array (not shown). The pixel elements are semiconductor photovoltaic diodes and so the choice of IR absorber material is most crucial to device performance.

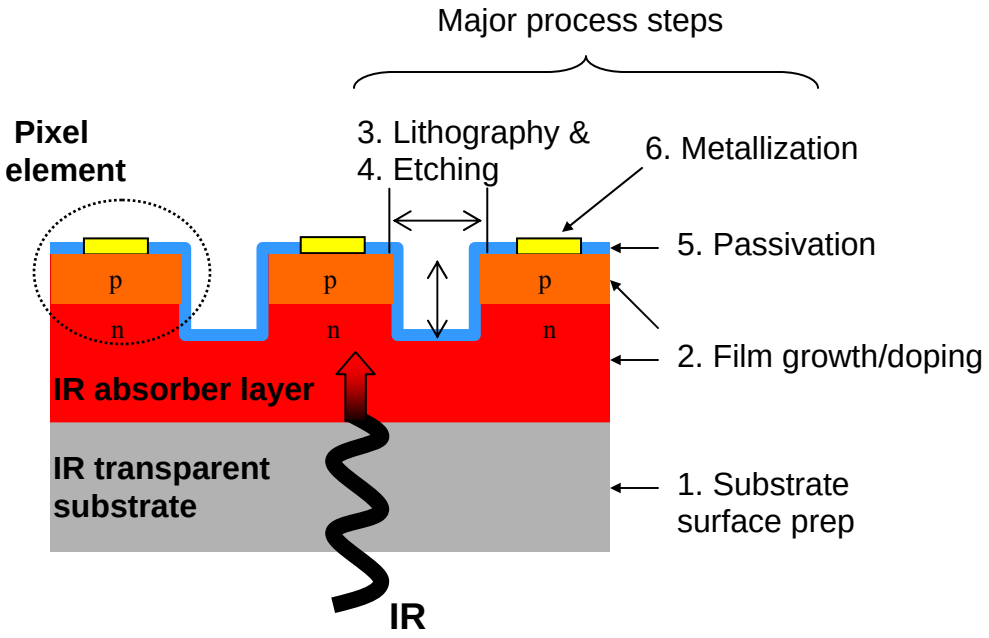

Figure 1.1: Simplified cross-sectional view illustrating the basic architecture of an IR detector array. The IR absorber layer must be reticulated (via lithography and etching) to define and isolate photovoltaic pixel elements. After the major process steps are carried out, the individual pixels are mated to a ROIC array via cold-welding (not shown).

For IRFPA technology, the $Hg_{1-x}Cd_xTe$ material system has had an enormous impact [1,3,4]. By varying the composition (x value), the band gap can be tuned continuously from 1.6 eV (high x value) to 0 eV (low x value) [1,5,6], making it possible to design sensors for detection in the near IR (~0.7 μm) to the long wavelength IR (LWIR) region (>25 μm). In addition, HgCdTe offers strong optical absorption and a quantum efficiency (number of carriers generated per incident photon) of near 80% at 77 K. Though several competing sensor technologies exist, experts in the field agree that HgCdTe is the most versatile and efficient detector of IR radiation and will likely continue to dominate as the material of choice for next generation high performance IR imaging systems [7].

There are however, several limitations of HgCdTe that prevent it from competing with other materials particularly for low-end IR detection. These are: 1) As with many ternary compounds, it is difficult to control the doping and composition of the material during film growth. 2) The choice of substrate has also been a major issue. The detectors are backside illuminated, so in addition to lattice and thermal mismatch, the substrates must also be transparent to the IR wavelength for which the detector is to be used. The substrate of choice, particularly for mid-wavelength (MWIR) and LWIR detectors has been CdZnTe [8]. However these substrates are extremely fragile, expensive, and available only in small wafer sizes [9,10]. 3) HgCdTe, (even more so than other II-VI materials) is very soft and very brittle. The extra care and precision required for processing of such a fragile material leads to relatively low yield. 4) Finally, HgCdTe is extremely sensitive to damage and contamination as a consequence of its very small band gap (under 0.1 eV for LWIR material).

Despite the limitations described above, HgCdTe research continues, and progress in the industry has been made [11]. This is largely due to the demanding requirements of next generation high-resolution "two-color" IR focal plane arrays (FPA). For one, the advent of molecular beam epitaxy has provided better composition and doping control than was previously obtainable through liquid phase techniques [9,12-15]. Alternative substrate systems have also been demonstrated, the most notable of which is CdTe/Si (CdTe buffer layers on Si substrates). Using novel growth techniques, HgCdTe has been epitaxially grown on CdTe/Si(211) substrates, despite an unprecedented 19% lattice mismatch [16-18]. Advantages are gained due

to the availability of low-cost, large-format Si substrates, and also because of the low thermal mismatch to Si read out integrated circuits (ROIC), to which the detector is eventually mated.

In general, difficulties encountered in materials handling can be abated by switching from wet to dry processing [19]. Dry processing reduces both wafer handling and contamination, because process steps are performed in vacuum environments. In particular, the microelectronics industry has seen tremendous improvements in etching due to the implementation of dry processing [20]. Etching is a crucial step that is performed to both define and isolate detector elements or "pixels" by the selective removal of material. Proper isolation of pixels is necessary to suppress spectral crosstalk, which occurs when photogenerated carriers in one detector element diffuse to adjacent elements in the array. Thus, without proper pixel isolation, the image clarity and overall system performance of a detector array is dramatically degraded [21].

Conventional etch processes for HgCdTe IR FPAs are performed by first spin coating a polymer film (known as photoresist) onto the wafer. After baking the film to volatize excess organics, a pattern is generated by ultraviolet (UV) irradiation through a patterned mask. The creation of a pattern on the film by UV (or by other means) is known as lithography. For the "positive tone" resists typically used, UV radiation alters the film, making it soluble in a chemical developer solution used to selectively remove the irradiated portions. This step is known as development. In the subsequent etching step, a chemical solution (such as bromine-methanol) is used to remove a certain thickness of the underlying II-VI film. It is during this last step

(also known as pattern transfer) that dry etching techniques have made the most impact [22]. Conventional wet-etching is essentially an isotropic process in that material is removed in all directions at the same rate. This is problematic for applications that require deep isolation trenches between pixels, in that pixel area is drastically reduced as etching progresses. By taking advantage of highly anisotropic etch mechanisms, dry plasma etching has been used here to preserve pixel area even while producing deep trenches in the film [22-24]. The use of plasma etching also averts the problem of possible contamination from organics used during wet etching. It is therefore expected that in addition to smaller and denser pixel arrays, dry etching will lead to higher manufacturing yield.

The potential advantages of dry processing have influenced an integrated approach to HgCdTe detector array fabrication, which has now been pursued for some 20 years [25]. As was indicated in Figure 1.1, the major process steps for the detector array include:

1-Substrate surface preparation
2-Film growth
3-Lithography
4-Etching
5-Passivation
6-Metallization

At the Night Vision and Electronic Sensors Directorate (NVESD), technologies have been developed for progression towards the ultimate goal of all-vacuum processing. For example, plasma-based surface preparation of CdZnTe substrates for HgCdTe epitaxy has been demonstrated [26]. For growth on Si substrates (see above), separate CdTe and HgCdTe MBE growth chambers have been integrated onto a vacuum transfer line along with advanced spectroscopic equipment for in-vacuo

surface analysis. Also attached to the transfer line is an electron cyclotron resonance (ECR) plasma reactor for anisotropic etching of films after lithographic patterning with polymer resists. Thus, except for lithography, steps 1 through 4 can already be performed in vacuum. Passivation (step 5) refers to the deposition of a thin CdTe layer to protect the HgCdTe surface, and metallization (step 6) refers to the deposition of a contact metal to pixel surfaces for subsequent mating to a read out circuit. In principle, in-situ techniques for steps 5 & 6 exist, but require further development. These steps will not be addressed here. On the other hand, a novel vacuum compatible lithography technology (for step 3) has recently been demonstrated using an inorganic resist material, [27]. This subject is the focus of this dissertation.

1.2 Selection of a-Si:H as a vacuum compatible photoresist

A resist material for a viable vacuum compatible lithography process must meet several key requirements. First, the material itself must be vacuum compatible. That is, it should have a sufficiently low vapor pressure to prevent vaporization under high vacuum conditions. However, vapor phase processes must be utilized to carry out both deposition and etching. A mechanism must also be found, by which irradiation of the as-deposited material alters the surface such that subsequent etching takes place at a very different rate. The ratio of the two different etch rates is termed "etch-selectivity" [28], and higher values are generally desirable. This establishes a means to lithographically generate and develop patterns in the material. It is also necessary that the developed material withstand the existing plasma etch process for pattern transfer to the underlying film. In our case the underlying films are HgCdTe

and/or CdTe, which are very difficult materials to work with. Namely, HgCdTe has been known to degrade/decompose at temperatures above 80 ºC. Finally, the chosen resist material and all of the associated process steps should not degrade the quality of the final product.

Amorphous hydrogenated Si (a-Si:H) was originally selected as a dry resist in this project for several reasons. Firstly, it is easily and cheaply deposited over large areas via plasma-enhanced chemical vapor deposition (PECVD). In addition, a-Si:H is known to oxidize under exposure to UV radiation [27,29,30]. A method for lithographically defining patterns is then made possible by achieving different removal rates for a-Si:H and the UV induced oxide (SiO_x) during subsequent development-etching. Furthermore, the use of PECVD allows for low-temperature deposition and removal processes [31], so that thermal degradation of HgCdTe and/or other underlying film layers can be avoided. These factors make a-Si:H an excellent choice for use as a vacuum-compatible resist.

Other researchers have investigated the use of organosilicon polymers for use as a dry resist [32-34]. The polymers are deposited via PECVD from precursors such as methylsilane (CH_3SiH_3). Exposure to 248 nm UV light causes oxidation of the polymer such that development etch selectivities up to 5:1 can be obtained during subsequent Cl_2 plasma etching.

Amorphous Si resists offer key advantages over organosilicon polymers. Namely, silane gas is used as the deposition precursor and pure H is used during development-etching. Thus, the possibility of contamination from organics is virtually eliminated since they are not used during processing. Silane is also

significantly less expensive than organosilanes. This makes a-Si:H more attractive from a manufacturing standpoint, given that resists are supposed to be consumable materials.

1.3 Proof of concept

The laboratory of Materials Research Group Inc. (MRG) previously reported the feasibility of a vacuum-compatible lithography process based on a-Si:H photoresists [27]. The process flow diagram in Figure 1.2 illustrates the procedure used during this proof of concept. For comparison, the conventional wet lithography procedure is also illustrated. Using an undiluted silane source gas, a-Si:H was deposited on HgCdTe epilayers via PECVD (step 1). Following deposition, the wafer was transferred in vacuum to a second chamber where a projected mask pattern was created on the a-Si:H surface through exposure to a KrF excimer laser (step 2). Prior to laser exposure, an oxygen-containing ambient was established to allow oxidation of the exposed regions. After transferring the substrate back to the PECVD chamber, the laser-generated pattern was developed in a pure hydrogen plasma (step 3), where etch selectivities of at least 500:1 were reported for unexposed and exposed regions. The resulting a-Si:H mask was used to create mesas in the underlying HgCdTe epilayers, by etching in an electron cyclotron resonance (ECR) plasma reactor (step 4). The ECR plasma parameters were chosen to completely strip the a-Si:H photoresist, while etching approximately 2.5 μm deep mesas into the HgCdTe.

Devices were fabricated at NVESD using a crude 8 X 8 array of mesas. Metallization was performed using conventional (wet-chemical) photolithography, and I-V curves were measured at 77 K using manual probes. While good I-V

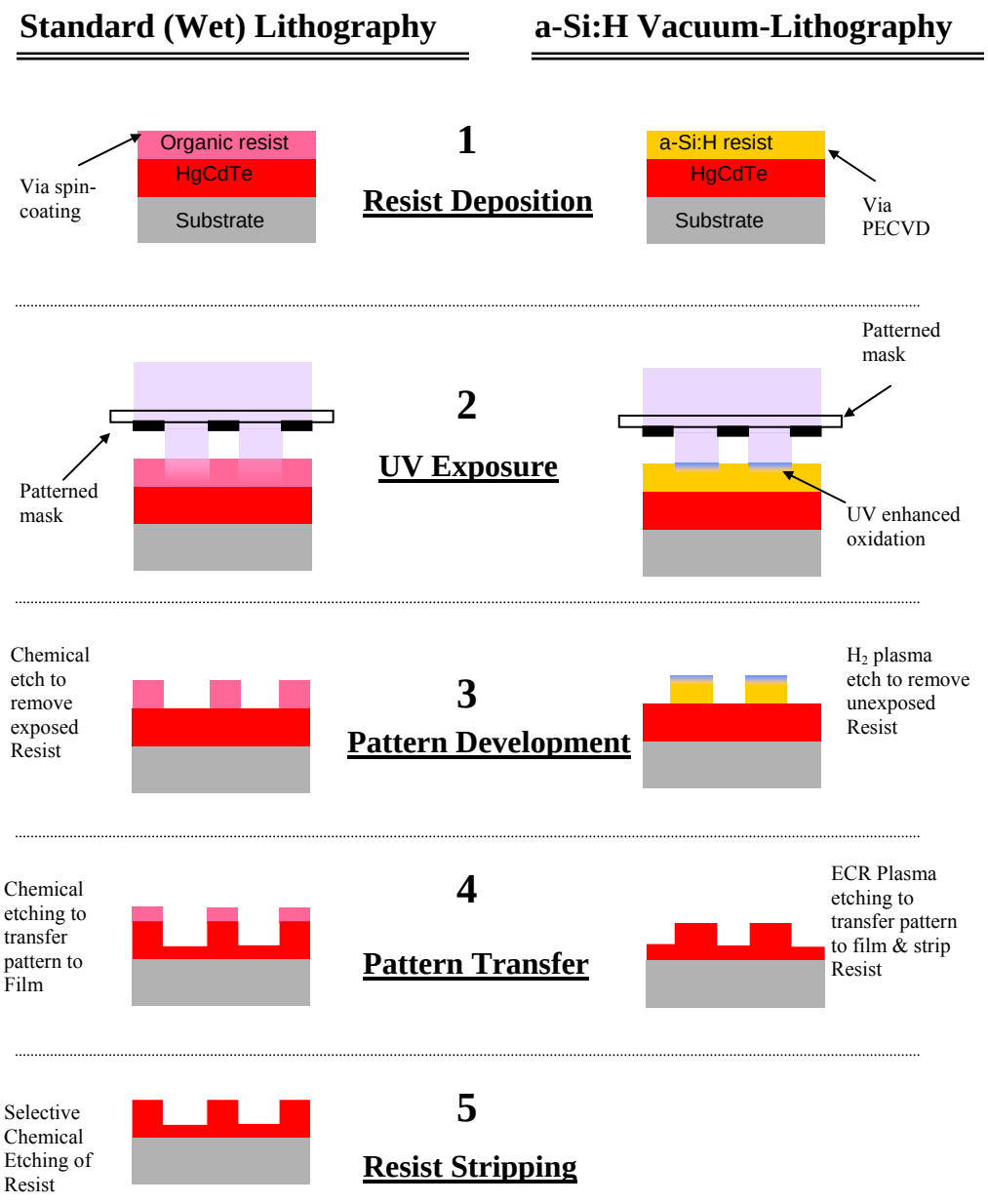

Figure 1.2: Process steps for standard lithography (left), and a-Si:H vacuum-lithography (right). A proof of concept for the a-Si:H vacuum-lithography procedure was carried out by Hollingsworth et al [27].

characteristics were obtained, the R_0A value (junction resistance at zero bias) was below state of the art for the HgCdTe material used. The authors attributed these results to a lack of passivation of the mesa sidewalls and to the immaturity of the device fabrication process at NVESD. Nonetheless, the results demonstrated a working device and the technology was thought to be so promising for detector array fabrication that a similar module was attached to the HgCdTe device processing line at NVESD. The addition of this equipment made possible a true wafer-in, array-out method for the fabrication of HgCdTe detector arrays (see Figure 1.3 below). Further experimentation and technology development were needed to determine the usefulness of a-Si:H vacuum-compatible lithography [27], and for the potential transitioning of this technology to an industrial process.

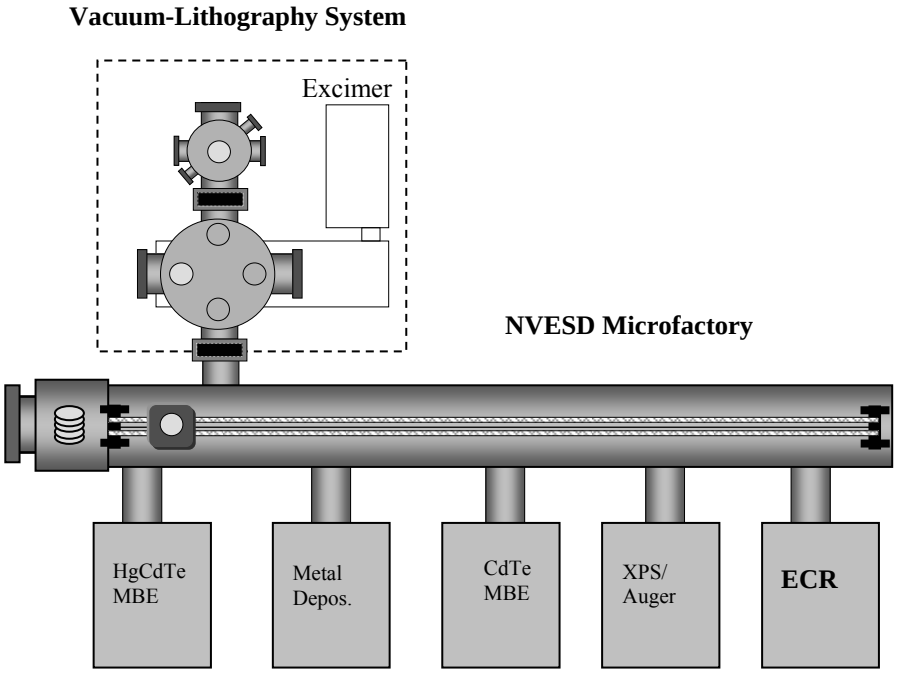

Figure 1.3: Integration of vacuum-lithography system with the NVESD vacuum processing line (Microfactory). The addition of this equipment makes possible a true "wafer in – array out" method for HgCdTe detector array fabrication.

1.4 Contribution and Motivation of present study

This thesis presents a continued investigation of a-Si:H as a resist material for use in a novel vacuum-compatible lithography technique. Certain changes had been incorporated into the new system installed at NVESD (in 1998), in order to improve upon the original design. Namely, an argon-diluted silane precursor (instead of pure silane) was used for deposition in efforts to suppress the creation of Si dust which results from gas phase reactions taking place within the plasma. In addition, silane is extremely flammable, so dilution of the source gas also mitigated safety concerns. As we will show in chapter 3 however, the solution to one problem can create others. In essence we demonstrate a pattern generation mechanism based on laser crystallization, in contrast to the "UV enhanced oxidation" mechanism originally used during the proof of concept. In chapter 4 we attempt to understand the origins of, and to suppress surface roughness induced by the laser irradiation process. The knowledge gained here is applied in chapter 5 where pattern transfer to CdTe and HgCdTe films is performed via ECR plasma etching. Key etch characteristics of the a-Si:H resists are also compared to conventional organic resists. Finally, chapter 6 discusses the effects of the a-Si:H lithography process on the HgCdTe near surface. While chapter 6 does not cover all aspects of process induced changes, the results do address the potential for structural damage.

Various characterization techniques are carried out during this study. These include surface profilometry, transmission and scanning electron microscopy, Fourier transform infrared spectroscopy and auger electron spectroscopy. A brief review of

these techniques and their specific use in this work are given in chapter 2, in addition to details of experimental/fabrication methods.

The results presented in this thesis were crucial in advancing the current understanding of the a-Si:H vacuum-lithography technique for patterning of CdTe based semiconductors. While possible obstacles such as surface roughness are elucidated, solutions are proposed and studied to examine their feasibility. It should be noted that the realization of an all-vacuum fabrication technique for HgCdTe detector arrays will depend on several process steps and in turn, many inter-related factors. However, the dry lithography process is an important and necessary step to achieving this ultimate goal. The potential advantages of a complete high vacuum processing line may include less surface contamination, and higher manufacturing yield [35]. This could in turn, lead to the realization of more complex structures and increased device performance. Furthermore, the a-Si:H vacuum-lithography technique need not be limited to the manufacture of HgCdTe detector arrays. Due to low process temperatures and the elimination of organics, the technique could potentially be used during device fabrication of other semiconductors as well. The changes would mainly involve finding plasma etch chemistries (for pattern transfer) that are suitable to that particular material.

Chapter 2

Experimental Methods

2.1 MBE Growth of HgCdTe and CdTe

Thin film growth of all II-VI semiconductor materials used throughout this work was carried out via molecular beam epitaxy (MBE). During the growth process evaporated beams of atoms from one or more sources are directed at a crystalline surface within an ultrahigh vacuum (UHV) environment with 10^{-10} Torr base pressures. Independent control of beam fluxes, source temperatures, and other deposition conditions allow for fabrication of semiconductor heterostructures at an atomic level [36]. This gives MBE a distinct advantage over other growth techniques such as liquid phase epitaxy (LPE). Particularly for HgCdTe epitaxial film growth, composition and doping control is achieved through precise monitoring of the growth parameters mentioned above [9,37,38].

In this work, two MBE systems (connected via high-vacuum transfer line) were used for II-VI semiconductor film growth. Deposition took place on three-inch Si(211) substrates that were pretreated ex-situ. Si(211) is the substrate of choice for next generation IRFPAs due to their low cost and high availability compared to CdZnTe. Prior to deposition, Si wafers were mounted on indium-free molybdenum substrate holders and then hydrogen passivated using an HF spin-etch procedure [39,40]. After introduction into the UHV chamber, the wafers were then heated to

~540 °C to desorb the passivating hydrogen. The molecular and elemental sources in the MBE system are housed in isothermal cavities known as "effusion cells", which are arranged around the substrate. The use of Si substrates in this work, necessitated the growth of an initial ZnTe buffer layer prior to growth of subsequent layers of CdTe and/or HgCdTe. ZnTe exhibits a 12.3% lattice mismatch with Si, compared to 19.3% for CdTe on Si. Thus, an initial ZnTe layer results in better nucleation on the Si surface. This ~ 300 Å thick layer is grown using a technique known as migration enhanced epitaxy (MEE), where the growth procedure is performed by alternating Zn and Te_2 fluxes with the substrate held at 250 °C. This method is thought to promote a 2-dimensional growth mode, while minimizing the generation of growth defects [41].

Subsequent CdTe epitaxy is carried out using a compound CdTe effusion cell. Here several layers are grown at different temperatures with a 370 °C one minute annealing step between each layer. This procedure is used to filter threading dislocations from the underlying ZnTe/Si interface. The dislocations interact with each other due to thermal stresses between each layer, and thus become localized at the interfaces [41]. A typical growth procedure results in a total CdTe thickness of ~10 μm with growth rates of ~1 μm/hr.

Other experiments in this work involve the deposition of $Hg_{1-x}Cd_xTe$ following CdTe film growth. HgCdTe epitaxy took place in a separate MBE system (connected via the NVESD-microfactory) with standard CdTe and Te effusion cells and a customized Hg cell. A simplified schematic of this particular system is shown in Figure 2.1. In-situ characterization techniques employed during growth, include reflection high energy electron diffraction (RHEED), and spectroscopic ellipsometry

(SE). RHEED was used to assess the crystalline quality of the growing film. A < 20 KV electron beam was directed at the film surface at a very low angle and a phosphor screen collected the reflected intensity. Here, a streaky diffraction pattern is indicative of smooth 2-dimensional film growth, while a spotted diffraction pattern results from undesirable three-dimensional or island-like growth [42]. The SE apparatus is attached to the HgCdTe MBE system as it allows for highly precise in-situ monitoring of composition and substrate temperature through a modeling technique [43]. The method has been successfully used to measure *x* values in the range ($0.16 < x < 0.6$), which correspond to short, mid, and long-wavelength IR-sensitive $Hg_{1-x}Cd_xTe$ material. A detailed description of the SE apparatus and specifics regarding the monitoring technique are discussed elsewhere [43,44]. HgCdTe MBE was carried out using a modified Fisons VG-80 chamber.

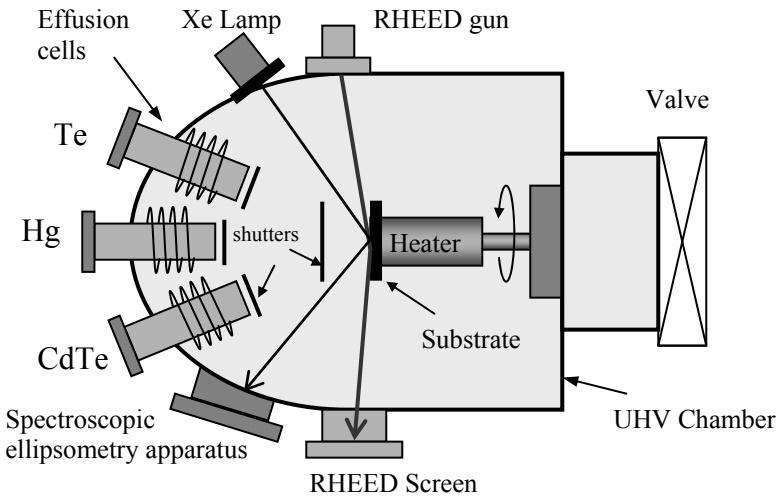

Figure 2.1: Schematic diagram of the MBE chamber for HgCdTe thin film deposition. RHEED and Spectroscopic ellipsometry were used to monitor crystalline quality and composition of the growing film.

2.2 Plasma processing of a-Si:H

Amorphous hydrogenated silicon (a-Si:H) was deposited and removed using plasma-enhanced chemical vapor processes. Over the past few decades, the use of plasma processes in semiconductor device manufacturing has been greatly increased due to several advantages over standard wet chemical and chemical vapor processes. For instance, highly anisotropic profiles (which are necessary for reduction in feature sizes) are obtained by plasma etching techniques. In addition, the use of plasmas allows many films to be deposited at much lower temperatures than would be required by conventional chemical vapor deposition (CVD) [19]. For the purposes of this study, the latter point is most crucial in that a low-temperature deposition technique was needed to avoid thermal degradation of the underlying films.

The plasma itself is a radio frequency (rf) driven, low-pressure glow discharge consisting of randomly moving electrons, ions, and neutrals. The fractional ionization x_{iz}, in the plasma can be described by,

$$x_{iz} = \frac{n_i}{n_g + n_i} \tag{2.1}$$

where n_g and n_i are respectively, the neutral and ionized gas densities. For low-pressure glow discharges, $x_{iz} << 1$, in contrast to high pressure plasmas such as stars and most interstellar matter. Thus, the plasma is only weakly ionized and its constituent species are not in thermal equilibrium. Preferential heating of the electrons occurs so that the "electron temperature" (T_e) is much greater than that of the more massive ions. That is, $T_e >> T_i$. This fact is responsible for the thin positively charged layer near the substrate surface called a plasma *sheath*, which is

characteristic of all laboratory plasma processes. Though $n_i \approx n_e$ (where n_e is the electron density), the enormous difference in mass leads to much higher thermal velocities for electrons compared to ions. On a short timescale, the fast-moving electrons are lost rapidly to a grounded surface so that a thin layer results near the surface where $n_i >> n_e$. This causes a net charge density, which gives rise to a dc-bias despite the fact that the plasma is driven by an alternating (rf) source. Ions that enter the sheath from the plasma are accelerated into the surface and deposition or etch processes occur [45]. In this study, both deposition and etching of a-Si:H were carried out using a parallel plate radio frequency (rf) plasma reactor or *rf diode*.

2.2.1 Growth of a-Si:H via PECVD

In the absence of a plasma, silane readily decomposes at temperatures above approximately 450 ºC allowing for Si deposition via standard chemical vapor deposition, (CVD). However, the low deposition temperatures necessary for this work required the use of a plasma to dissociate the silane molecule [31]. A-Si:H films were deposited via plasma decomposition of silane gas (SiH_4) using a custom-built plasma-enhanced chemical vapor deposition (PECVD) system operated at 13.56 MHz. Figure 2.2 shows a schematic diagram of the PECVD system used for a-Si:H deposition. The system uses a capacitively coupled, parallel plate electrode arrangement where the substrate sits on the ground electrode. It should be noted that the substrate faces down in this configuration, to reduce particulate contamination from material flaking off the chamber walls. Base pressures of 10^{-9} Torr are achieved in the copper-sealed PECVD chamber using a turbomolecular pump backed by a

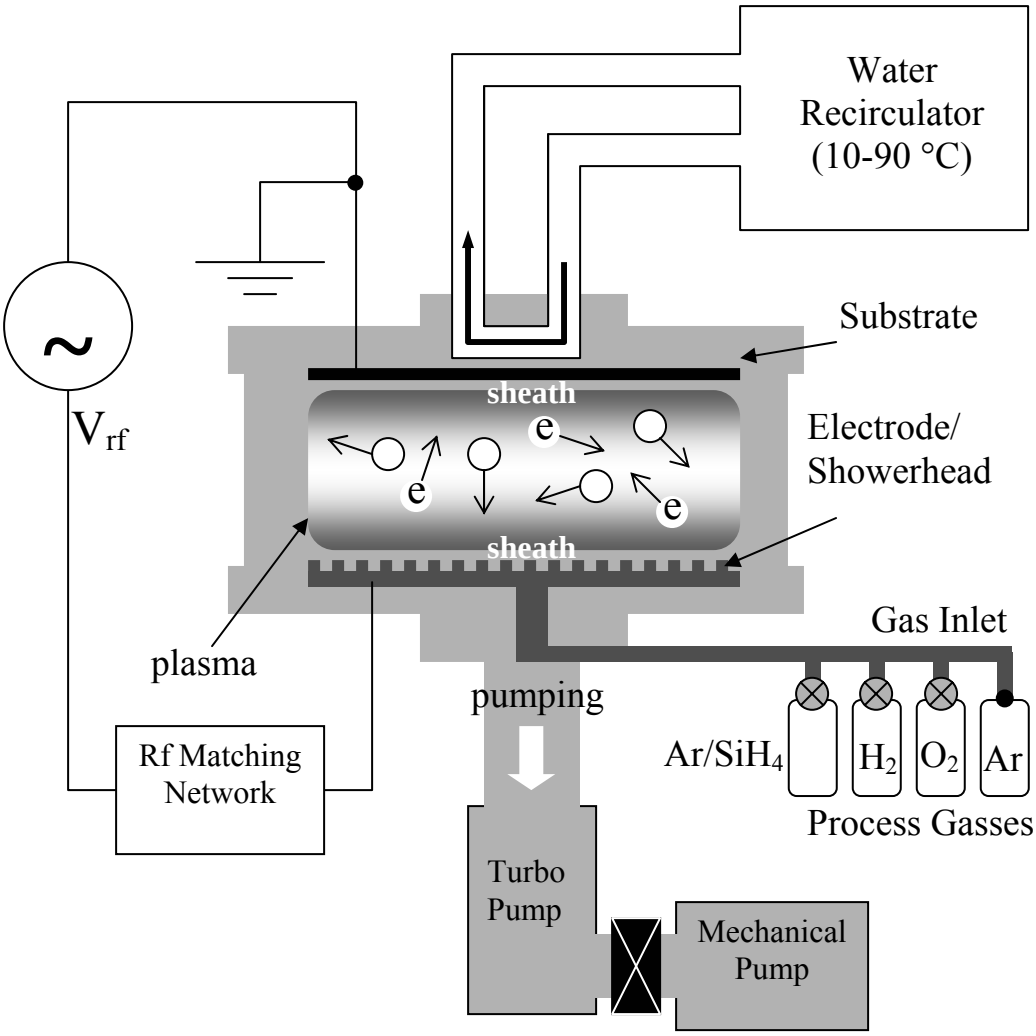

Figure 2.2: Schematic of PECVD reactor used for deposition of a-Si:H films. Hydrogen plasma etching is also carried out in the reactor (see section 2.2.2).

mechanical pump. The process gasses are introduced through a showerhead, which also serves as the powered electrode. The showerhead design allows for deposition uniformity of +/- 5 %, which was sufficient for the experiments performed in this work. The substrate temperature was regulated radiatively using a water recirculator with a range of 10-90ºC. It was therefore necessary to allow sufficient time for the substrate to heat up to the desired temperature (measured using a thermocouple) prior to deposition. A mass flow controller was used to set the desired flow rates of silane entering the reactor chamber.

Various processing parameters must be controlled to grow material with the desired properties and to achieve reasonable deposition rates. While gas flow rates determine the residence time of the gasses in the reactor, the total pressure influences the mean free path for collisions and thus the amount of gas phase reactions. In addition, the rf power controls the rate of gas dissociation and therefore affects the growth rate. Substrate temperature can also influence the growth rate by affecting the rate of chemical reactions at the surface. The influence and interrelationship of these growth parameters are fairly complex, as was demonstrated by several authors [46-48]. For example, under certain gas concentrations the deposition rate peaks at 10 W, and then decreases at higher rf power [47]. This observation (Figure 2.3c) has been explained by depletion effects, whereby the silane is completely consumed by the reaction.

The hydrogen content in the film is also affected by various process parameters. For typical a-Si:H device applications including solar cells and thin film transistors (TFTs), the hydrogen content is important because H acts to suppress

electronic defects. In this case however, a-Si:H is used as a resist material and the role of hydrogen is two fold. First, H passivates the a-Si:H surface against oxidation and thus makes possible the UV enhanced oxidation mechanism for pattern generation (see section 1.3). In addition, the presence of H in a-Si acts to reduce the average coordination number of the Si bonding network, leading to less structural rigidity [49]. This property may be related to the high etch selectivities that are achieved during subsequent development etching (next section). Figure 2.3 also illustrates the dependence of the hydrogen content (in the deposited film) on temperature (a) and rf power (b). The H concentration decreases with increasing growth temperature but seems to peak at a particular rf power [47]. The consideration of defect density (electronically active point defects or macroscopic inhomogeneities), is deemed less important here, since the material is not being used as an active device layer.

The trends observed in Fig 2.3 are due in part to complex chemical and physical processes taking place at the growing surface and within the plasma. Energetic electrons accelerated by the rf discharge collide with gas molecules causing ionization and many possible reactions to occur. For example, excited gas molecules may relax to ground states via emission of visible (or UV) photons giving rise to the characteristic plasma glow. Film growth however, is primarily caused by collisions that result in dissociation of the gas molecules either as neutral radicals or ions. Examples of low energy silane dissociation reactions are as follows [50-52];

$$e + SiH_4 \rightarrow SiH_2 + H_2 + e \quad (2.2)$$

$$e + SiH_4 \rightarrow SiH_3 + H + e \quad (2.3)$$

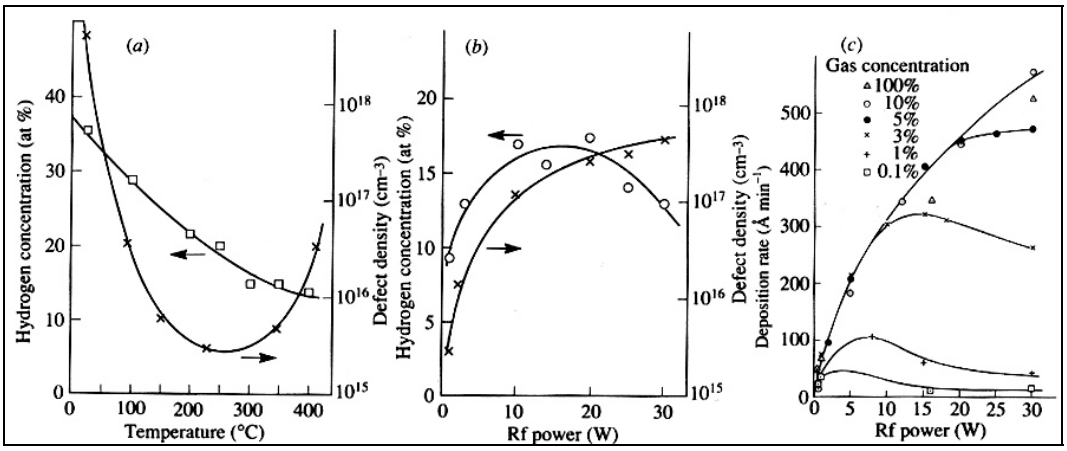

Figure 2.3: Illustration of dependence of material properties on deposition conditions, showing variations of hydrogen concentration and defect density on (a) substrate temperature, and (b) rf power. c) dependence of growth rate on rf power and argon dilution. Reprinted from R.A. Street 1992 [46].

While there are many other possible dissociation reactions, it is commonly believed that SiH_3 and SiH_2 radicals are primarily responsible for film growth under conditions of low rf power [52]. The formation of larger molecules are also possible through reactions such as:

$$SiH_4 + SiH_2 \rightarrow Si_2H_6 \quad (2.4)$$
$$Si_2H_6 + SiH_2 \rightarrow Si_3H_8 \quad (2.5)$$

Larger molecules are generally undesirable since they can interfere with film growth and lead to formation of macroscopic particles. Studies have shown that high rf power promotes macroscopic particles by increasing the fraction of reactive species (neutral radicals or ions) in the plasma [52].

Process parameters in this study were chosen to provide a good balance between growth rate and desired film properties even while meeting strict project requirements. For typical a-Si:H growth, 10% SiH_4 in argon is introduced into the chamber through one of four process gas channels using flow rates of 100 sccm

(standard cubic centimeters per minute). Among other reasons (discussed in chapter 3), the Ar-diluted silane source was utilized for safety concerns, as silane is a particularly hazardous gas that reacts explosively with air or water vapor. Additional argon is introduced into the chamber through a purge line regulated by a needle valve. This additional Ar (~50 mTorr) increases the total flow of process gasses and reduces the residence time of silane in the chamber. A throttle valve is used to maintain an overall chamber pressure of 0.5 Torr for deposition. An rf generator then starts the growth process by initiating the plasma with 3 W rf power (a value chosen to suppress formation of macroscopic particles). The substrate temperature was set at 50 ºC during a-Si:H deposition to both avoid thermal degradation of underlying epilayers and to ensure high H concentrations.

Essential to the growth process is an in situ thickness monitoring technique, which was performed using laser interferometry. A laser beam from a helium-neon source is directed at the growing surface at a glancing angle (approximately 4º), and the reflected signal is measured using a Si photodiode with a 632.8 nm bandpass filter. The beam reflects off the top and bottom surface of the film so that interference occurs. As the film thickness changes, the reflected signal intensity also changes, cycling through constructive and destructive interference. A period of oscillation or fringe spacing (T), is directly proportional to a change in film thickness, Δd where

$$\Delta d = \frac{\lambda}{2n} \approx D\left(\frac{T}{t_p}\right) \tag{2.6}$$

n is the index of refraction of the deposited film, and λ is the wavelength of the laser [53]. It is not practical to measure n however, so Δd was determined by recording the total process time t_p, and measuring the total film thickness D by ex-situ measurement. A value of roughly 100 nm was determined for Δd under typical deposition conditions. Note the number of fringes m, will be equal to t_p/T. Thus, the film thickness during growth can be estimated by,

$$D \approx \Delta d\left(\frac{t_p}{T}\right) = \Delta d(m) \tag{2.7}$$

The fringe spacing T depends on the properties of the growing film but is independent of the substrate. However the starting point of the reflected signal intensity depends strongly on the substrate. The difference in index of refraction between the a-Si:H film and the substrate is directly related to the amplitude of the interference fringes. Thus in some experiments where in-situ film thickness monitoring was crucial, SiO_2/Si substrates were used, as these lead to relatively large interference fringe amplitudes and in turn easily discernable fringes.

2.2.2 Hydrogen plasma etching of a-Si:H

After lithographic patterning (described in the following section), a-Si:H films were etched in the PECVD reactor (Figure 2.2) using a pure hydrogen plasma. In this process, hydrogen gas is excited to create reactive H atoms (radicals) and/or ions, which sustain the plasma discharge;

$$e + H_2 \rightarrow e + 2H \tag{2.8}$$

$$e + H_2 \rightarrow 2e + 2H^+ \tag{2.9}$$

The etchant H atoms then react with species on the a-Si:H surface to yield the volatile etch product SiH_4, through the reaction;

$$4H(g) + Si \rightarrow SiH_4(g) \qquad (2.10)$$

This process is very similar to chemical-plasma etching techniques where F, Cl, or Br is used as etchant atoms to produce volatile etch products [55]. The etch mechanism is purely chemical in nature since the atoms (not ions), are directly responsible for the removal of material. In addition, since there is little directionality to the etchant atoms arriving at the surface, relatively isotropic etch processes are expected. The advantage here is the fact that the etch process is chemically selective. This is extremely important in that a-Si:H is used as a resist material in this study, and a means of selectively removing untreated portions is essential.

As in growth via PECVD, there are various interrelated factors that influence hydrogen plasma-etching of a-Si:H. Conditions must be established to create sufficient etchant H atoms, but also minimize dissociation of the volatile etch product, SiH_4. Dissociation of volatile silane molecules may result in film growth, so that etching and redeposition become competing processes. The etch rate is of particular concern for this work, and is dependent on rf power, H_2 flow rate, and substrate temperature. With other parameters held constant, the etch rate was found to peak at approximately 10 W rf power, and then decrease at higher rf powers (probably due to redeposition). While higher substrate heater temperatures will slightly increase the etch rate, a 50 °C limit was adopted to avoid possible thermal degradation of underlying films. High flow rates are desirable for etching (compared to deposition) and thus, a hydrogen flow rate of 300 sccm (and total pressure of 1 Torr) were

adopted for use throughout this study. While the complex interrelationship of all the etch parameters is not entirely understood, these conditions produced the best results by minimizing redeposition from reactions with volatile etch products [56]. Due to the shower-head gas delivery, the etch non-uniformity (estimated via profilometry), was generally less than 10%.

In-situ film thickness monitoring was especially crucial during the H_2 plasma etch procedure. HeNe laser interferometry was used to accomplish this task just as it was during deposition. In this case however, each fringe corresponds to approximately 100 nm of material removed, and the reflection profile recorded during a deposition can essentially be retraced to ensure complete film removal. A typical HeNe reflection profile for a 15 minute a-Si:H deposition followed by complete hydrogen etching is shown in Figure 2.4 below. The first set of fringes was recorded during deposition, while the second set was recorded during etching. For this particular run, a Si (100) substrate with a 100 nm thick thermal oxide (SiO_2) layer is used. Thus a double peak appears in each fringe, due to interference of reflections from the SiO_2/Si and a-Si:H/SiO_2 interface, in addition to the vacuum/a-Si:H interface. It is also evident (from the difference in fringe spacing) that the etch rate is significantly slower than the a-Si:H deposition rate, but increases slightly as the film is etched. Ex-situ thickness measurements have indicated typical deposition and etch rates of approximately 5 Å/s and 1 Å/s, respectively. In principle, complete film removal could be ensured by etching until the profile flattens, as in Figure 2.4. It must be noted however, that the thickness information comes from a very limited

portion of the surface. Therefore, a slight over-etch was typically used in experiments where complete film removal was desired.

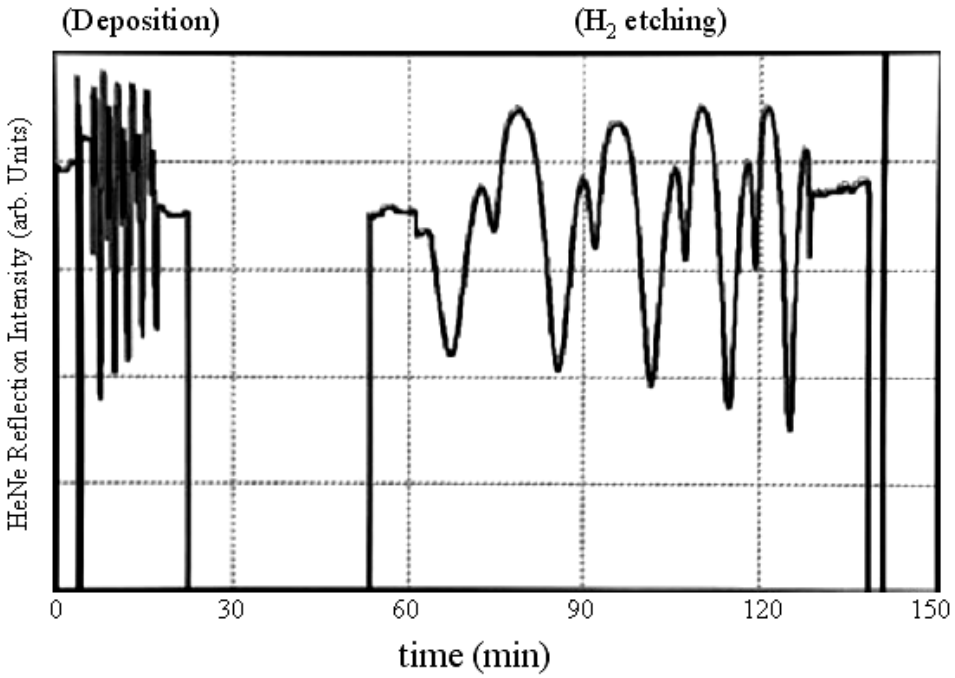

Figure 2.4: Reflection profile from HeNe laser for 15 min a-Si:H deposition followed by hydrogen plasma etching for 88 minutes. Complete etching of the a-Si:H layer is indicated by a flattening of the profile after the deposition profile has been retraced. The small peaks present in each fringe occur due to a thin oxide layer on the Si substrate.

2.3 Excimer laser lithography

A Krypton-Fluoride laser (KrF) was used in this study to modify selected regions of the a-Si:H surfaces, thereby creating a pattern for subsequent H_2 plasma development. Excimer laser sources such as KrF have been used by the microelectronics industry, primarily due to the demand for smaller and smaller device feature sizes. Due to the 248 nm wavelength of KrF sources, usable linewidths (feature sizes) as small as 0.3 μm have been reported [57]. In this work however,

linewidths in this size range are not necessary. The projection optics set-up in our system (described below) allows a minimum linewidth (resolution) of 5 μm. The KrF laser was chosen for this work mostly to achieve a wide range of output energies and to study the resulting modification of a-Si:H surfaces.

A schematic diagram of the projection optics system used for lithography is shown in Figure 2.5. Starting from the laser, a mirror (coated for high reflection at 248 and 632.8 nm) directs the beam into the center of the line of optics. The beam then passes through a 10 cm focal length diverging lens followed by a 20 cm focal length converging lens. This combination expands the raw excimer beam into a roughly 2.5 x 2.5 cm square beam. Next the beam passes through the mask, which is mounted on a tilt stage for fine tilt adjustment and translation. A turning mirror then directs the beam upward through a relay lens with 2x reduction for final focusing. A quartz vacuum viewport with dual side antireflection coating is the last component in the optics system, before the beam reaches the sample. Optics alignment and sample positioning (for lithography) are carried out by using a HeNe laser mounted behind the rear mirror of the laser cavity.

Due to the absorption characteristics in the deep UV regime, the lenses are made entirely of fused silica [58] to reduce attenuation of the beam. In addition, the mask itself is either chrome or aluminum on quartz. Nevertheless, significant attenuation of the laser power occurs, and careful measurement of the actual energies reaching the sample was necessary for this study. A laser power meter was placed at the sample exposure position in the load-lock chamber to carry out energy density measurements. The laser (Lumonics PM844 KrF) was set up to give 10 pulses per

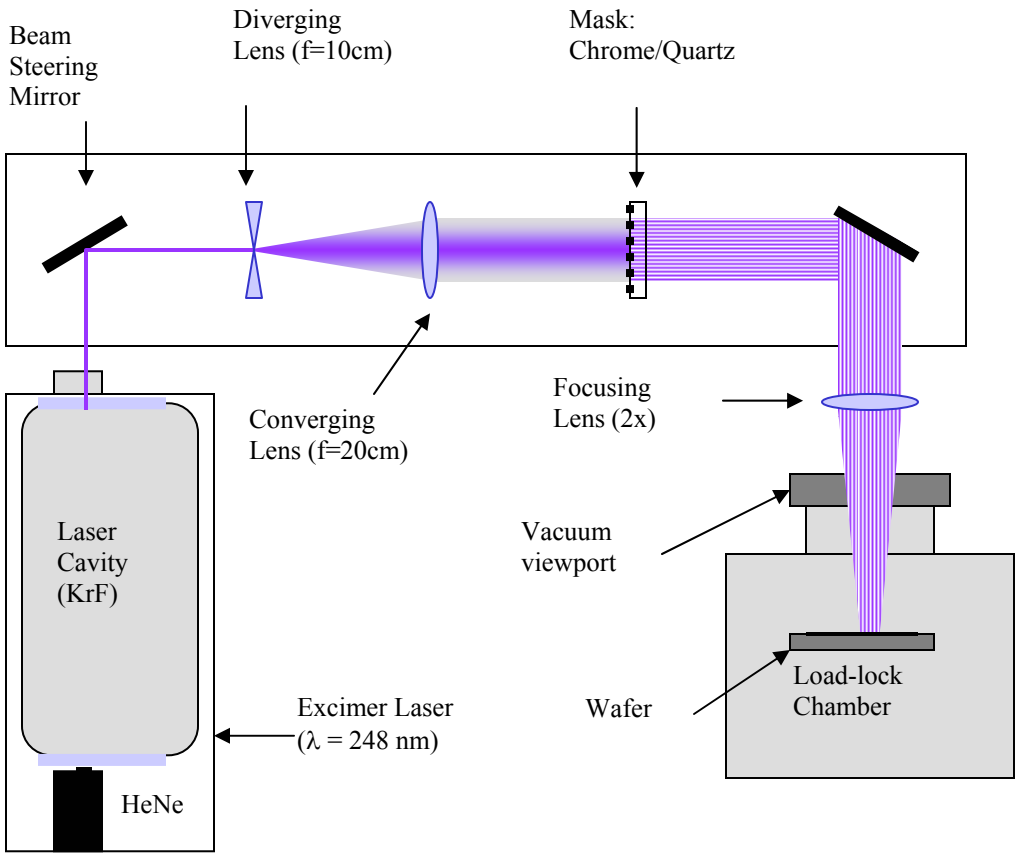

Figure 2.5: Simplified schematic diagram of projection optics system used to carry out laser-lithography on a-Si:H surfaces.

second, while the power meter (An/2 Ophir) was set for a 1 second averaging period. The average power was recorded as a function of input laser voltage over the usable range of the laser (23-40 kV). In addition, UV burn paper was placed at the exposure position to obtain a direct measurement of the exposed area (A). Thus the actual energy density at the exposure position E_{ex}, could be calculated by

$$E_{ex} = \frac{P}{RA} \tag{2.11}$$

where P is the average power, and R is the repetition rate, (10 s^{-1}).

This energy density is plotted vs. input laser voltage in Figure 2.6 below. Since the unattenuated energy output of the laser (E_0) is known, the percentage of energy actually reaching the sample δ, could be calculated via AE_{ex}/E_0. Figure 2.6 also shows a plot of the energy density E_δ, calculated using

$$E_\delta = \frac{\delta_{av} E_0}{A} \qquad (2.12)$$

where δ_{av} is an average δ obtained using data from the entire range of output laser energies. Since the two curves match very closely, E_δ was used throughout this study as it gave a reasonably accurate and simple method for estimating the laser energy densities reaching the sample.

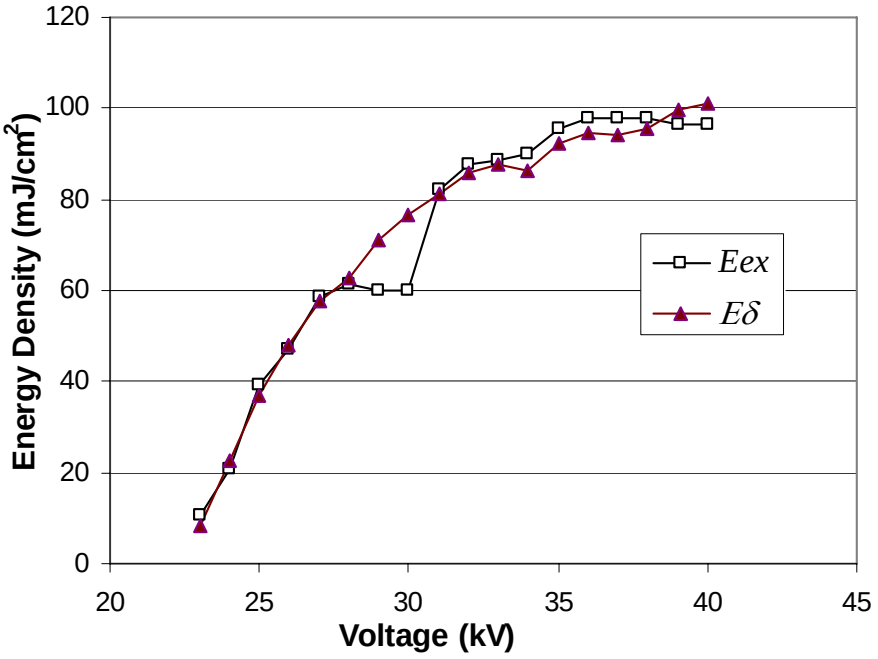

Figure 2.6: Measured laser energy density E_{ex}, reaching the sample at the exposure position as a function of input laser voltage. E_δ was calculated based on the measured average percentage of the Excimer output energy reaching the sample.

2.4 Electron Cyclotron Resonance Plasma etching

After a planar a-Si:H film was transformed into a mask by irradiation and development, the mask pattern was transferred into the underlying film layer by Electron Cyclotron Resonance (ECR) plasma etching. ECR reactors allow "remote processing" in that the substrate lies outside the plasma generation zone. The advantage is that the probability of etch products interacting with the plasma is greatly reduced [59]. In turn, this reduces the possibility of redeposition. In addition, independent control of various plasma parameters is obtained so that high ion densities and high anisotropic etch processes may be achieved even at low pressures.

In ECR processing, microwave radiation is used to excite the plasma, which is confined due to the presence of a static magnetic field. The magnetic field B produces a Lorenz force causing the plasma electrons to move in circular orbits with a characteristic cyclotron frequency $\omega_c = eB/m_e$, where e is the electronic charge and m_e is the electron mass. When the microwave driving frequency ω_m is equal to the frequency of the plasma electrons ω_c, a resonance condition occurs. This resonance results in a relatively high degree of dissociation and ionization at pressures as low as 10^{-5} Torr. By applying a dc bias to the wafer, the energy of incident ions, and thus the degree of etch anisotropy, can be controlled [60].

Figure 2.7 shows a schematic diagram of the Model 375 PlasmaQuest ECR reactor used for mesa etching. An ASTeX 2.45 GHz source supplied microwave power through a quartz window. The upper electromagnet produces an 873 gauss field to create the resonance condition ($\omega_c = \omega_m$), while the lower magnets are used to confine and control the ion trajectories. A DC self-bias potential was established at

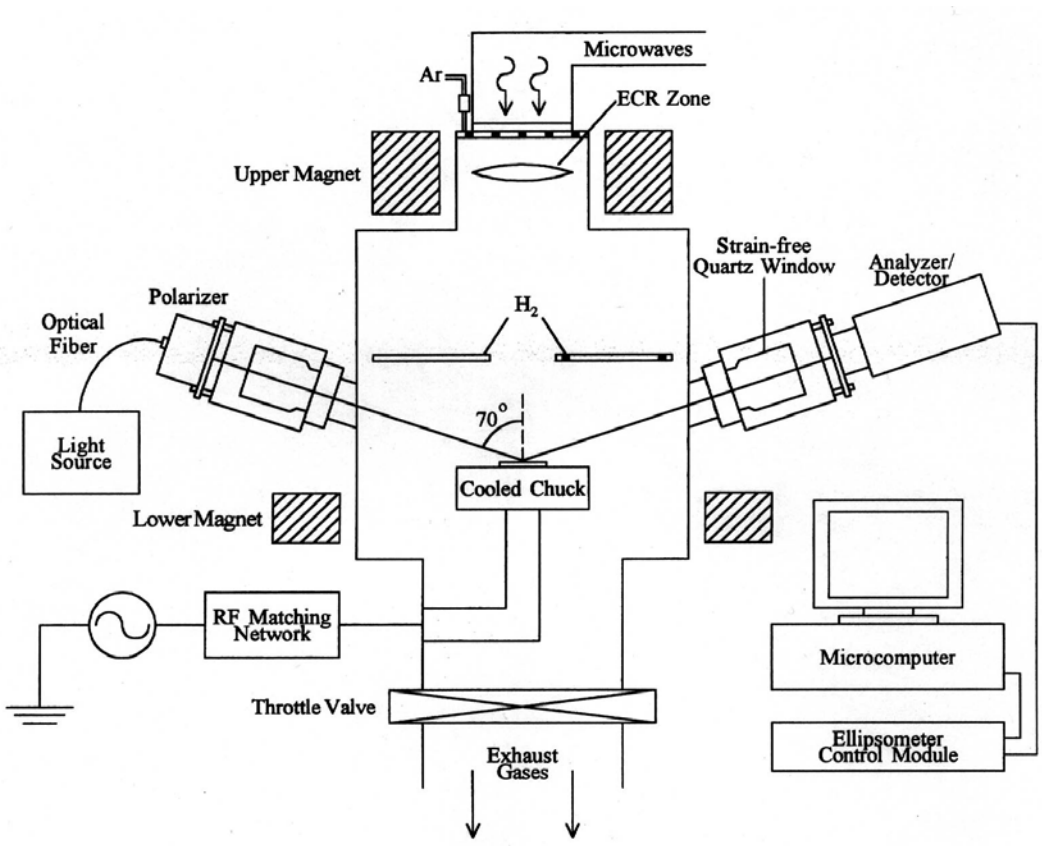

Figure 2.7: Schematic diagram of the ECR reactor used for mesa etching after carrying out the a-Si:H deposition, exposure, and development procedures [26].

the substrate using a capacitively coupled 40.68 MHz (rf) generator. This self-bias potential is caused by the formation of a thin plasma "sheath" near the substrate, which is due to the same reasons discussed in section 2.2. The ECR is also equipped with a spectroscopic ellipsometer for in-situ film characterization.

ECR plasma parameters and etch chemistries at the Night Vision Laboratory have been optimized specifically for etching CdTe and HgCdTe films. A 4:1 argon to hydrogen ratio (80 sccm Ar and 20 sccm H_2) is typically used, giving an overall

chamber pressure of 2 mTorr. Argon gas is injected above the ECR (plasma) zone, to generate Ar ions. The Ar ions are then used to dissociate H_2 gas (injected downstream) to create etchant H atoms, which are thought to react primarily with Te to form TeH_2. This configuration minimizes the formation of H ions, which would require the energies provided only in the plasma zone [61]. Other ECR process parameters for CdTe/HgCdTe etching include an input microwave power of 300 W, and an rf power (to the substrate) of 120 W [62].

2.5 Vacuum photolithography system and procedure

As stated in chapter 1, the ultimate goal of the Night Vision Laboratory microfactory concept is to demonstrate an all-vacuum processing line for producing MCT-based focal plane arrays. The work described in this dissertation focuses on the development of a vacuum-lithography process, which is a crucial step for realization of this goal. Thus, the processes described above, include only those essential for carrying out the in-situ lithography procedure.

Figure 2.8 illustrates the experimental vacuum-lithography procedure, with essential process steps numbered in order (refer also to Figure 1.2). The schematic diagram assumes that MBE growth of HgCdTe and/or CdTe has already been performed. Step 1 is carried out in the PECVD chamber where growth of an a-Si:H resist layer takes place. A robotic arm transfers the wafer to the exposure position in the load-lock chamber where patterning is carried out via excimer laser exposure (step 2). In step 3, the wafer is transferred back to the PECVD for full pattern development via hydrogen plasma etching. Finally, for step 4, the wafer is

transferred through the microfactory processing line via conveyer belt to the ECR reactor for simultaneous mesa etching (pattern transfer) and resist stripping.

Under the right conditions the ECR reactor might very well be used to perform step 3, in which case a more anisotropic pattern development process could be achieved. However, the existing procedure (where step 3 is performed in the PECVD reactor) satisfies our current project requirements. ECR development etching may be employed in future projects that require smaller linewidths, deeper trenches, and thus more anisotropic etch processing.

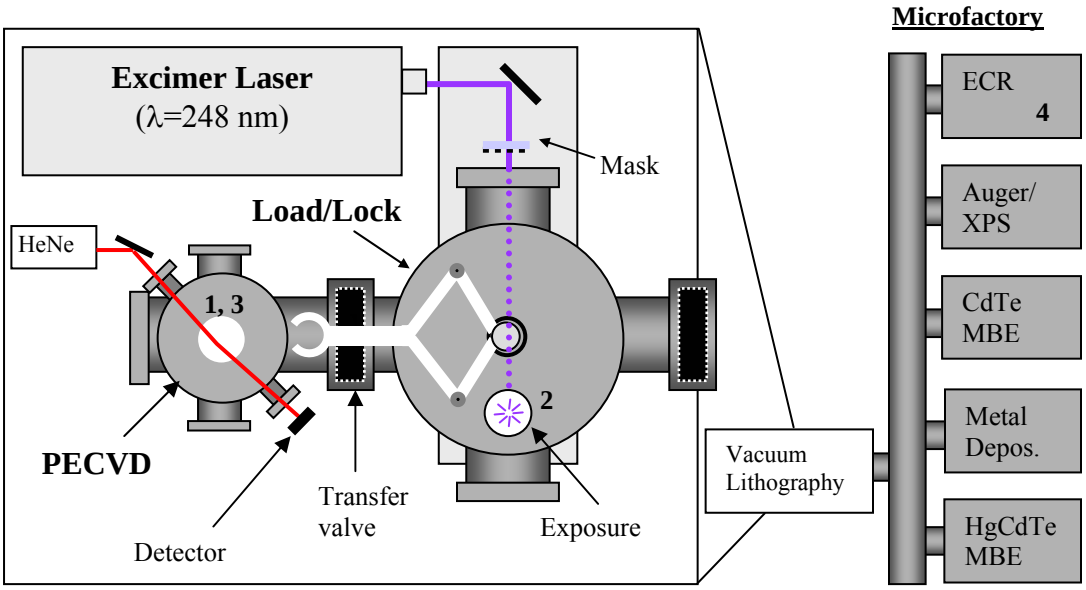

Figure 2.8: Experimental Vacuum-lithography System and NVESD Microfactory. Process steps for vacuum-lithography procedure are indicated in numbered order. [62]

2.6 Characterization tools

2.6.1 Surface Profilometry

Of the various ex-situ characterization methods employed throughout this study, surface profilometry was the simplest and most frequently used for measuring film thickness, etch depth, and surface roughness. A stylus is scanned across a film surface with topographical features, and its vertical movement is electromagnetically sensed as a function of position. The stylus is typically made of diamond and the radius at the tip can be as small as 0.2 μm. The available range of stylus force (0.1 to 50 mg), allows step height measurements between 5 nm and 800 μm. Due to factors such as surface roughness, possible stylus penetration, or equipment vibration, a minimum 1% error of the measured step height can be expected, (as observed in between successive scans) [63].

Profilometry scans were carried out using either a Sloan Dektak 3030, or Veeko Dektac 8. Both instruments were mounted on vibration-isolated tables and produced identical scans when operated at 5 mg stylus force. In addition, both instruments included data analysis functions for calculating average heights and rms roughness from a specified measurement range. In certain cases, optical micrographs are presented along with profilometer data, to show the region over which a particular scan was taken.

2.6.2 Transmission Electron Microscopy

2.6.2.1 Basic Modes of Operation

Transmission electron microscopy (TEM) was primarily used in this work to carry out structural characterization of processed a-Si:H resists. Microstructural information from TEM was obtained through two basic modes of operation, which are shown schematically in ray diagrams (see Figure 2.9). It should be noted first that the term "lens" used here actually refers to electromagnetic coils used to guide an electron beam. The focusing power in these electromagnetic lenses is altered by changing the current through the coils so that this system essentially mimics that of light passing through a series of convex optical lenses. Electrons are thermionically emitted from a cathode filament through a condenser lens system and onto an electron transparent specimen. Various scattering mechanisms occur as the beam passes through the specimen so that in addition to a primary (unscattered) transmitted beam, several diffracted beams emerge. An objective lens positioned at the exit surface of the sample focuses the beam to create a diffraction pattern (DP) on its back focal plane, after which the beam recombines to form an intermediate image just before the selected area aperture. Subsequent magnifying and projector lenses combine to form a final magnified image on a fluorescent viewing screen. The strength of the current through the intermediate lens determines whether the diffracted spots (i.e. diffraction mode) or a magnified image (i.e., imaging mode) is viewed on the screen [64,65,66].

The two basic modes, diffraction (Figure 2.9a), and imaging (Figure 2.9b), combine to provide a powerful technique for microstructural characterization of materials. In diffraction mode, the crystal structure of the material is revealed

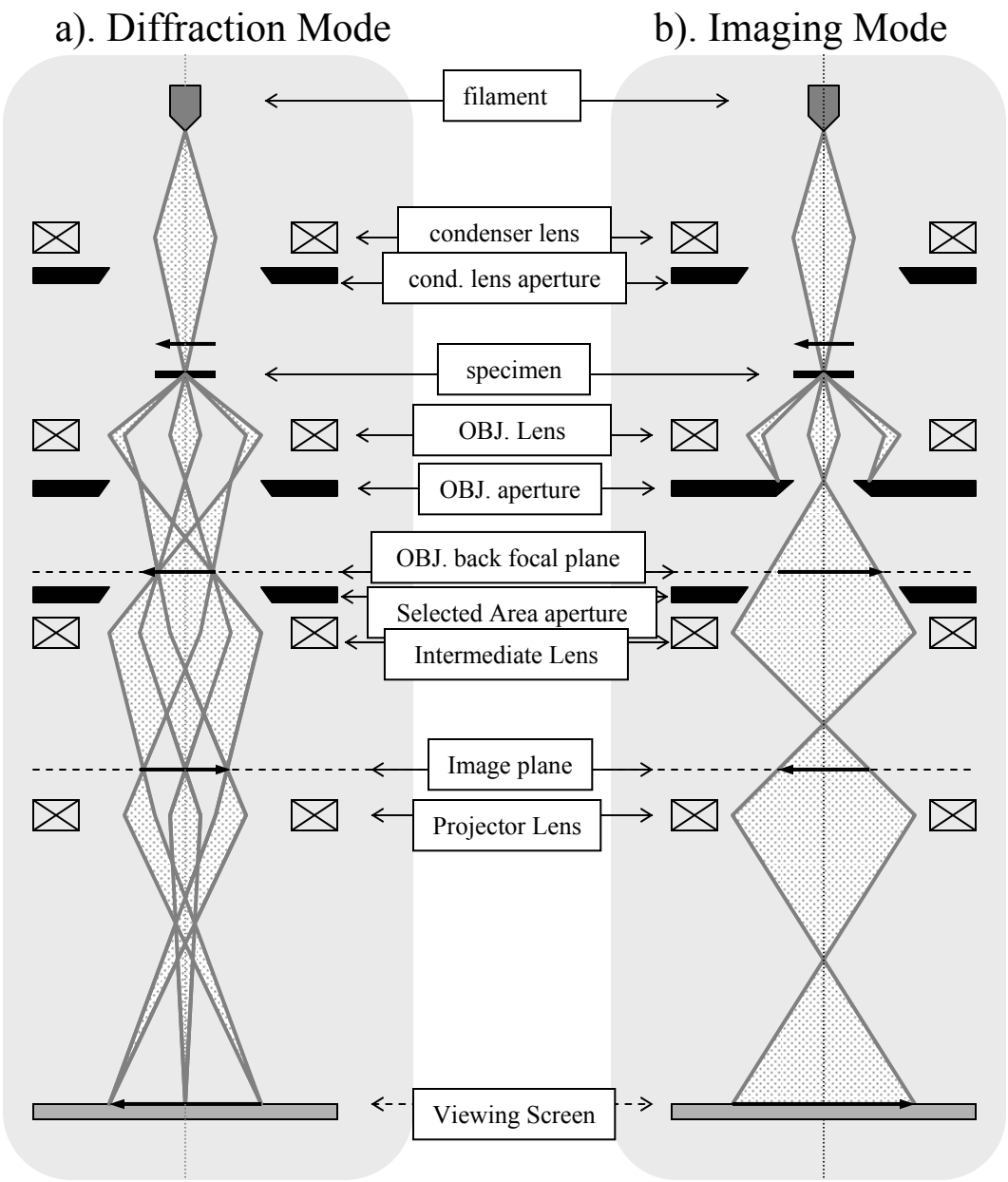

Figure 2.9: Ray diagrams showing two basic operating modes in TEM. In diffraction mode (a), imaging the back focal plane of the objective lens projects an amplitude contrast image (diffraction pattern) of the specimen onto the fluorescent viewing screen. In imaging mode (b), the current in the intermediate lens is altered so that an image (having both amplitude and phase contrast) is projected onto the screen [89].

through the position of the various spots ($\boldsymbol{g}$ = *hkl*) about the transmitted beam ($\boldsymbol{g}$ = 000) in the DP (where *hkl* are miller indices). While only amplitude contrast contributes to DPs, both amplitude and phase contrast contribute to an image. There are thus various methods in TEM to obtain several kinds of images such as bright field, dark field, and phase contrast (lattice imaging). In this dissertation however, only bright field imaging and phase contrast imaging were carried out extensively.

To form a bright field (BF) image, a specimen is first tilted (in diffraction mode) to find the desired zone axis diffraction pattern (i.e., so that the transmitted beam is perpendicular to a particular lattice plane). In thin film applications, this is typically done using an electron transparent region of the single crystal substrate. The objective lens aperture is then positioned so that all diffracted beams are blocked, and only the transmitted beam reaches the viewing screen. The resulting image produced (after switching back to imaging mode) is one of maximum "diffraction contrast" and is termed a BF image [67]. Note that a BF image is implied in Figure 2.9b, where only the transmitted beam passes through the objective lens (OBJ) aperture.

The ability to obtain structural information at sufficient magnifications made TEM a crucial characterization tool for this study. The high magnification is the result of a small effective wavelength λ, according to the de Broglie relationship (taking into account relativistic effects),

$$\lambda = \frac{h}{\sqrt{2m_0 eV\left(1+\frac{eV}{2m_0 c^2}\right)}} \tag{2.13}$$

where h is Planck's constant, m_0 is the electron rest mass and V is the acceleration voltage. For phase contrast or “high resolution” imaging of crystalline films, the OBJ

aperture is placed so that only the transmitted beam and a few diffracted beams are utilized. In this way, both the amplitude and phase of the diffracted beams contribute to the image and the resulting contrast is a reflection of the periodicity of the crystal lattice structure.

A microscope of sufficient magnification must be used in order to obtain phase-contrast images. A JEOL 4000FX transmission electron microscope operated at 300 KV was used in this study. This gives an effective electron wavelength (λ), of 0.00197 nm and a spatial resolution of 0.2 nm under optimum conditions.

2.6.2.2 Sample Preparation

Preparation of cross-sectional samples for TEM characterization (Figure 2.10) required significant attention and careful adherence to a meticulous procedure. Samples were first diamond scribed, cut, glued, and clamped with film sides face to face, keeping note of the known macroscopic orientation of the substrate. The glue used here was an epoxy (M-bond 610), which was hot-plate cured at 100 - 200 °C for approximately 1-3 hours depending on the specimen material. The sandwiched structure was then wax-mounted on the L-bracket of a tripod polisher (Southbay Technologies Inc.) for polishing one side using diamond lapping sheets with successively smaller grinding particle sizes (30-1 μm). The sample was then removed from the L-bracket and remounted to polish the second (opposite) side. While polishing the second side, the thickness was monitored using a novel technique developed by H. Li et al [68]. After reaching a thickness between 15 and 20 μm, the sample was mounted on to a Cu Grid and carefully removed from the L Bracket. A Baltech Res 100 etching system with dual ion guns was then used to mill out a small

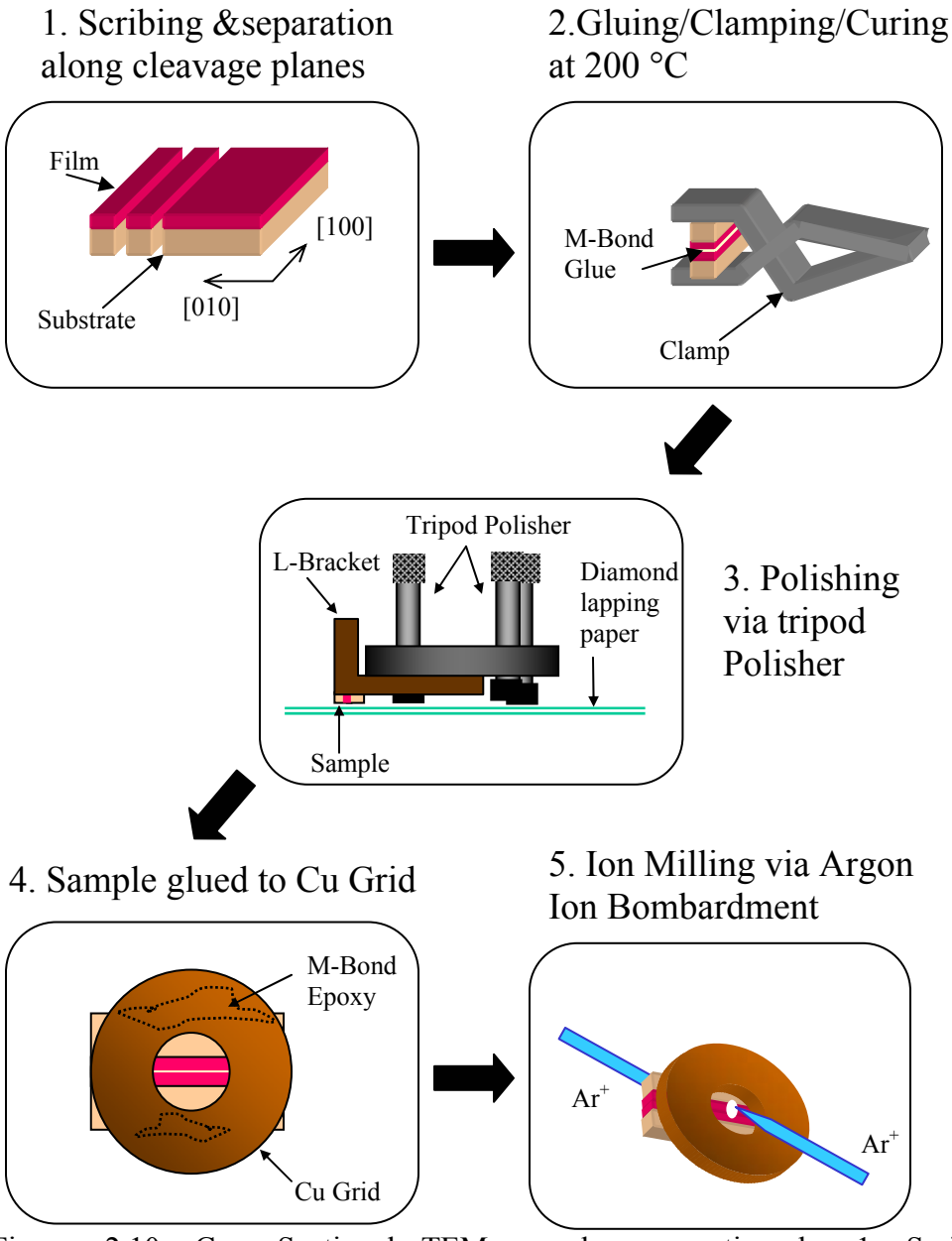

Figure 2.10: Cross-Sectional TEM sample preparation by 1; Scribing and separation, 2; clamping and curing at 200 ºC, 3; Polishing to < 20 µm with diamond lapping sheets, 4; Mounting on Cu Grid, and 5; Ion milling until perforation. Electron transparent regions are created in regions surrounding hole [69].

hole using argon ions incident at a 12 degree angle. The argon ion beam was produced using an acceleration voltage of 4 KV and 2 mA current, which lead to a typical milling duration of 1.5 hrs. It should be noted that the voltage and current used, as well as the required milling duration, varies with the specimen material. After this procedure, essentially four areas surrounding the hole have a strong likelyhood of being electron transparent (thickness < 100 nm) to allow for meaningful TEM study.

2.6.3 Scanning Electron Microscopy

Scanning electron microscopy was used to image mesa profiles particularly after ECR etching for selected times. A typical SEM uses thermionically emitted electrons, which are focused by two successive condenser lenses into a fine spot size of approximately 1-10 nm. As illustrated in Figure 2.11 [70], several different electronic excitations occur as a result of the incident electron beam, which is commonly in the ~30 KeV energy range. The various electron and photonic signals emitted from the tear-shaped interaction volume, are detected and/or imaged, and form the basis of several SEM techniques.

The most common imaging technique uses secondary electrons which are generated in the atomic lattice due to excitation by the primary beam. The low energies (below 50 eV [71]) associated with secondary electrons, means they originate from subsurface depths of less than a few angstroms. In addition, electron emission from sloped surfaces is greater than from horizontal surfaces (see Figure 2.11c), so that edges tend to appear brighter than flat regions. For these reasons,

secondary electron imaging is ideal for studying surface topography. SEM analysis was carried out on a CamScan Maxim 2040SL operated at 20-34 KeV with a spatial resolution of 4 nm.

2.6.3.1 Energy Dispersive X-ray Spectroscopy

The SEM described above was also equipped with an energy dispersive x-ray (EDX) spectroscopy system, which was useful for simultaneously determining chemical species in selected regions of the etch profile. In EDX, the incident electron beam excites an atom, ejecting (for example) a K shell electron and creating a vacancy.

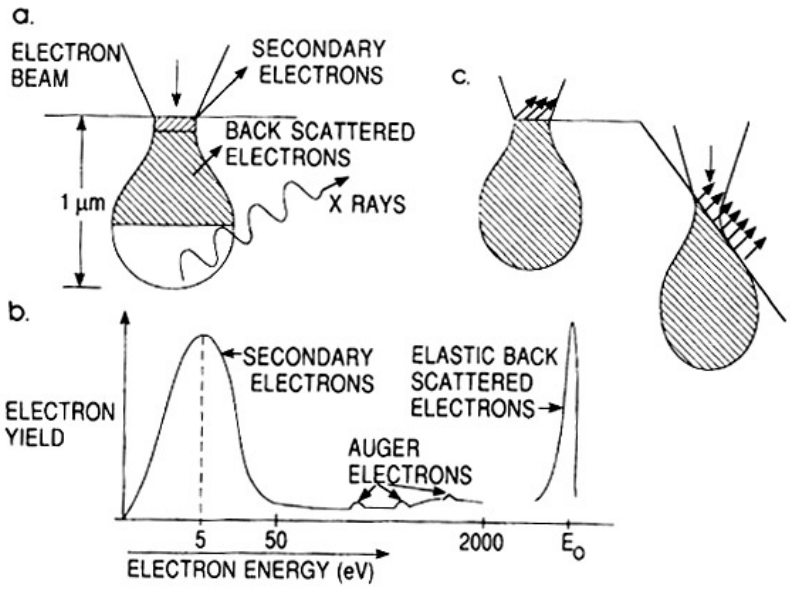

Figure 2.11: (a) Electron and photon signals emanating from tear-shaped interaction volume during electron-beam impingement on specimen surface. (b) Energy spectrum of electrons emitted from specimen surface. (c) Effect of surface topography on electron emission. Reprinted from M.C. Ohring, Materials Science of thin films [70].

This vacancy is filled by an outer shell electron, and an x-ray photon is emitted in the process. For example, an electron transition between the L and K shell, produces a Kα x-ray. The energy of the emitted x-ray photon depends on the specific electron transition that occurs, and is thus characteristic of the atom involved. It should be noted that EDX has an effective probe depth of ~1 μm, and may be limited to detection of elements with Z > 11 due to the use of a Beryllium window at the detector [72].

EDX analysis was used in this work to determine the chemical species present in films at selected ECR etch times, and was particularly useful for obtaining compositional profiles of cross-sectional samples. An EDAX DX-prime60 was used to obtain energy dispersive x-ray spectra.

2.6.4 Auger Electron Spectroscopy

For near surface chemical analysis of mesa-etched films, auger electron spectroscopy (AES), was performed. AES is similar to EDX in that electrons are initially used to excite the sample surface, and resulting electron transitions yields information unique to a particular atom. In AES however, a more complex transition takes place, where excess energy is not expended by creating a photon, but by ejecting an electron from the atom. The ejected or (Auger) electrons are counted by a hemispherical analyzer, which is configured so that only electrons in a selected energy range ΔE are detected. By sweeping a bias potential applied to the coaxial hemispheres, the entire electron spectrum can be measured. The actual Auger spectrum is obtained by electronic differentiation of the total electron yield to

enhance the magnitude of the Auger peaks. This is a true surface analytical technique in that typical systems use a finely focused ~2 KeV electron beam, and less than 15 Å of the surface is usually examined [73]. AES analysis was carried out on a Phi 5802 Scanning Auger system.

2.6.5 Fourier Transform Infrared Spectroscopy

Infrared spectroscopy is an invaluable tool for analyzing the molecular vibrational modes in certain materials. For a-Si:H thin films, IR absorption studies have produced a wealth of knowledge regarding Si-H bonding characteristics [74,75]. IR spectroscopy makes use of the fact that different inter-atomic bonds will vibrate in resonance with, and thereby absorb, IR light at a particular frequency. Other frequencies are simply transmitted through the material. Thus, the dependence of the transmitted intensity as a function of frequency can be obtained. A conventional "dispersion" IR spectrometer achieves this using a grating. The grating disperses IR light transmitted through the sample and a narrow frequency band is sent to a detector. Alternatively, a Fourier transform infrared (FTIR) spectrometer uses interferometry to capture the IR signal as a function of the path difference. The collected data is then Fourier transformed to convert the IR signal to frequency space. The main benefit of FTIR is the ability to automatically measure the transmitted IR signal for a wide range of frequencies, rather than for a narrow frequency band at a time. Other advantages include higher signal to noise ratios and better accuracy over a wide frequency range [76]. In this thesis, IR spectra is reported as absorbance rather than transmittance, to maintain consistency with the literature. The absorbance is defined by

$$A = \log\left(\frac{1}{T}\right) \tag{2.14}$$

where T is the % transmittance. Analyses of a-Si:H films were performed on a Nicolet 8700 series FTIR spectrometer.

2.6.6 Double Crystal Rocking Curve X-ray Diffraction

X-ray diffraction techniques can provide very accurate information about the average crystal quality in an epitaxial thin film. In a standard θ-2θ single crystal diffractometer, the x-ray beam is directed at the sample and scanned through a range of angles. Diffracted x-rays that satisfy the Bragg condition ($n\lambda=2d_{hkl}\mathrm{Sin}\theta$) are collected by the detector and show strong diffracted intensities (peaks). The position and width of a particular peak are direct measurements of lattice spacing, and crystallinity, respectively. However the measurement precision is typically limited by spectral dispersion, which leads to unwanted peak broadening. The double crystal x-ray diffractometer reduces peak broadening by using two parallel crystals which are made to satisfy the Bragg condition. During a scan, the sample can be rocked through a very small angular range to produce a "rocking curve" x-ray scan. This diffraction technique has been extensively used to examine (with arc second resolution), the crystalline quality in thin epitaxial films [77]. Double Crystal Rocking Curve (DCRC) measurements were obtained in this thesis to examine the effects of a-Si:H lithography processing on HgCdTe films.

Chapter 3

Characterization of PECVD a-Si:H resists deposited via argon-diluted SiH_4

3.1 Introduction

Several authors have reported the use of plasma reactors for deposition of photosensitive organosilicon polymers [32,33,34]. Others have recognized the potential uses of hydrogen-passivated silicon films as resist layers for dry lithography [29,30,78]. In contrast to wet-chemical techniques, resist deposition, UV exposure, pattern development and pattern transfer can all be carried out within a vacuum environment. This could enable a complete high vacuum semiconductor processing line where wafer surface contamination is minimized and cycle times are greatly reduced [35]. The use of an amorphous hydrogenated silicon (a-Si:H) resist to pattern HgCdTe epilayers for use in infrared detectors has been reported [27]. Among the existing dry lithography techniques, this may be the most mature technology for integration into an existing all-dry processing line.

During the proof of concept study described in chapter 1, amorphous hydrogenated Si resists were deposited using a pure silane (SiH_4) precursor. Following deposition, the excimer laser exposure procedure was carried out within an oxygen-containing environment to promote oxidation of irradiated regions of the surface. During the subsequent hydrogen plasma development step, an etch

selectivity of approximately 500:1 was achieved between un-irradiated and irradiated regions of the a-Si:H.

A significant drawback to the use of pure SiH_4 during plasma deposition of a-Si:H films is the creation of SiH_x dust. These macroscopic dust particles form due to rapid gas-phase reactions occurring within the plasma. This poses a potential problem for the NVESD microfactory, due to the possibility of contamination in other process chambers. Argon dilution is expected to reduce SiH_x dust formation by decreasing the SiH_4 concentration and thus the amount of gas phase reactions taking place within the plasma [79]. Consequently, Ar dilution would lead to a more environmentally benign process and would reduce the possibility of cross-contamination in adjacent processing chambers. In this chapter the effects of argon-dilution (during deposition) on the a-Si:H films, and in turn, on the existing dry-lithography process, is investigated. Profilometry is used to examine the effects of different exposure ambients on pattern development while TEM is used to characterize the irradiated surfaces. Finally, the effects of argon-dilution on a-Si:H film properties are directly investigated using FTIR, in efforts to confirm assertions made in this chapter.

3.2 Experimental Procedure

The work presented in this chapter focuses on the lithography processes that take place prior to mesa etching (pattern transfer to underlying films). Procedures used for this particular study (i.e.; resist deposition, excimer laser

irradiation, and H_2 development-etching) are summarized below. A more detailed description of these process steps was provided in chapter 2.

For resist deposition, a-Si:H layers with thicknesses ranging from 300 to 600 nm were grown via PECVD at 3 W rf power and at a substrate temperature of 50 °C. Pure Ar was first introduced into the chamber via needle valve to give a pressure of 50 mTorr. Another gas source containing 10% SiH_4 in Ar was then introduced via mass flow controller at 100 sccm. With both gasses flowing and the throttle valve open, a total chamber pressure of ~145 mTorr was obtained. Therefore the percentage silane gas used was only 6.5%. The throttle valve was then adjusted to maintain an overall pressure of 500 mTorr so that the actual silane partial pressure was probably less than ~33 mTorr. These parameters were used for deposition as they were found to minimize SiH_x dust formation, while reasonable deposition rates (5 Å/s) could be achieved.

Excimer laser irradiation was carried out using projection optics with approximately 2x reduction to image a mask pattern on the sample. Laser fluences with energy densities (per pulse) up to 100 mJ/cm^2 were used to determine threshold doses for full pattern development. Three exposure ambients were investigated in this study, including O_2/Ar mixtures at 1 Torr, air at atmosphere and vacuum at 10^{-8} Torr. The O_2/Ar ambient was established by simply leaking the gasses into the Load-Lock chamber (via the PECVD) and then stopping the flow at 1 Torr to establish a static mixture. The partial pressure of O_2 in this mixture did not exceed 100 mTorr (10%).

Several samples in this study were subjected to hydrogen plasma-development, which took place in the PECVD chamber. While development-etch durations may vary, other plasma parameters were fixed at 10W rf power, 300 sccm H_2, and an overall pressure of 1 Torr.

Characterization of the samples was carried out using techniques described in chapter 2. Profilometry was performed on a Veeko Dektac 8 using 5 mg stylus force. Cross-sectional TEM samples were prepared as mentioned in section 2.6.2.2, and analysis was carried out on a JEOL 4000-FX operated at 300 KV. Finally, Infrared absorption studies were performed using a Nicolet 8700 FTIR spectrometer.

3.3 Effect of exposure ambient on pattern development

During the proof of concept carried out by Hollingsworth et al [27], a detailed study was done to determine the UV dose requirements for pattern generation in different ambients. The a-Si:H resists were deposited from a pure silane source. In this experiment a threshold was defined as the minimum energy density per pulse, required to allow full development of a 500 nm thick a-Si:H layer after hydrogen plasma etching. It should be noted here, that full development means complete removal of unirradiated a-Si:H, with no observable etching of irradiated regions. Figure 3.1 shows the threshold energy (per pulse) vs. number of pulses for exposures that were carried out in 5% O_2/Ar at 1 Torr and in air at atmosphere. It was shown that the threshold energy per pulse decreased with number of pulses. Note however that the total dosage (pulse energy * number of pulses) increases with increasing number of pulses. For example, the total dosage at 1 pulse (for 5% O_2/Ar

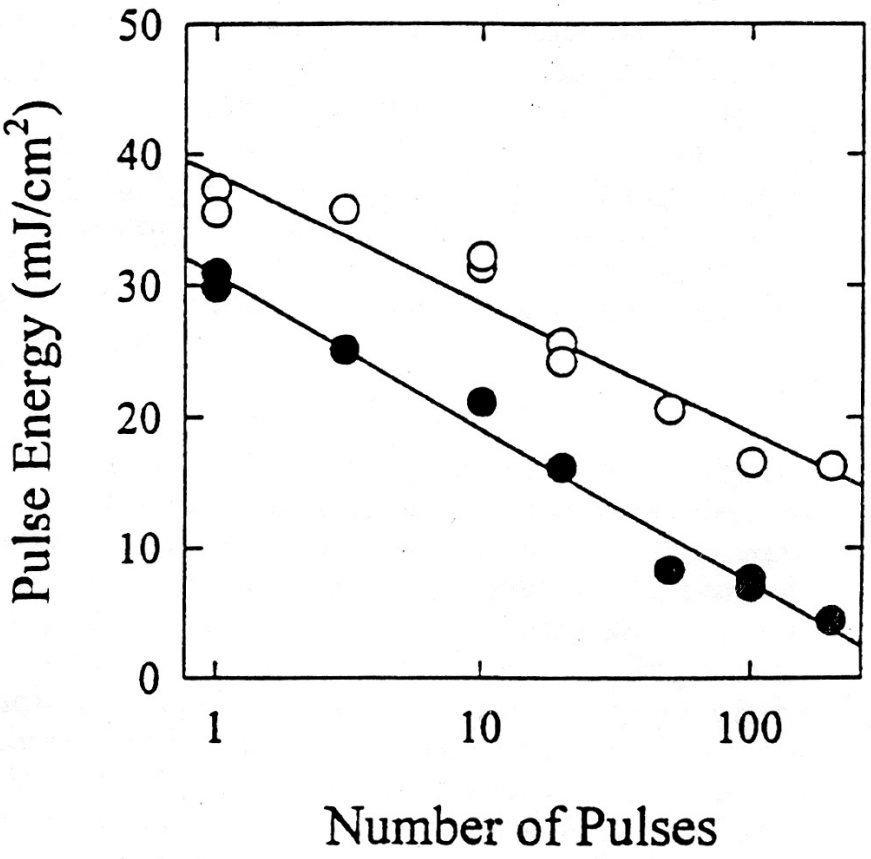

Figure 3.1: Threshold energy per pulse for generation of 500 nm thick resist patterns. In this case the a-Si:H resists were deposited via undiluted silane. The Solid circles are for irradiation in air at atmosphere (760 Torr) and open circles are for irradiation in 5% O_2/Ar at 1 Torr (reprinted from Hollingsworth et al [27]).

at 1 Torr) was ~35 mJ/cm^2, but at 100 pulses, the total dosage was ~1700 mJ/cm^2 (100*17). Evidently, a single pulse alters the a-Si:H surface such that subsequent pulses at the same energy density, desorb less and less hydrogen. Significant H desorption in the exposed surface is required to promote the formation of a sufficient oxide mask for development of the resist. Thus, a simple linear relationship between the total dosage required for resist development and the number of pulses is not observed. The data also shows that threshold pulse energies were lower for exposures

in air, than in 5% O_2/Ar at 1 Torr. This may be explained by noting that additional O_2 is available in air (compared to the 1 Torr ambient), so that oxidation in exposed regions occurs more readily. The general trend here is consistent with that expected from a pattern generation mechanism based on UV enhanced oxidation [30,35].

A comparative experiment was carried out for the a-Si:H films used in our study. In this case, 500 nm thick a-Si:H films were grown using a 10% SiH_4 in Ar precursor and then irradiated using (approximately) the same energy densities and corresponding number of pulses from the data reported in Figure 3.1. Thus, pattern thicknesses of ~500 nm following complete hydrogen plasma removal of unirradiated regions would indicate full development. The goal here was to determine whether the threshold doses obtained previously, would allow full development of the films grown in our study. The results are presented in Figure 3.2 and show pattern thickness vs. pulse energy density for irradiation in 5% O_2/Ar at 1 Torr (a), and in air at atmospheric pressure (b). The number of pulses fired at a particular energy density is also indicated. The data shows that none of the threshold doses from Figure 3.1, were sufficient for full pattern development of the a-Si:H films in this study. For both exposure ambients (in Figure 3.2), a pulse energy density of approximately 60 mJ/cm^2 was required for full hydrogen plasma development of the films.

Figure 3.3 shows a typical surface profile of a partially developed pattern in a film previously irradiated at approximately 50 mJ/cm^2 in O_2/Ar at 1 Torr. The film was H_2 development-etched for 30 min, so that approximately 200 nm should be removed from unexposed regions. A scan across a 100 μm mesa array, reveals well defined ~350 nm steps. This thickness is significantly greater than was expected,

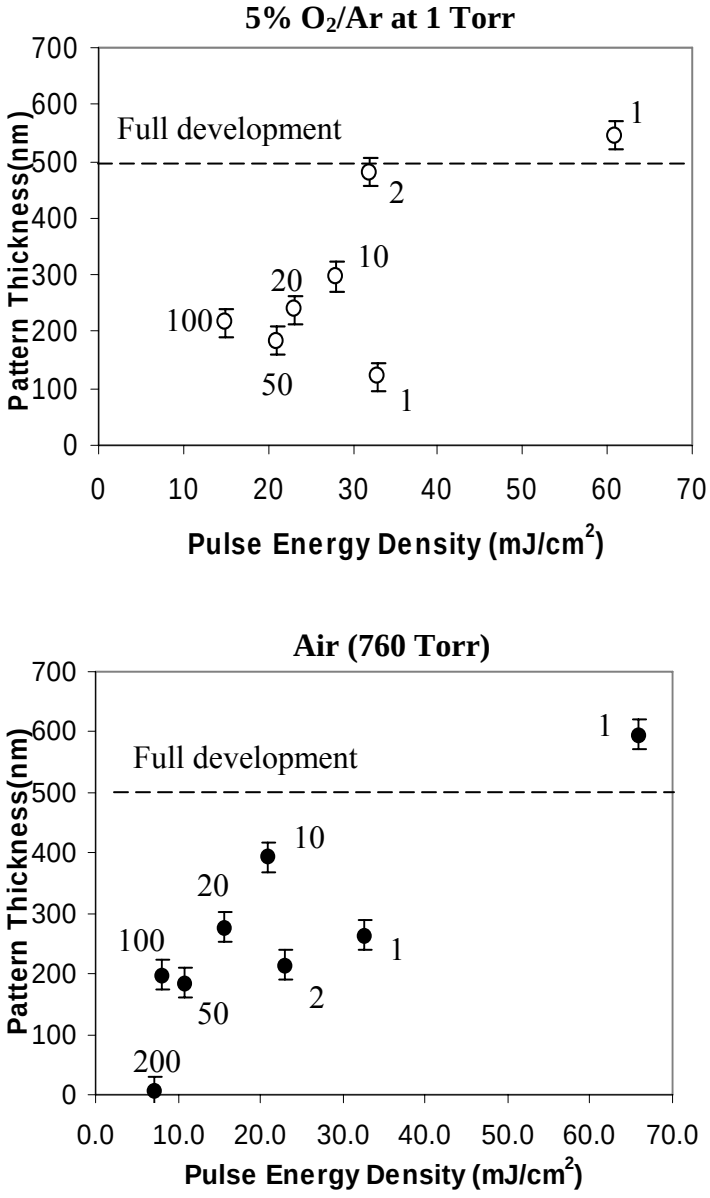

Figure 3.2: Pattern thickness (after plasma-development) vs. pulse energy density for irradiation carried out in 5% O_2/Ar at 1 Torr (a), and in air at atmospheric pressure (b). The a-Si:H resists were deposited using an Argon diluted silane precursor. The number of pulses fired at a particular energy density is indicated. The laser dosages (used in Fig 3.1) were not sufficient for full development of the films in this study.

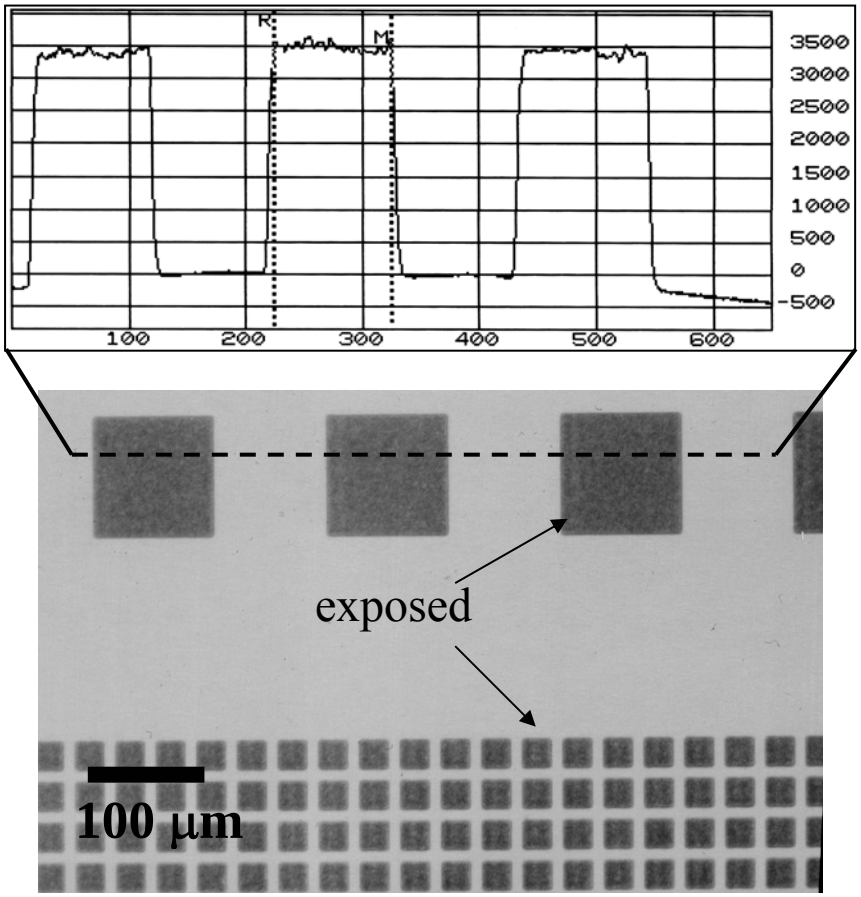

Figure 3.3: Profilometer scan over 100 μm linear array. Pattern created using a single 50 mJ/cm^2 laser pulse in a 1 Torr oxygen containing ambient, followed by partial development etching for 30 min a H_2 plasma. Units of the horizontal and vertical axes are in microns and angstroms, respectively. R.Jacobs et al, [80].

based on measured etch rates of the material. It should also be noted, that significantly more surface roughness occurs in the exposed regions (mesas), than in the unexposed regions (valleys). Rms roughness (R_a), as high as 25 nm was observed in exposed regions, while no more than 1 nm was observed in the unexposed (masked) regions. The image and surface profile of a fully developed pattern are shown in Figure 3.4. Here, a 600 nm thick a-Si:H film was deposited, irradiated in an O_2/Ar ambient using a single laser pulse, and then development-etched in a H_2 plasma

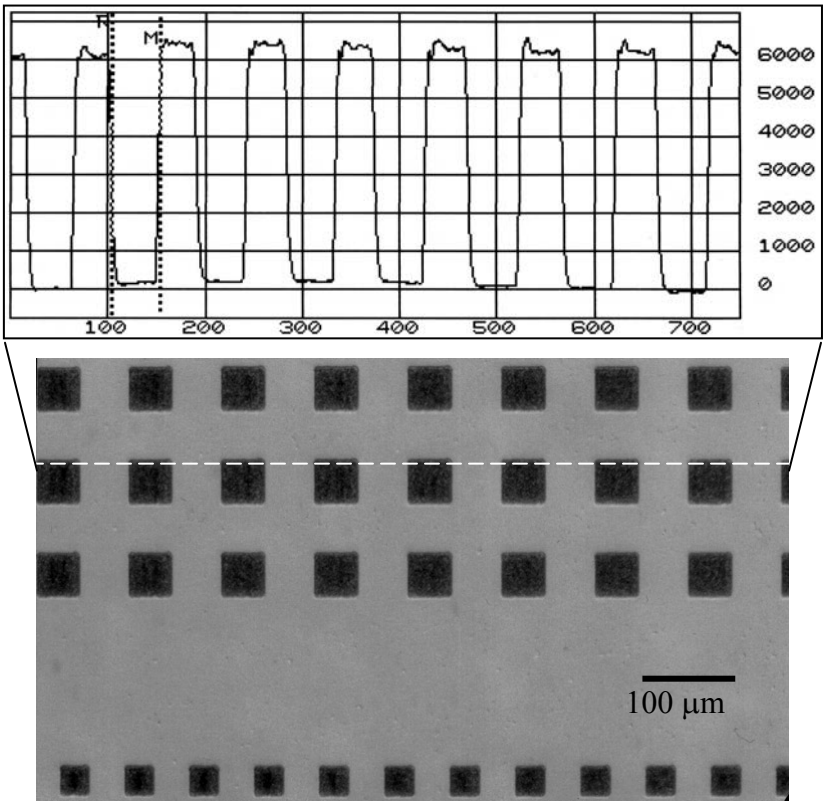

Figure 3.4: Profilometer scan across 50 μm linear array created with 60 mJ/cm^2 laser pulse and hydrogen plasma development-etching for 60 min (full development). (Horizontal and vertical axes are in microns and angstroms, respectively) [62].

for 120 min. The profilometer scan across 50 μm sized features reveals mesa heights over 600 nm in thickness, indicating that the pattern was completely developed. Rms roughness values, (R_a) were similar to those obtained during partial development, suggesting that the H_2 plasma-etch process is not responsible for roughness in the patterned regions of the film. The observation of these rough profiles brought the mechanism for pattern generation into question. The next experiments were performed to determine the single-pulse threshold energy for hydrogen plasma development of 500 nm thick resists. Exposures were carried out in 5% O_2/Ar at 1 Torr and in vacuum at 10^{-8} Torr (see Figure 3.5). As before, 500 nm thick a-Si:H

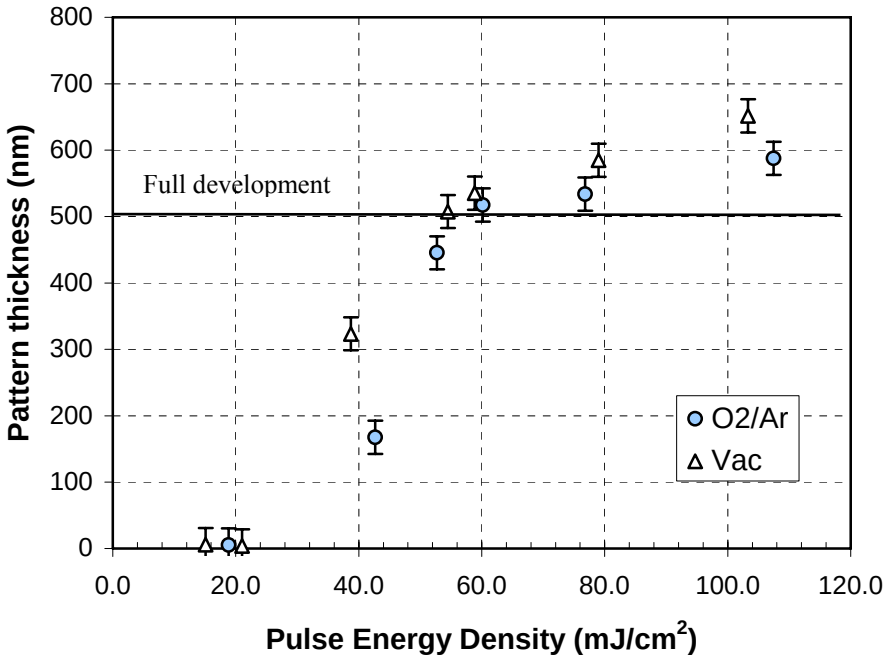

Figure 3.5: Pattern thickness (after resist development) vs. pulse energy density for O_2/Ar at 1 Torr, vacuum at 10^{-8} Torr. The single pulse threshold dose for development of the 500 nm thick films appears to be approximately 60 mJ/cm^2 for both exposure ambients.

films were deposited, irradiated, and then development-etched in a hydrogen plasma. The threshold energy densities (for full resist development) appear to be approximately 60 mJ/cm^2 for irradiation in both the O_2/Ar and vacuum ambients. The results also indicate similar pattern thicknesses for both exposure environments. Furthermore, irradiation at energy densities higher than the threshold resulted in pattern thickness significantly greater than the as-deposited film thickness. These findings are inconsistent with a UV enhanced oxidation mechanism and reveal the need for characterization of the irradiated a-Si:H surfaces.

3.3.1 Characterization of Irradiated Surfaces

The as-exposed surfaces were examined via transmission electron microscopy. Figure 3.6 shows a cross-sectional TEM image of a laser exposed a-Si:H film where 1 pulse was fired at 48 mJ/cm^2. The sample was held in a vacuum ambient during exposure and was not subjected to subsequent hydrogen development-etching. Selected-area electron diffraction (SAD) patterns from three regions of the sample are also shown. The lower SAD pattern simply shows a (011) pattern from the Si substrate, while the continuous rings in the middle SAD pattern confirm the amorphous nature of the as grown a-Si:H layer. However, the discontinuous rings and random spots in the top SAD pattern are indicative of a polycrystalline Si (poly-

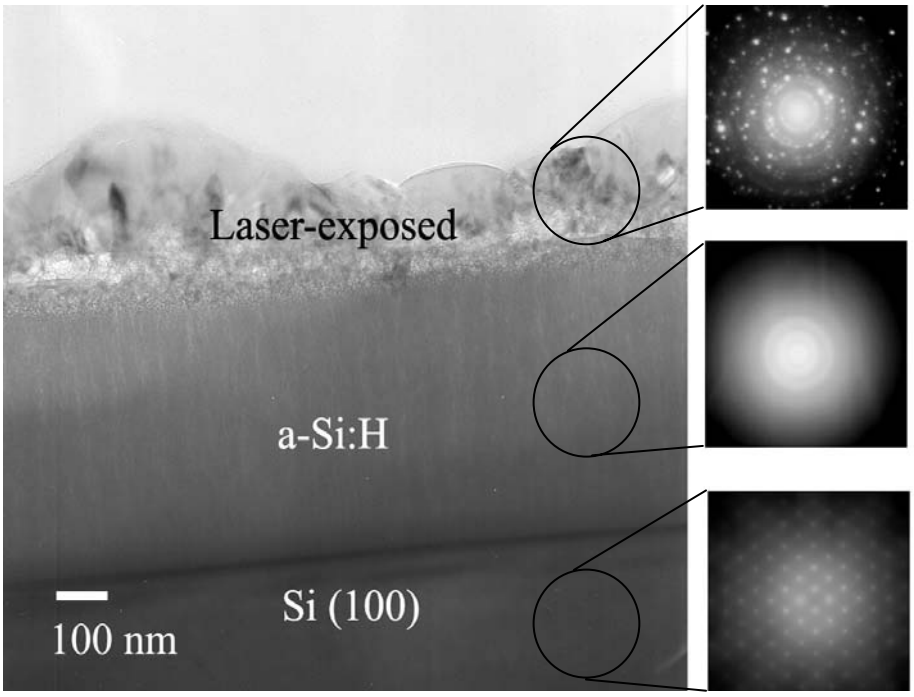

Figure 3.6: Cross-Sectional bright-field TEM image of a-Si:H layer exposed to one pulse at 48 mJ/cm^2. The SAD patterns reveal structure from specified regions.

Si) top layer. This region extends at least 200 nm from the surface, before transitioning to the underlying amorphous Si. It should also be noted that the a-Si:H layer has a columnar morphology. Figure 3.7 shows cross-sectional TEM images of a sample that was exposed and then H_2 plasma development-etched for 45 min. Approximately 250 nm has been removed from the unexposed surfaces, while the exposed regions are essentially unaffected. Thus the laser-induced poly-Si surface functions very well as an etch mask during H_2 plasma development, exhibiting high selectivity. Other experiments [81] have indicated etch selectivities over 1000:1 between a-Si:H and laser-induced poly-Si regions. It should be noted however, that significant undercutting of patterned regions is expected for long etch times. This is due to the isotropic nature of the H_2 plasma etch process. Slight undercutting is visible in the inset of Figure 3.7 at the exposed/unexposed interface.

3.3.2 Comparison of pattern generation mechanisms

Our results reveal a second pattern generation mechanism that can be exploited to form an etching mask for vacuum photolithography. The mechanism described as "UV enhanced oxidation" was utilized in the proof of concept experiments discussed earlier. This method relies on the direct optical interaction between the incident 5 eV photons from the excimer laser and the 2.5-3 eV Si-H bonds [29,78,82,83] on the a-Si:H surface. Irradiation in an oxygen ambient would result in dissociation of Si-H bonds followed immediately by oxidation of the near

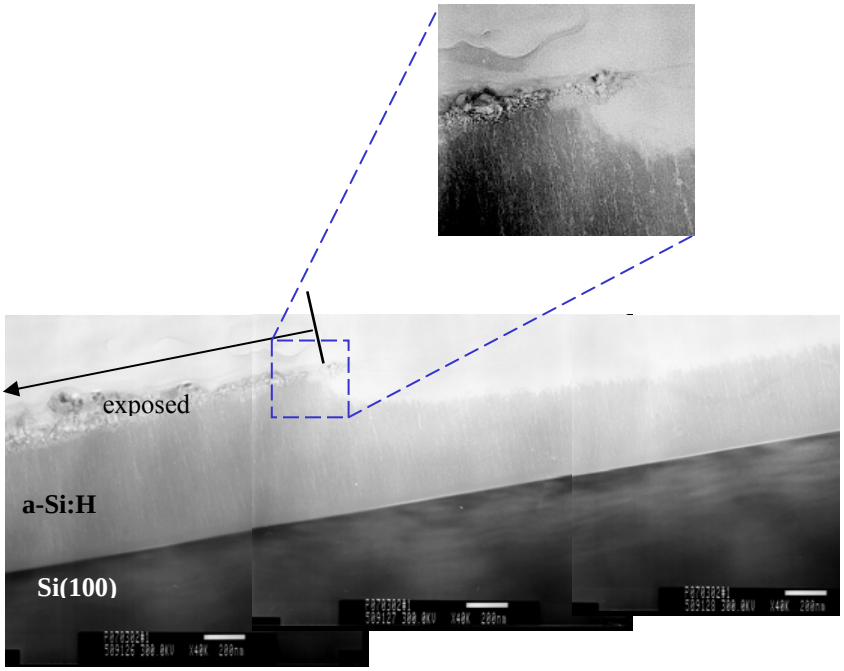

Figure 3.7: Cross-Sectional bright-field TEM image of a-Si:H exposed and then hydrogen plasma-etched for 45 min. Approximately 250 nm has been removed from unirradiated regions. The inset shows undercutting, which is expected due to the isotropic nature of the H_2 etch process.

surface. In the study reported here, the exposed surface region is found to be poly-Si. In this case, the incident pulse energy density must be greater than the crystallization threshold energy (E_{th}), of the film. For energies above E_{th}, the temperature of the surface increases such that rapid H desorption occurs, followed by melting and crystallization. Previous studies have reported energy densities in the range 70-100 mJ/cm^2 required for crystallization of a-Si:H surfaces [84,85]. For the films grown in this study however, E_{th} energy densities as low as ~30 mJ/cm^2 have been observed. This was indirectly shown in Figure 3.2a, where a single pulse energy density of ~33 mJ/cm^2 resulted in some limited selectivity during hydrogen plasma etching. For a single pulse with an energy density below E_{th}, subsequent hydrogen plasma-etching does not result in a measurable pattern thickness, though the actual pattern may be

faintly visible under 10x magnification. In other words, irradiation below the crystallization threshold energy (even in O_2 containing ambients) did not result in a pattern that could be plasma-developed. Laser-induced crystallization (at $E > E_{th}$) was required to establish lithographically definable patterns for all exposure ambients explored in this study.

The gas mixture used for resist deposition is by far the most probable reason preventing the realization of the UV enhanced oxidation mechanism in this work. The use of Ar-diluted SiH_4 may result in a film that is not sufficiently passivated against oxide formation. Previous studies have suggested that Ar dilution causes a columnar morphology, which oxidizes readily because the open structure allows oxygen diffusion [50,86]. Fracture-surface SEM images for a-Si:H films grown under two different conditions are shown in Figure 3.8. Fig 3.8a shows a distinctly columnar microstructure when a-Si:H is grown under conditions of high rf power and using SiH_4 diluted to 5% in Ar. On the other hand, a-Si:H grown using pure silane precursors and low rf power (Fig 3.8b) yields a smooth and uniform morphology. In the present study, relatively low rf power was used during deposition, but the precursor gas was approximately 6.5% SiH_4 in Ar. Note that a columnar-like microstructure was observed in the TEM micrographs (Figures 3.6 and 3.7). Significant oxidation may have occurred over the a-Si:H surface when O_2 gas was leaked into the chamber prior to laser irradiation. The internal surfaces and voids (associated with columnar morphologies) would make it relatively easy for oxygen to penetrate and diffuse through the a-Si:H film. Oxygen atoms could then attach themselves to the amorphous network at Si dangling bonds or even strained Si-Si

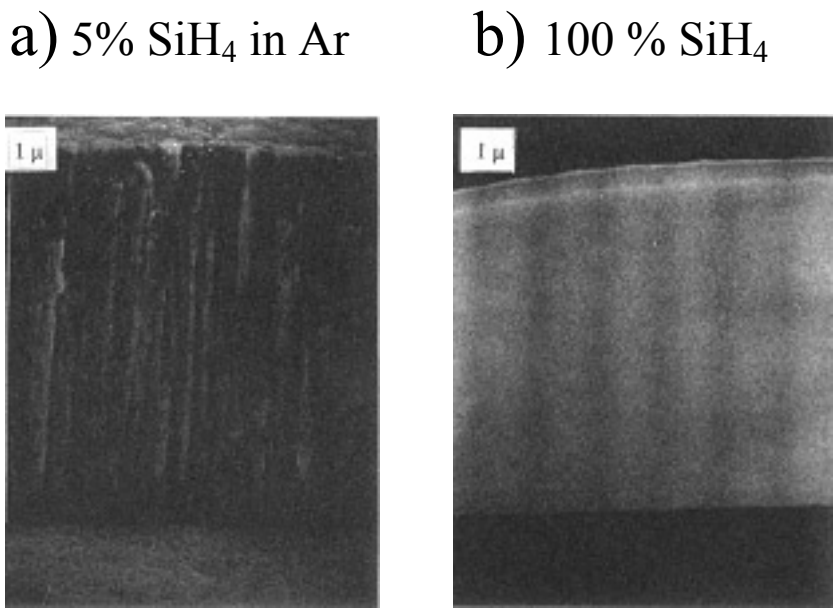

Figure 3.8: Fracture-surface SEM images grown under conditions of a) high rf power and heavy Ar dilution (5% Silane in Ar), and b) low rf power and pure silane (reprinted from J.C. Knights et al [50]).

bonds [86]. In this case, laser pulses below E_{th} energy densities could not generate a distinct oxide pattern on the surface and thus "UV enhanced oxidation" could not be utilized. Lithographic patterns were formed only by using laser pulses above E_{th} to crystallize selected regions of the surface. The schematic diagram in Figure 3.9 illustrates this theory and experiments performed in the following section attempt to investigate it further.

3.4 Effect of gas concentration on film properties

In this section we directly investigate the effects of argon-dilution on a-Si:H film properties and on the resist process. 500 nm thick films were deposited using

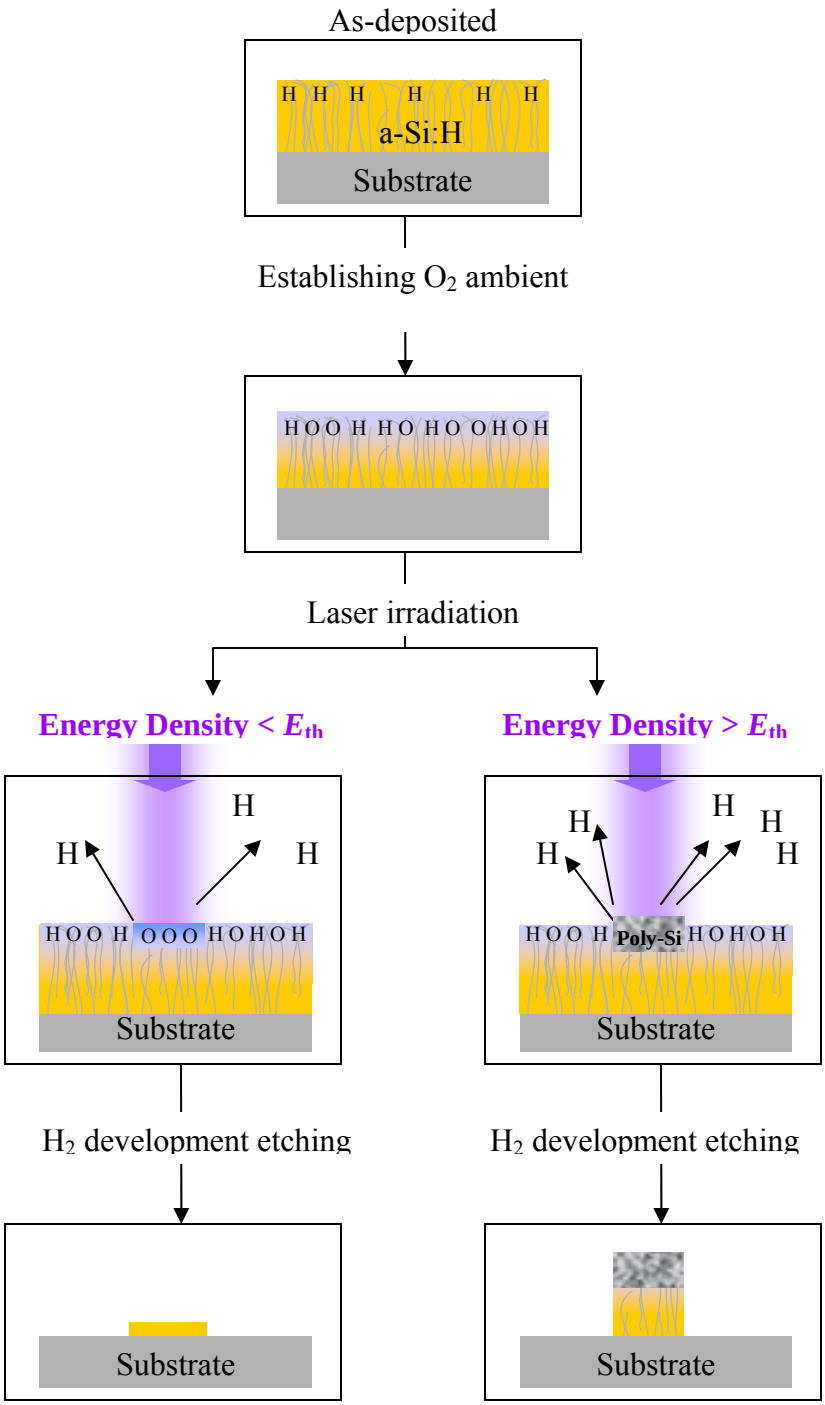

Figure 3.9: Proposed theory: a-Si:H deposited via Ar diluted SiH_4 precursors show a highly columnar and defective morphology so that significant oxide growth occurs upon exposure to O_2 containing ambients. In this case, a laser induced oxide ($E < E_{th}$) does not produce a viable means for patterning. Rather, a laser induced poly-Si surface ($E > E_{th}$) is required to obtain sufficient selectivity during subsequent H_2 plasma-etching.

different silane concentrations; $[SiH_4]/[SiH_4+Ar]$ = 10%, 7.5%, 5.0%, 2.5%, 1.0%, while other deposition parameters were fixed as described in section 3.2. It is worth noting that the SiH_4 source gas cylinder already contains a mixture of 10% silane in argon, and that additional argon (from a second gas cylinder) is introduced in the PECVD chamber through a needle valve (see chapter 2.2.1). Thus, to obtain the gas concentrations specified above, the SiH_4+Ar flow rate (i.e., from the first gas cylinder) was set to 100, 75, 50, 25, and 10 sccm, while the Ar needle valve was adjusted to give the total chamber pressure equivalent to that for 100 sccm SiH_4/Ar (with no additional Ar flow). In this way, a flow rate of 25 sccm (for example), corresponds to a concentration 2.5% silane in argon. The different flow rates involved here also resulted in different deposition rates, so that calibration was necessary to ensure the same film thicknesses were obtained for the different samples. A cleaved Si wafer was used as a physical mask to establish a reference thickness for direct measurement (via profilometry) after deposition. In-situ thickness estimation using HeNe laser interferometry was also carried out.

Infrared absorption spectra for the samples described above are shown in Figure 3.10. The vibrational spectra of a-Si:H alloys have been well characterized by Lucovsky et al and others [75]. For reference, the various Si-H bonding modes, and their respective frequencies are presented in Figure 3.11. There are several features of interest in Figure 3.10. The vibrational modes at approximately 2000 and 630 cm^{-1} wavenumbers, correspond to Si-H stretching and bending, respectively. $Si-H_2$ and $Si-H_3$ bending modes (rock or wag) have also been attributed to the feature at ~630 cm^{-1}, but the $Si-H_2$ stretching mode is exclusively associated with ~2090 cm^{-1}. In

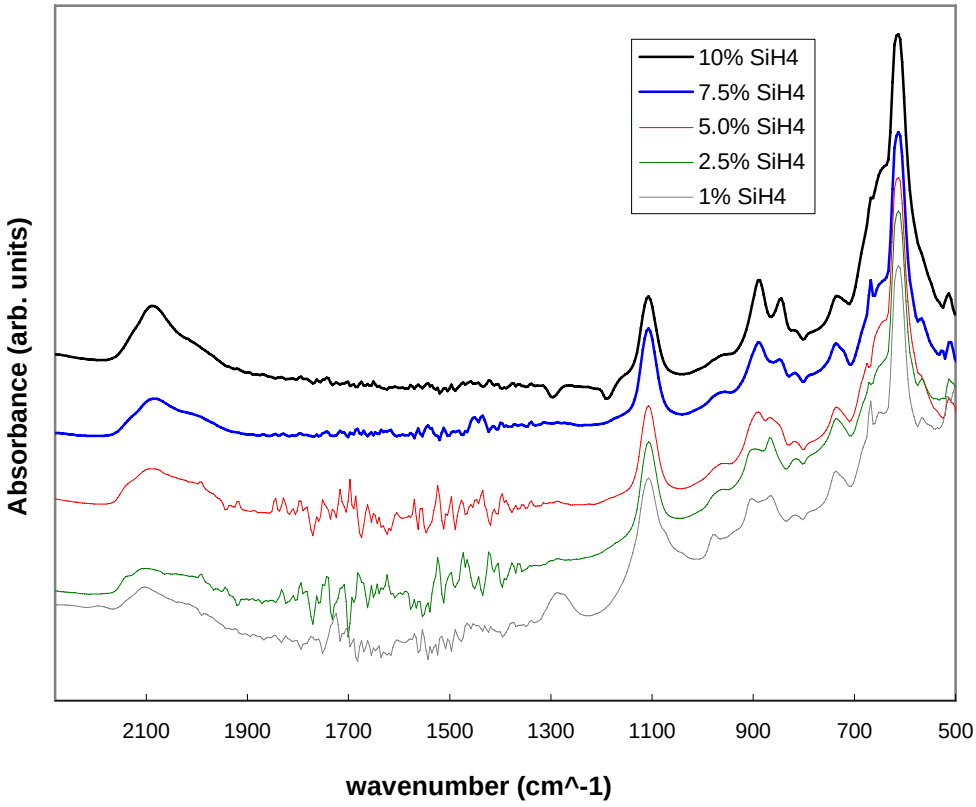

Figure 3.10: IR absorbance spectra for ~500 nm thick a-Si:H films deposited with different silane concentrations (using argon as the diluent).

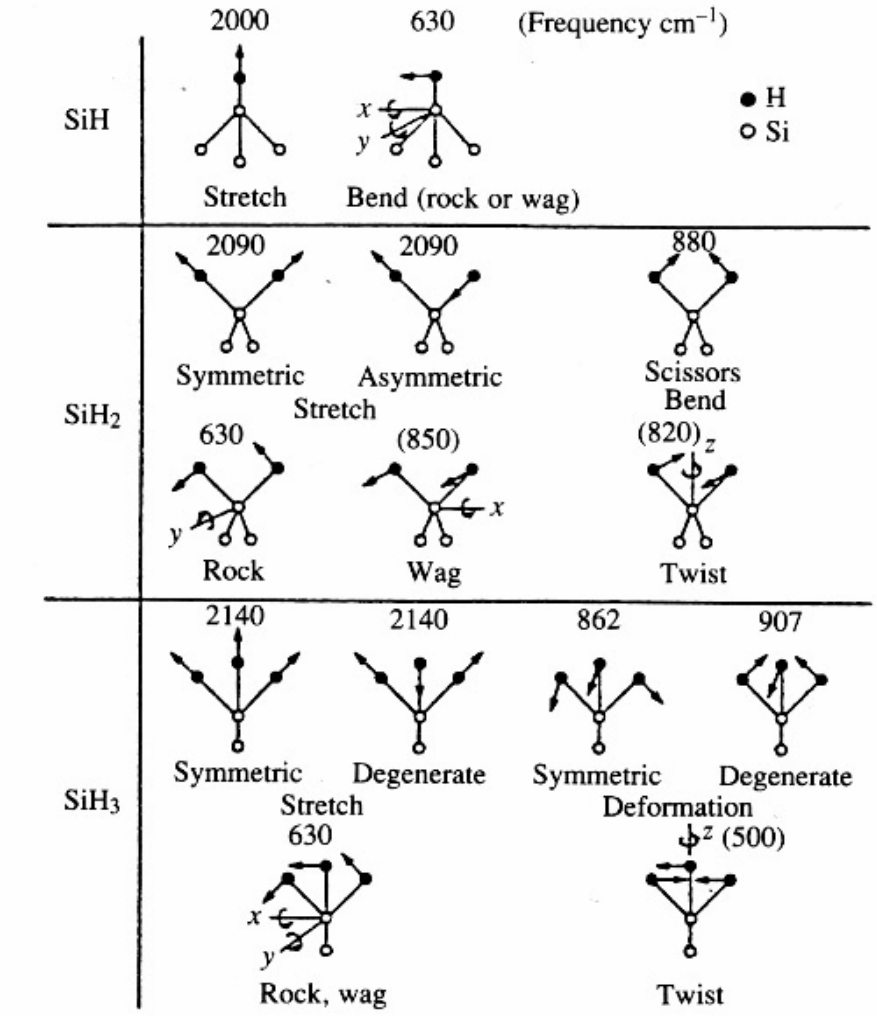

Figure 3.11: The primary Si-H vibrational modes for SiH, SiH_2, and SiH_3 groups with calculated frequencies (in wavenumbers, cm^{-1}) indicated [75].

addition, a doublet occurs at approximately 850 and 907 cm^{-1}, which has been attributed to Si-H_2 wagging or Si-H_3 degenerate deformation, respectively. The most obvious trend in Figure 3.10 is that the absorption strengths for the stretching modes in the range 2000-2090 cm^{-1} decrease with increasing dilution of SiH_4. Integration of the area under this feature showed decreasing values as the relative silane concentration is decreased (Figure 3.12a). The 2090/2000 cm^{-1} peak height ratio also decreased with smaller silane concentrations. A notable change is also observed for the doublet vibrations present in the range ~840-915 cm^{-1}. For the sample deposited with 10% silane, a sharp peak occurs at 907 cm^{-1}, which is stronger than the peak at 850 cm^{-1}. As the silane percentage is decreased however (7.5 and 5.0%), the peak at 907 cm^{-1} becomes less pronounced, and for the 2.5 and 1% silane samples, the 850 cm^{-1} peak becomes dominant. The decreasing vibrational modes (907 and 2090 cm^{-1}) are associated with Si-H_3 and Si-H_2 bonding (see Figure 3.11). These findings suggest that the H_2 content of the a-Si:H films decreases with decreasing SiH_4 content in the depositing gas. The infrared absorption at a frequency ω is related to the hydrogen concentration N_H, by

$$N_H = A_\omega I_\omega = A_\omega \int \left[\frac{\alpha(\omega)}{\omega} \right] d\omega \qquad (3.1)$$

where α is the absorption coefficient, I is the integrated intensity at ω, and A is a proportionality constant dependent on the particular frequency range of interest [87]. However, Lucovsky et. al and others, caution that the total H_2 concentration in a given sample may not always be simply proportional to the relative absorption strengths of these vibrational modes [75]. Nevertheless, other studies in which the infrared absorption is actually calibrated with the total hydrogen content (measured

by hydrogen evolution), have shown the integrated intensity of the 630 cm^{-1} line may be the best measure of H concentration [74,88]. Figure 3.12b shows the integrated intensity corresponding to the 630 cm^{-1} line (from Fig. 3.10) as a function of silane percentage. The observed trends in Fig 3.12(a & b) confirm that the total hydrogen content does in fact decrease as the depositing gas is diluted in Ar.

Another important feature from Figure 3.10 is the relatively strong absorption line in the range 1040-1150 cm^{-1}. For comparison, the absorption frequency of oxygen in bulk single crystal Si pulled from the melt is 1100 cm^{-1} [89]. Lucovsky et al reported that absorptions in the range 900 to 1100 cm^{-1} may be due to Si-O vibrations and that features between 2100 and 2250 cm^{-1} may be attributed to SiH vibrations in which the Si atom is bonded to one or more O atom [75]. In Figure 3.10 a small shoulder at ~2150 cm^{-1} begins to appear in the 5% SiH_4 sample and is most apparent in the 2.5% SiH_4 sample, suggesting the presence of more oxygen with increasing SiH_4 dilution. For better observation of the relative oxygen concentrations however, the integrated intensities in the range 1040-1150 cm^{-1} are plotted as a function of silane concentration (Figure 3.13). A significant increase in intensity is seen particularly in the 2.5% and especially in the 1% silane sample. These combined observations confirm that Ar dilution of silane (during PECVD a-Si:H deposition) tends to result in films with lower hydrogen concentration and in turn, higher oxygen content upon exposure to a O_2 containing ambient. It is important to note that the IR spectra presented here was obtained at least one day after removal from the vacuum chamber (i.e. exposure to atmosphere). However, Street reports that a-Si:H films with columnar morphologies (which are associated with high defect densities) should

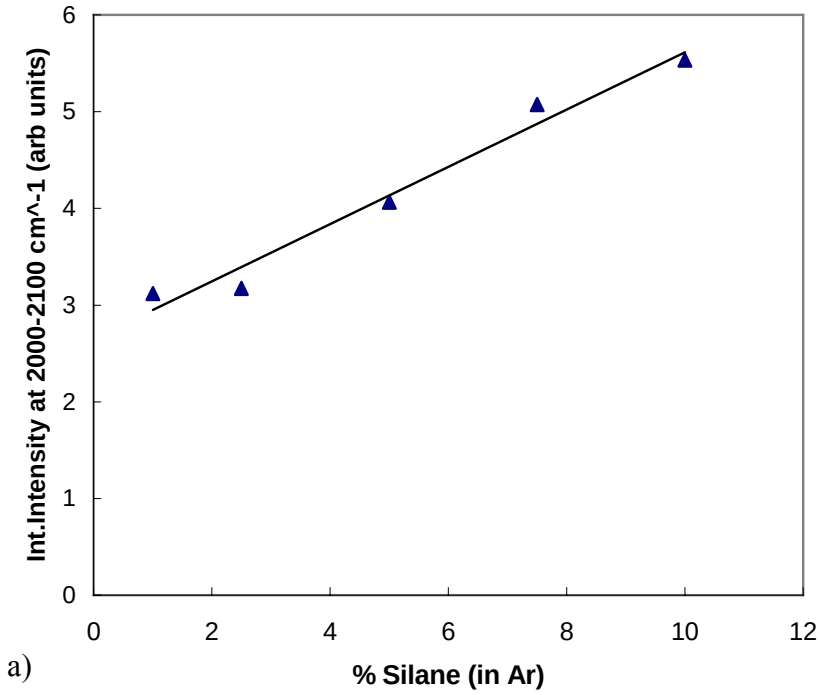

a)

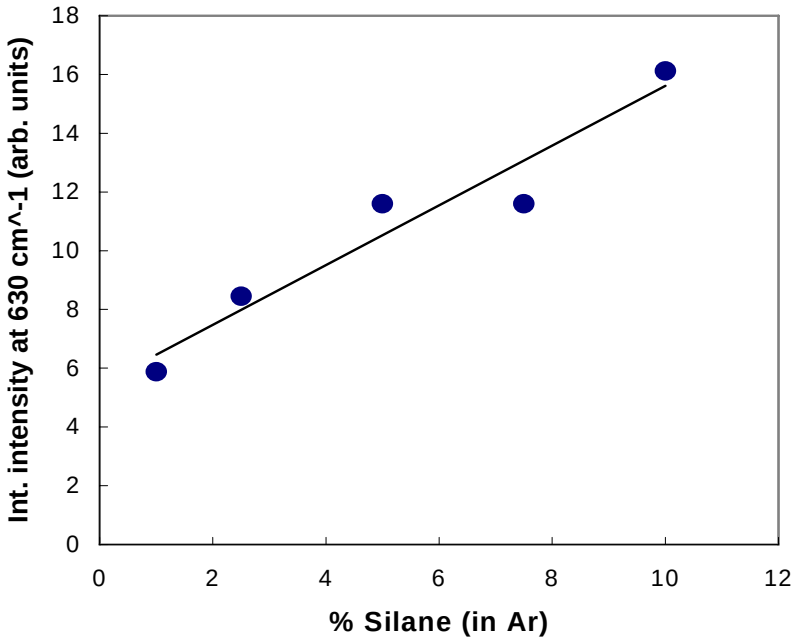

b)

Figure 3.12: Integrated intensity for IR absorption at wavenumbers 2000-2100 cm^{-1} (a) and for 630 cm^{-1} vs. silane concentration (b). See Fig 3.10 for vibrational modes associated with the respective frequencies. The trend lines suggest a linear dependence.

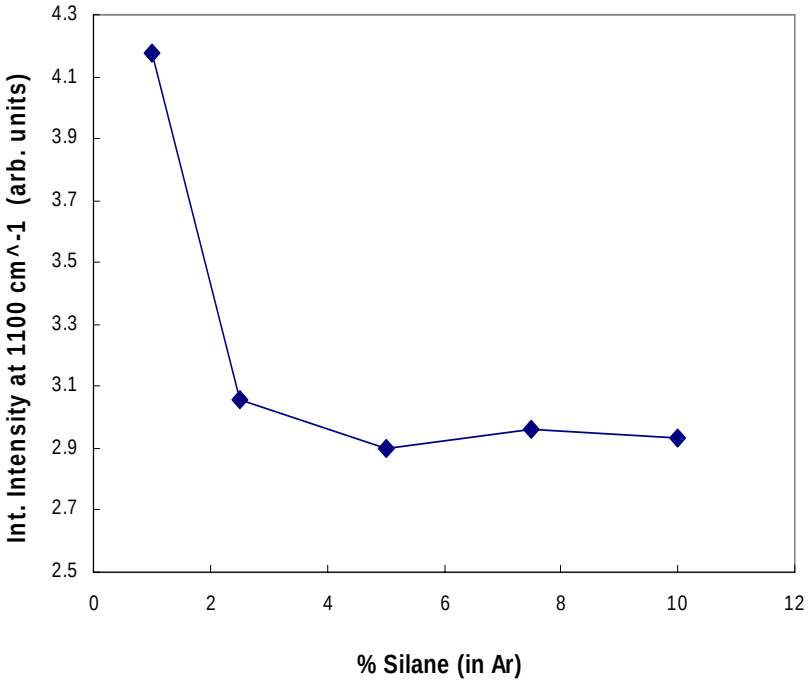

Figure 3.13: Integrated intensity for IR absorption at 1100 cm^{-1} vs. silane concentration (see Fig 3.10). Strong absorption due to Si-O vibrations are observed particularly for samples deposited with 1 and 2.5 % silane.

oxidize rapidly immediately upon being exposed to air [90]. Thus the films used for the IR spectra shown above, are probably similar to those used when attempting to obtain UV generated oxide patterns in a 1 Torr O_2 ambient (or at atmosphere).

Next, we directly investigated the effects of silane concentration (during deposition) on the hydrogen plasma etch rate. All in-vacuo processing was carried out here to suppress variables such as contamination and/or unintentional oxidation, which may affect the etch rate. In addition, the 500 nm thick films were each irradiated through a patterned mask, with a single pulse (for each pattern) ranging from 10 to 65 mJ/cm^2. The thickness of the patterns after 90 min H_2 plasma etching,

was used to measure the etch rate. Pulses with energies below the crystallization threshold did not result in patterns with measurable thicknesses (after plasma etching) for any of the samples studied. Thus, etch rates were calculated only from patterns where the incident pulse energy was 65 mJ/cm^2 (above the threshold). Figure 3.14, shows the H_2 plasma etch rate vs. silane concentration, for samples exposed in vacuum (10^{-7} Torr) and 10% O_2/Ar at 1 Torr. For samples deposited with 10% silane, etch rates in the range 0.9-1.2 Å/sec were obtained for both vacuum and oxygen exposure ambients. This is roughly similar to etch rates observed for samples deposited with 6.5% silane concentration (used throughout most of this work). For samples deposited with 2.5% silane, the H_2 plasma etch rate was also in the ~1.0 Å/sec range for vacuum exposure, but was only ~0.2 Å/sec for exposure in the O_2 containing ambient. These findings indicate that the a-Si:H etch rates are affected by the silane concentrations used during deposition, and can be extremely low for the lowest concentrations. The difference in etch rate observed for 2.5 and 10% SiH_4 samples exposed in the O_2 ambient, points to possible differences in material composition and microstructure. A lower hydrogen content in the 2.5% SiH_4 sample (see fig. 3.12) means less hydrogen passivation, and a greater likelihood of native oxide growth after oxygen is leaked into the chamber. This situation would result in a lower etch rate (in H_2-plasma), as the material becomes more SiO_2-like.

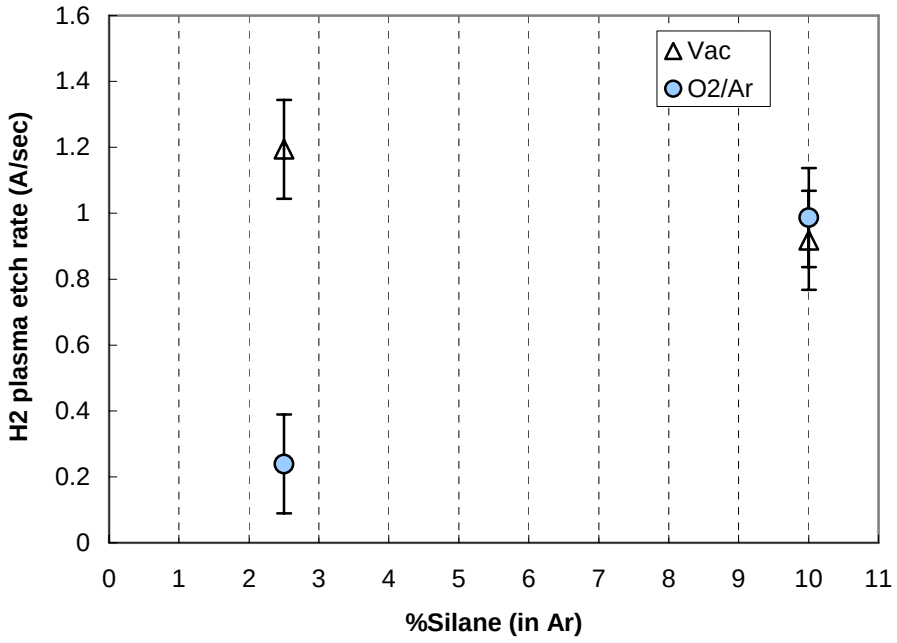

Figure 3.14: Hydrogen plasma etch rate (Å/sec) for samples deposited using 2.5 and 10% silane concentrations, and then exposed in either O_2/Ar at 1 Torr or vacuum at 10^{-8} Torr. A difference in etch rate of 0.2 Å/sec is not experimentally significant.

3.5 Conclusions

The focus of the work presented here, was to study the effects of argon dilution (in the depositing gas) on a-Si:H films, and on its use in an experimental vacuum lithography technique. The results show both benefits and disadvantages to the use of heavy Ar dilution during a-Si:H deposition. While undesirable SiH_x dust formation can be decreased, the resulting films show a strongly columnar morphology (as seen via TEM) that is suggestive of internal surfaces and voids. Through IR absorption spectra, it was shown that the hydrogen content of these films is decreased as the depositing SiH_4 gas concentration is decreased. As a consequence of lowered

hydrogen content and a strong columnar morphology, the films are less passivated against oxidation relative to films deposited from precursors with higher SiH_4 concentration. Less hydrogen most likely means more Si dangling bonds, so that native oxide growth is more rapid and extensive in samples with the least hydrogen content. These findings are consistent with the low H_2 plasma etch rates observed for samples that were initially deposited with lower SiH_4 concentrations and then exposed in oxygen containing ambients. Finally, these results explain the apparent difficulty in generating viable UV enhanced oxide patterns that could be plasma-developed with sufficient etch-selectivity.

On the other hand, our results also demonstrate the use of laser generated poly-Si surfaces for use as an etching mask for lithography. When the laser energy density is increased above E_{th}, the a-Si:H film crystallizes and provides a means for achieving H_2 development-etch selectivities over 1000:1 for unexposed and poly-Si regions. However profilometry and TEM also showed that the poly-Si regions were very rough, and if transferred to an underlying device layer (in subsequent etching steps), this roughness could lead to poor device performance. The following two chapters discuss techniques to either decrease the rms roughness or to add a separate etch step (after mesa-etching), to remove residual a-Si:H.

Chapter 4

Reduction of laser-induced surface roughness

4.1 Introduction

In the previous chapter, we discussed the effects of argon-dilution on a-Si:H film properties and showed how these properties affect the a-Si:H resist process. Namely, it was shown that laser-induced crystallization of the resists is required in order to obtain sufficient selectivity during subsequent H_2 plasma development-etching. Thus, excimer laser energy densities above the crystallization threshold energy (E_{th}), are essential if the material is to function as a resist layer. While the laser-induced poly Si patterns stand up very well to H_2 plasma etching, they do introduce another obstacle. That is, the surfaces are extremely rough, relative to unirradiated (as deposited) a-Si:H surfaces. This roughness was discussed briefly in section 3.3, and is visible in profilometer scans (Figures 3.3 and 3.4) and even in cross-sectional TEM images (Figure 3.6 and 3.7).

The roughness that is introduced during laser irradiation persists throughout the H_2 plasma-development process, and (as will be shown in chapter 5) is exacerbated during ECR mesa-etching. The complete a-Si:H resist technique was originally designed so that mesa etching in underlying HgCdTe/CdTe layers, and a-Si:H removal, take place within one processing step. Therefore the roughened surfaces from developed a-Si:H patterns, would be transferred to underlying active

device layers. This could potentially cause reduced or poor diode performance. The fabrication of both HgCdTe p-n diodes and Cd/CdTe schottky diodes, require that a contact metal be deposited onto the mesa surfaces. The photodiode array would eventually be mated unto a read out integrated circuit (ROIC), via the metal contacts. In this way, photoinduced current from the detector array is converted into a voltage [91]. Any roughness at the semiconductor mesa surfaces, may decrease the conduction of charge carriers to the deposited contact metal.

To decrease the surface roughness in laser-crystallized hydrogenated amorphous silicon thin films it is necessary to understand its origins. If a uniform laser pulse is assumed, there are essentially two material properties, which may contribute to roughened surfaces. First, recall that the a-Si:H films contain a large amount of hydrogen (up to 50 at%) as a natural consequence of the relatively low temperatures at which they are deposited [46,48]. Upon rapid heating, such as is the case during laser irradiation, the hydrogen is released from the film and forms bubbles, which will literally explode at sufficient H_2 concentrations. Secondly, internal voids and other defects already present in the material, may act as individual nucleation centers for grain growth following melting of the film. As the molten film cools and solidifies, the grains impinge on each other, creating surface undulations and grain boundaries, which may contain voids or trapped liquid. In other reports the roughness induced by laser-crystallization has been correlated to the initial thickness of the film [92]. As we will show however, this relationship appears to be true only for films that are irradiated with laser fluences large enough to melt (and crystallize) the entire film.

In this chapter we explore techniques to reduce the surface roughness induced by excimer laser-crystallization of a-Si:H. Ideally, the goal is to decrease the roughness such that: $R_a^{\text{exposed}} \approx R_a^{\text{as-deposited}}$. The most commonly used technique found in the literature is conventional furnace annealing for several hours at 450 ºC prior to laser irradiation [93]. In this way, most of the hydrogen is removed and laser crystallization can then be performed without explosive H_2 evolution from the film. While this technique may significantly reduce the roughness of the crystallized regions, the annealing temperatures involved are much greater than the limits imposed by our project requirements. Namely, thermal degradation of HgCdTe epilayers may occur at temperatures as low as 80 ºC. Others have investigated the use of different laser treatments to reduce roughness. Toet *et al*. showed that surface roughness could be reduced by using multiple laser pulses [92]. In the same article, a smoothing procedure was also demonstrated, where a pulse with an energy density above the full-melt threshold (FMT) is followed with a pulse below the threshold energy. Finally, Ping Mei et al, demonstrated a simultaneous laser dehydrogenation and crystallization technique where multiple exposures are used with incremental increases in the laser energy density [94,95]. While the intent was not necessarily to reduce Ra, the hydrogen removal rate was reduced, and "explosive crystallization" was suppressed. With the exception of 450 ºC furnace annealing, this chapter employs the techniques described above (and others), in attempts to decrease the laser-induced surface roughness on a-Si:H resists.

4.2 Experimental Procedure

Amorphous hydrogenated Si films were deposited via PECVD to thicknesses in the range 300 to 600 nm. Other deposition parameters were fixed at 3 W rf power, 50 °C substrate temperature, and an overall pressure of 500 mTorr. The SiH_4 gas concentration was fixed at approximately 6.5% in argon (the standard for deposition throughout most of this thesis). As in chapter 3, films were grown either on bare Si(211), or thermal oxide Si(100) substrates, depending on the specific experiment. For example, bare Si substrates were best for subsequent IR absorption (FTIR) measurements, while growth on thermal oxide Si substrates was best for in-situ thickness monitoring (via HeNe laser interferometry). The different substrates used here, do not affect the a-Si:H resist processing. For more details on film growth, see chapter 2.2.1.

Excimer laser irradiation was carried out in the load-lock to the PECVD chamber, after deposition of the a-Si:H resist. While most exposures were carried out in vacuum at 10^{-7} Torr, other ambients were used to examine their possible influence on roughness. The energy density incident on the samples was systematically varied from approximately 10 to 100 mJ/cm^2 per pulse. With a nominal pulse length of 20 ns, this is equivalent to a peak power density of ~0.5 to 5 MW/cm^2. For experiments involving multiple pulses, the Lumonics PM844 KrF laser allowed repetition rates up to 10 Hz (for highest output energies) and 50 Hz for lower energies.

Irradiated surfaces were inspected via optical microscopy and rms roughness, (R_a) was measured using a stylus profilometer. TEM and FTIR analyses are also

employed to understand the effects of different laser treatments on the a-Si:H surfaces.

4.3 Effect of Laser Fluence on Roughness

The pulse energy density was the most obvious means to control roughness at the irradiated surfaces. Figure 4.1 shows R_a vs. pulse energy density as measured via profilometry. An a-Si:H film was deposited on a Si(100) substrate and irradiated in vacuum with a single pulse at different energy densities. R_a was measured across a 100 μm feature for each exposed pattern. The general trend shows increasing R_a as a function of energy density, with values as high as 28 nm for a ~100 mJ/cm^2 pulse. Miscellaneous data points are also plotted for exposures on other a-Si:H substrate systems, and do not indicate an obvious dependence of laser-induced roughness on the starting substrate. As the energy density decreases, the roughness decreases to values as low as 7 nm. However the average roughness of an as-deposited a-Si:H layer is typically no more than 0.5 to 1.5 nm. Unfortunately even if pulse energies lower than that shown in Fig 4.1 could further reduce R_a, they may not produce patterns that provide sufficient etch selectivity for full resist development (depending on the thickness needed). For instance, our data suggests that a pulse energy density of roughly 40 mJ/cm^2 would be required to fully develop a 300 nm thick a-Si:H resist layer during subsequent H_2 plasma etching, (see Fig. 3.5). The roughness induced at this energy density however, is still an order of magnitude greater than that for the as-deposited resist.

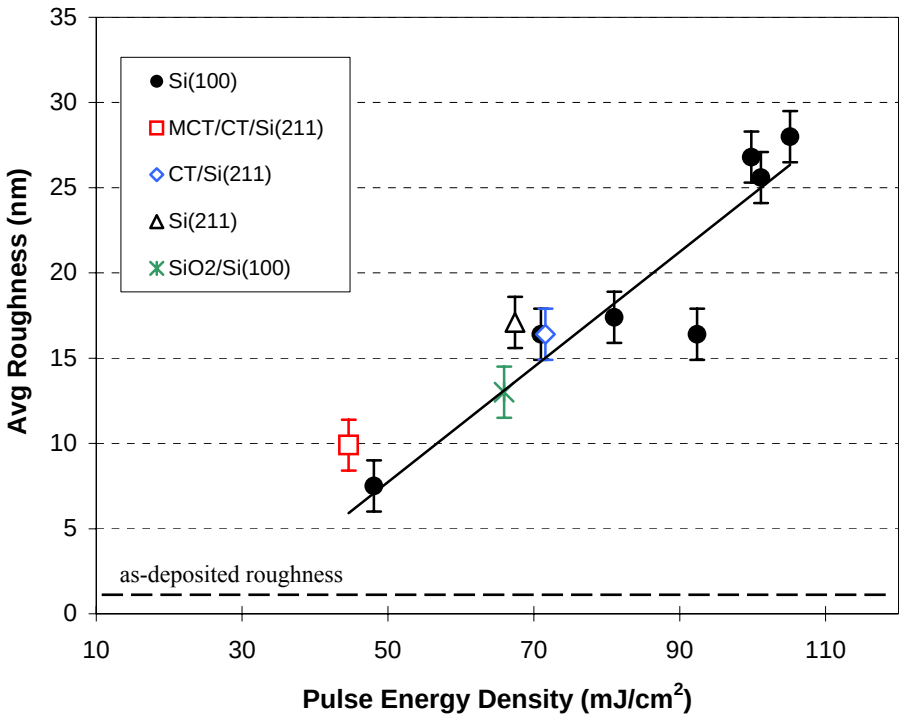

Figure 4.1: Average surface roughness vs. pulse energy density for an a-Si:H layer deposited on a Si(100) substrate and irradiated in a vacuum ambient. Each data point is an average across a 100 μm area of the irradiated surface. Other data points show no evidence of starting substrate dependence. Note, the single pulse threshold for crystallization has been estimated at $E_{th} \approx 30$ mJ/cm^2 (see Figures 3.2 and 3.5). At energy densities $< E_{th}$, the surface roughness is typically equal to the as-deposited roughness.

For energy densities above the crystallization threshold ($E_{th} \approx 30$ mJ/cm^2), significant grain growth occurs as the near surface is rapidly heated above the melting temperature and then cools. For films irradiated above E_{th}, ~100 nm scale surface texture is observed even prior to development-etching. Fig 4.2 shows a cross-section TEM image of an a-Si:H film grown to 300 nm thick, and then exposed using a single pulse at 55 mJ/cm^2. No H_2 plasma development-etching or any further processing

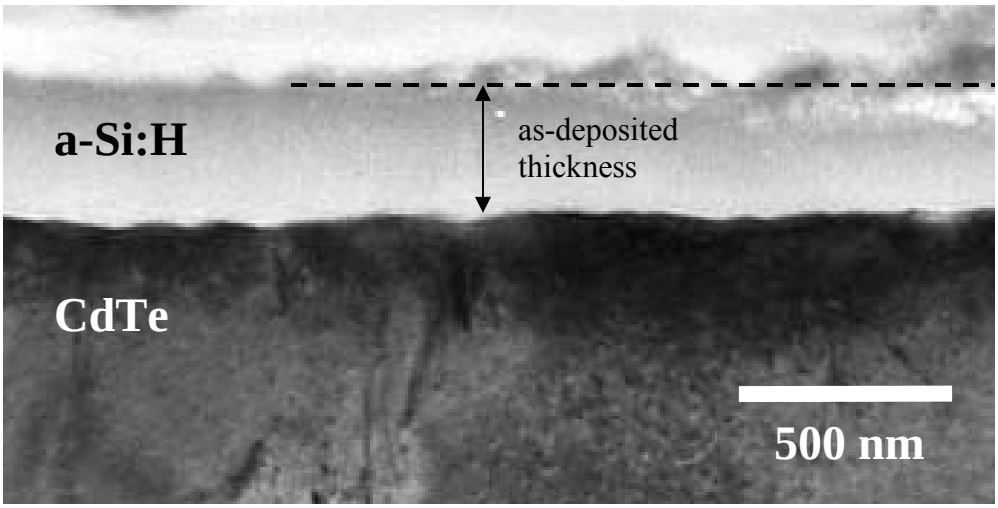

Figure 4.2: Cross-section TEM image of an a-Si:H layer grown to ~300 nm and irradiated using a single pulse of 55 mJ/cm^2. No development etching or further processing was carried out. The dashed line through the irradiated (poly-Si) region indicates the as deposited film thickness.

was carried out. The image shows that the laser-induced poly-Si grains extend above and below the surface of the as-deposited film. On average, this grain growth extends the total film thickness to 400 nm. Thus, we find that the pulse energy density influences not only the rms surface roughness, but also the total resist thickness. Figure 4.3, shows the average pattern thickness before and after full development of a 300 nm thick layer. The data shows that smaller pulse energy densities result in lower pattern thicknesses for both as-exposed and as-developed films. For a 40 mJ/cm^2 pulse, an average height of 70 nm is measured over the as-exposed surface, compared to 230 nm for exposure using a 95 mJ/cm^2 pulse. Note that these heights represent the increase in film thickness due to crystallization, and are not the total thickness of the crystallized region. After 60 min H_2 plasma etching, the patterns generated using 40 and 95 mJ/cm^2 pulses had measured thicknesses of 380 nm and

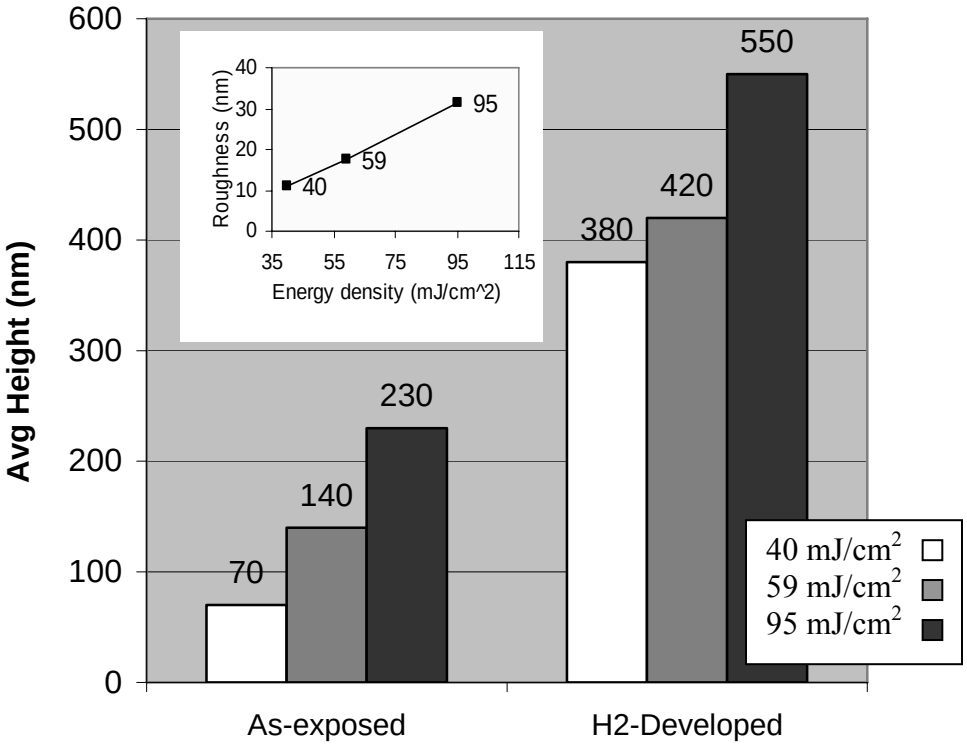

Figure 4.3: Average pattern thickness before and after full hydrogen plasma development of a 300 nm thick a-Si:H layer. Patterns are generated using single laser pulses of 40, 59 and 95 mJ/cm^2. The Inset shows the average roughness measured via profilometry, across a 100 μm area for each pattern

550 nm, respectively. Although R_a also decreases with smaller energy densities (Fig 4.3 inset), a significant change in R_a due to H_2 development-etching has not been observed. On the other hand, a correlation has been observed where the as-exposed thickness (due to grain growth) is typically 6 to 8 times the measured R_a.

The pulse energy densities used in Figures 4.1 to 4.3 are all above the observed crystallization threshold ($E_{th} \approx 30$ mJ/cm^2). Though single pulse energy densities of at least 40 mJ/cm^2 are necessary for sufficient development of the a-Si:H resist, granular surface texture (roughness) is observed for all energies $\geq E_{th}$. In

comparison, the surface texture obtained for energies below E_{th}, remain smooth with measured rms roughness equal to that of an as deposited a-Si:H layer. In fact, a UV grown oxide on an a-Si:H film surface is expected to show just that [56]. In Figure 4.4 below, optical micrographs are shown for two patterns generated on the same a-Si:H layer using a single pulse at 76 mJ/cm^2 (a), and 21 mJ/cm^2 (b). The exposures are carried out in air to promote "UV enhanced oxidation" (at the lower energy density). The high energy density pulse (a), produces strong granular surface texture and high roughness (R_a = 33 nm) so that very sharp contrast is observed. On the other hand, the pattern generated using $E < E_{th}$, shows a very smooth surface due to low roughness (R_a = 0.7 nm) and hence very low contrast is visible (Fig 4.4b). The contrast in this pattern is more likely due to selective oxide growth at the surface of the film. However the a-Si:H resist thickness after H_2 plasma etching was merely 12 nm, which is inadequate for subsequent pattern transfer to underlying epilayers.

a) E_D = 76 mJ/cm^2 b) E_D = 21 mJ/cm^2

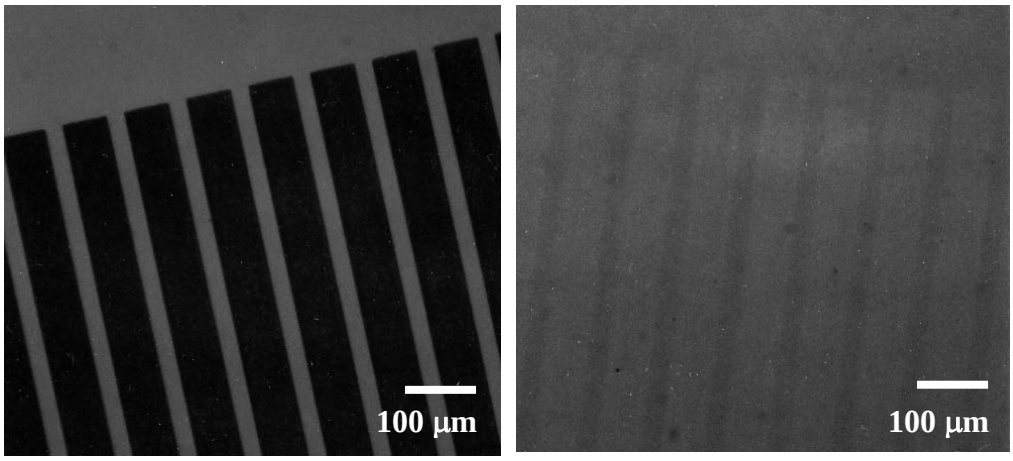

Figure 4.4: Optical micrographs for two patterns irradiated at a) 76 mJ/cm^2 and b) 21 mJ/cm^2. Exposures were carried out in air to promote oxidation (particularly in b).

We have also investigated the dependence of roughness on multiple exposures (at constant E_D), as this method was shown to reduce roughness by Toet et al [92]. In Figure 4.5, R_a is plotted vs. the number of pulses for a constant energy density of ~63 mJ/cm^2 (a), and as a function of energy density (b), where the number of shots fired at each E_D is fixed at 10. The results indicate that laser-induced roughness is not reduced by using multiple exposures. In fact, the data suggests that multiple exposures may even increase R_a for the films used in our study (compare Figs 4.1 and4.5b). Toet et al also reported that laser induced roughness increases with film thickness, since thicker films contain larger grains. For the films in our study however, this trend is not observed. Figure 4.6 shows R_a for a-Si:H films grown to different thicknesses and then irradiated using a single pulse with an E_D of approximately 65 mJ/cm^2. With the exception of a few variations, the roughness is in the ~15 nm range for all thicknesses explored. The differences observed here can probably be attributed to differences in laser fluences and initial film thickness. In the smoothing procedure reported by Toet et al, thin a-Si:H films (≤ 90 nm) were irradiated with multiple pulses at energy fluences sufficient to melt the entire film. The smoothing effect was explained by progressive separation of defects with additional pulses, where it is assumed that these defects act as heterogeneous nucleation centers for grain growth, leading to roughness. The authors also noted that above a certain number of shots, the roughness does not decrease significantly, and in some cases, may even increase due to substrate damage. The a-Si:H films in our study are much thicker (≥ 300 nm) and even the highest laser fluences used do not result in full melting/crystallization. The data in Fig 4.5 and 4.6 suggests then, that

a)

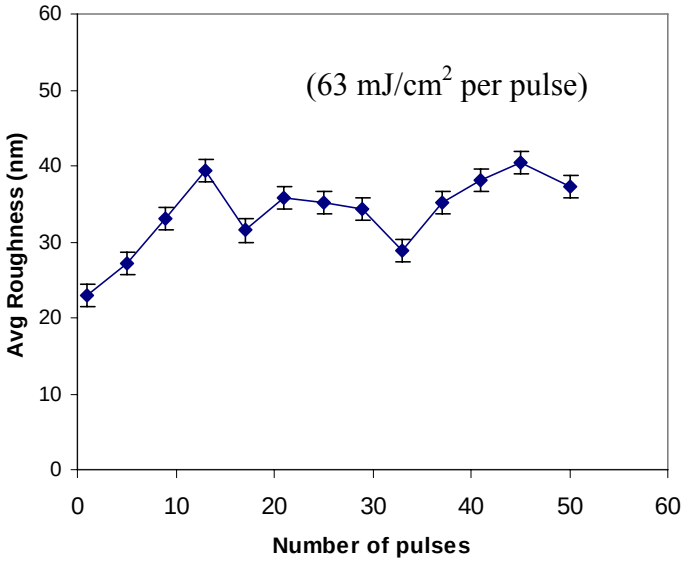

b)

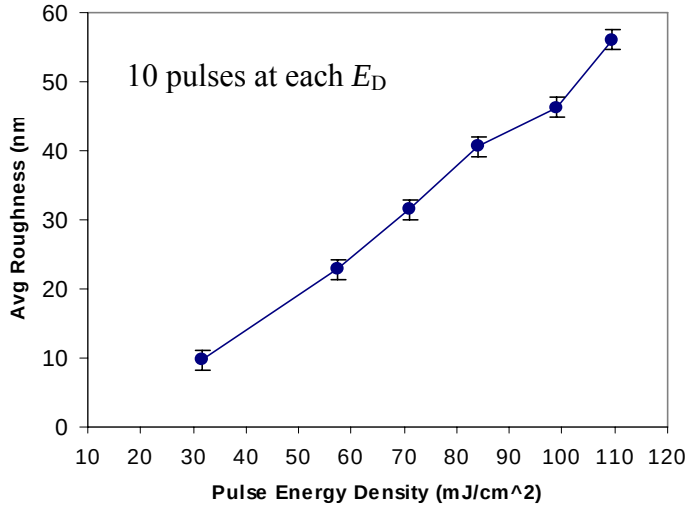

Figure 4.5: Roughness plotted vs. the number of pulses for a constant energy density of ~63 mJ/cm^2 (a), and as a function of energy density (b), where the number of shots fired at each E_D is fixed at 10.

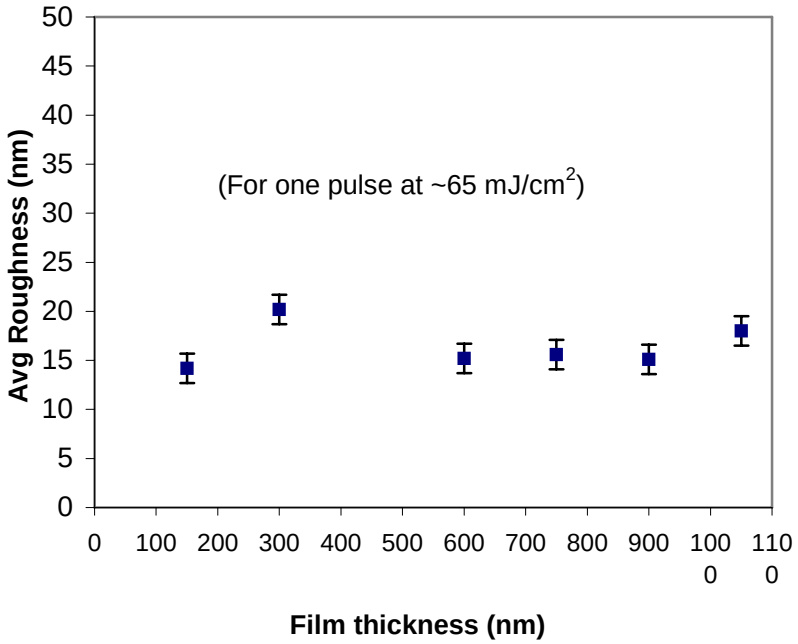

Figure 4.6: Average Roughness for a-Si:H films grown to different thicknesses and then irradiated using a single pulse with an E_D of approximately 65 mJ/cm^2

the film/substrate interface may be responsible for achieving reduced roughness using the smoothing technique by Toet et al. That is, since the entire film is melted upon irradiation, the substrate may act as a template for subsequent crystallization. Full melting/crystallization of the a-Si:H films in our study was not a viable option, as this would risk damage to underlying HgCdTe/CdTe films, which are to be used as active device layers. A more useful smoothing technique involving multiple laser pulses is discussed below.

4.4 Step-wise crystallization

We have also experimented with a step-wise laser irradiation approach that uses multiple laser pulses with progressive increases in the pulse energy density. This technique has been used by others to suppress explosive H evolution during crystallization, and it is attempted here to lower R_a. One study [84] reported success using multiple pulses at three successive pulse energies of 100, 140 and 330 mJ/cm^2. Another study [96] used only single pulses at 150, 300, and 374 mJ/cm^2. In this work, much lower fluences were used, since E_{th} = 30 mJ/cm^2 for the films in our study. Figure 4.7 plots the average roughness for step-wise laser irradiation sequences using different energy density increments. Each sequence started with a pulse well under E_{th} and then ended with a final pulse of approximately 65 mJ/cm^2. The total number of pulses fired is also indicated next to each data point. The roughness values suggest explosive crystallization occurred for all but the last sequence in which 11 pulses were fired with increments of approximately 5 mJ/cm^2. For this sequence, a roughness of 1.1 nm was achieved which is well within the range typically observed for as deposited a-Si:H. Thus the R_a value measured for this sequence is very promising.

There is however, another complication that arises due to the use of multiple pulses in general. Figure 4.8 shows optical micrographs and profilometer scans for patterns generated using a single pulse (a), and step-wise crystallization (b). In (a), the pattern appears dark due to the high roughness (R_a =14.7 nm), which is associated with granular surface texture. In b) the bright patterns are indicative of specular reflection off a smooth surface, which is confirmed by the profilometer scan across a

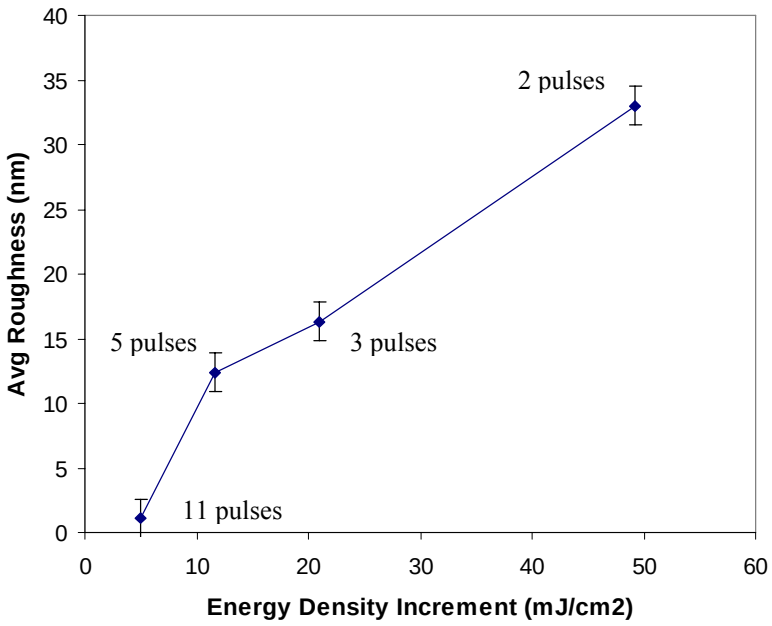

Figure 4.7: Average roughness vs. energy density increment using step-wise laser irradiation. Each point represents a sequence of pulses where the first pulse is < E_{th} and the last pulse is approximately ~65 mJ/cm^2. For example, the 3 pulse sequence: 24, 46, and 66 mJ/cm^2.

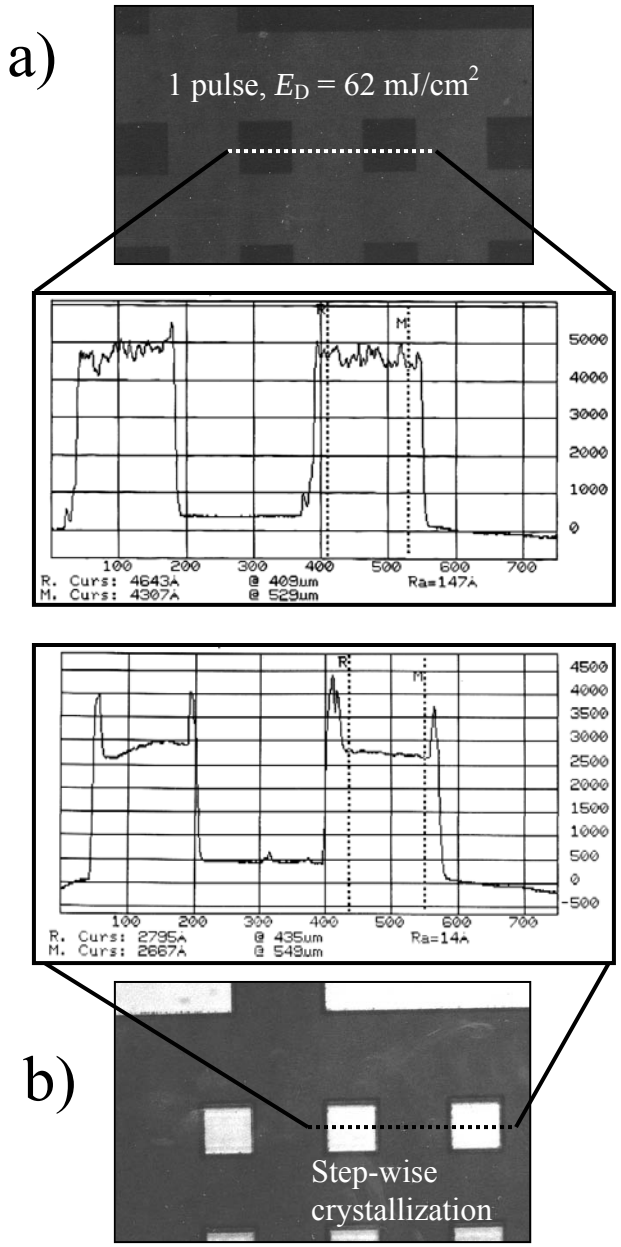

Figure 4.8: Optical micrographs and profilometer scans for patterns generated using a single pulse at high E_D = 62 mJ/cm^2 (a), and using the step-wise crystallization procedure (b). Average roughness values for the indicated regions were 14.7 nm and 1.4 nm respectively. (Horizontal and vertical axes are in microns and angstroms, respectively).

~ 100 μm area. The edges of the pattern however, appear to be roughened. This effect may be due to a spatial coherence phenomenon that is inherent to all laser projection systems. In essence the intensity distribution in the image plane of a sharp edge shows a "ringing effect", where the position of the edge appears to shift towards the center [97]. The effect may not be noticeable in an image created using a single pulse. However, when multiple pulses are used, the effect may become more and more apparent. In addition, vibration of the sample at the exposure position assures that patterns generated by multiple exposures will not be exactly aligned, making roughness at pattern edges difficult to avoid. As we will see in the next chapter however, the edge roughness effect caused by step-wise crystallization may be a limitation only for smaller pixel (mesa) arrays. In addition, it is likely that the effect would be much less pronounced in a properly designed laser-projection system (i.e., with minimized sample vibration).

To better understand the effects of step-wise crystallization, IR absorption studies were carried out for irradiated samples. Table 4.1 lists the different pulse sequences used for generation of 7 patterns (see Figure 4.9) during a step-wise crystallization experiment. Using a ~5 mJ/cm^2 increment in E_D, six patterns (2 through 7) were generated. Each pattern was irradiated with an increasing # of pulses and progressively increasing energy densities. It should be noted here that the 5 mJ/cm^2 increment is only an approximate value, and that variation occurs due to our inability to precisely control the excimer laser output energy. For reference, another pattern (#1) was generated using only a single pulse of 60 mJ/cm^2. FTIR analysis of the as-exposed patterns was carried out immediately after removal from the vacuum

Pattern #	Pulse Sequence (mJ/cm^2)
1)	60
2)	5, 10, 15
3)	5, 10, 15, 20, 25, 30
4)	5, 10, 15, 20, 25, 30, 35, 40
5)	5, 10, 15, 20, 25, 30, 35, 40, 45, 50
6)	5, 10, 15, 20, 25, 30, 35, 40, 45, 50, 55
7)	5, 10, 15, 20, 25, 30, 35, 40, 45, 50, 55, 60

Table 4.1: Pulse sequences used for 7 patterns during step-wise crystallization experiment. See Figure 4.9 below. Note the 5 mJ/cm^2 increment in E_D, (for patterns 2 through 7) is only an approximate value.

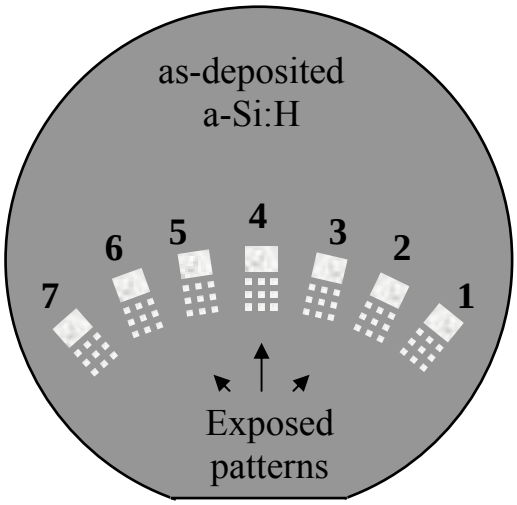

Figure 4.9: Schematic illustration of experiment to investigate a-Si:H film at different points during the step-wise crystallization sequence (see table 4.1). The experimental setup allows 7 distinct patterns to be generated on a single 3" wafer.

system. Figure 4.10 shows integrated intensities for the spectral region corresponding to Si-H stretching modes (~wavenumbers 2150-1900 cm^{-1}) in the IR absorption spectra. The plot shows data for each pattern (solid squares on solid lines) and for regions between each pattern (empty squares on dotted lines). The IR spectra

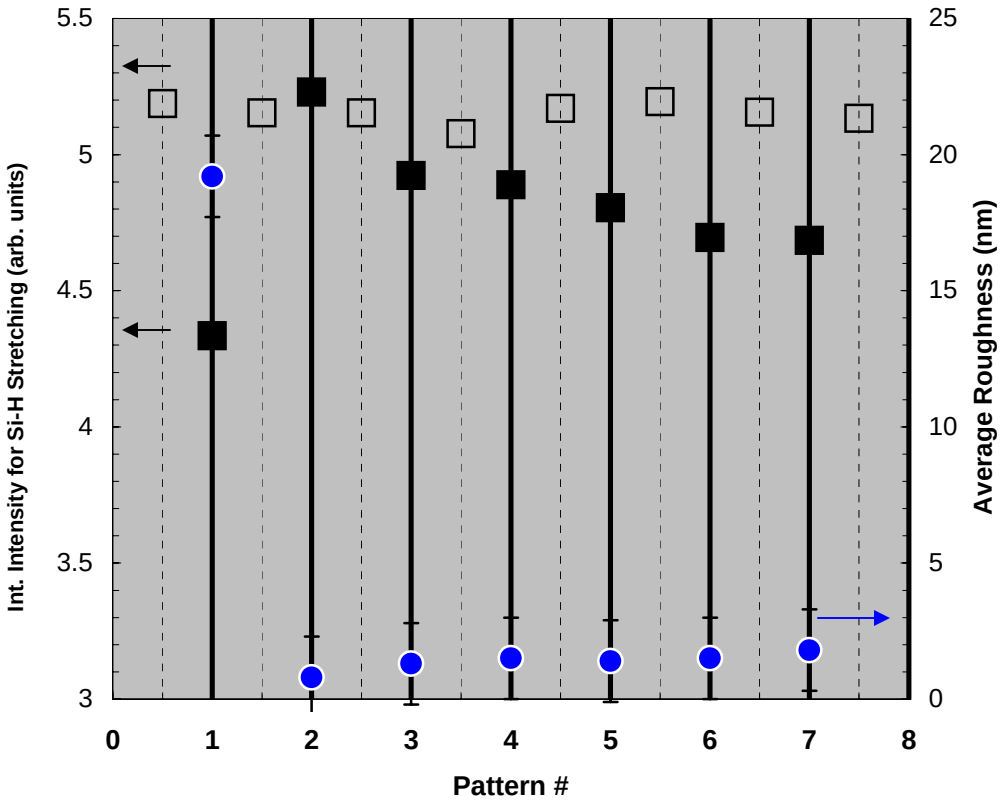

Figure 4.10: Integrated Intensity for Si-H stretching modes in IR absorption spectra obtained for the patterns indicated in figure 4.9. Square data points on solid grid lines represent absorption from a region within the specified pattern. Square data points on dotted grid lines represent absorption data from as-deposited a-Si:H regions between each adjacent pattern. The right y axis shows the average roughness (solid circles), measured via profilometry across a ~100 μm region of each pattern. See Figure 4.9 for a description of the laser treatment used for each pattern.

between each pattern were recorded only to determine if observed trends could be due to non-uniformity across the sample. The relatively minor changes in absorption intensity across the wafer for as-deposited regions (empty squares) suggest that this was not the case. However, there is a definite trend observed for patterns 2 through 7. The decreasing absorption intensities are indicative of decreasing H content (as explained in chapter 3.4). This trend confirms the working theory behind the step-wise laser crystallization procedure in that, explosive dehydrogenation is avoided by using incremental increases in energy density to slowly evolve hydrogen from the surface during the crystallization process. It is also interesting to note that the absorption intensity for pattern #1, (created using a single high energy pulse), is lower than that for pattern #7. This suggests that changes to the a-Si:H surface during the step-wise crystallization procedure, prevent the total H evolution from reaching levels obtained by explosive crystallization. The average roughness measured for each pattern (solid circles on solid lines), is plotted on a secondary y axis in Figure 4.10. The low R_a values obtained for patterns (2 through 7), confirm explosive crystallization is avoided throughout the step-wise crystallization procedure.

An identical experimental procedure was carried out as that shown in Figure 4.9, with the exception that the patterns were H_2 development-etched to remove unexposed a-Si:H regions. Figure 4.11 shows the pattern thickness for patterns labeled 1 through 7. As in chapter 3, a 500 nm thick layer was originally deposited so that we expect a fully developed pattern to have this thickness. However, a thickness of 500 nm was measured only for pattern # 1, and patterns 6 and 7 fell short by at least 100 nm. While it is not yet clear what causes this result, it will be shown later

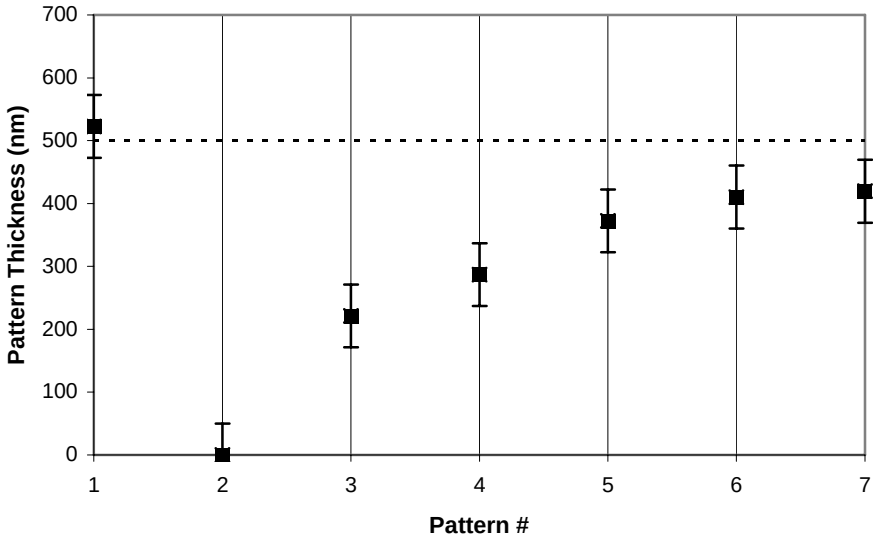

Figure 4.11: Pattern thickness after 90 min plasma development-etching for patterns generated using the pulse sequences described in Figure 4.9. The dashed line represents the nominal as-deposited resist thickness.

that patterns generated by step-wise crystallization are indeed sufficient for obtaining desired etch depths during pattern transfer to underlying device layers.

Cross-section TEM was also performed to examine the microstructure of a-Si:H films subjected to the step-wise crystallization technique. Figure 4.12 shows a bright field image for a ~500 nm film irradiated with a series of pulses similar to that used for pattern # 7 in Fig 4.9. Compared to the images previously shown in Figures 3.6 and 3.7, the profile of the laser induced poly-Si surface appears much smoother. In addition the grain size and grain size distribution are significantly smaller. For a better observation of grain morphology, a higher magnification image of the laser-induced poly-Si region is presented in Figure 4.13a. For comparison a second image (4.13b) is shown with the same magnification for a film irradiated with a single high

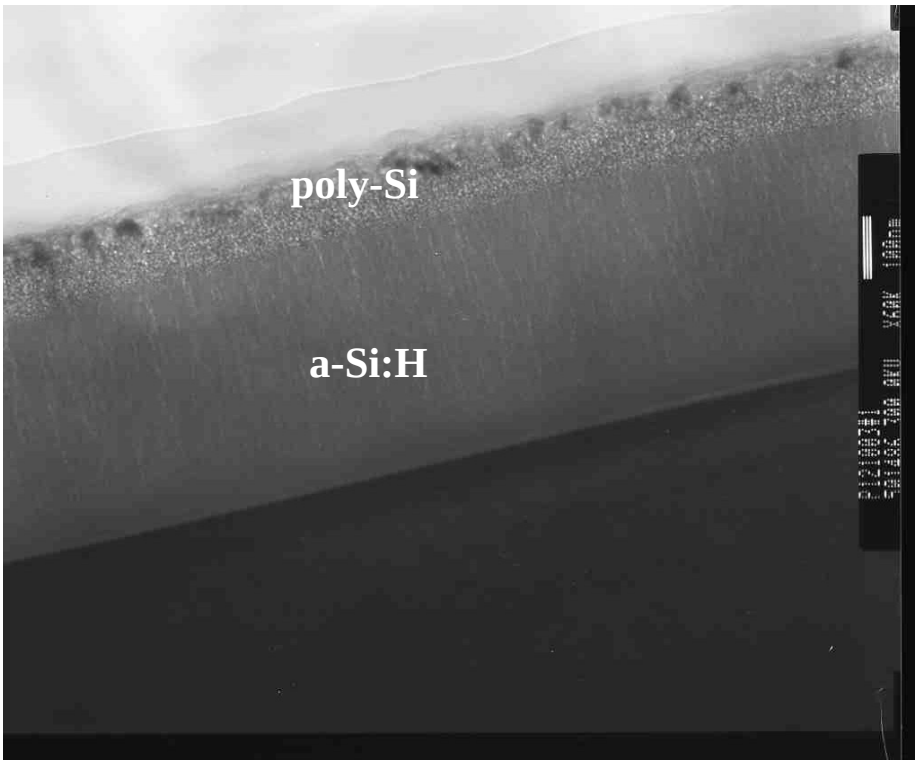

Figure 4.12: Cross-section TEM image for a ~500 nm a-Si:H film exposed using the step-wise crystallization procedure. The sequence of pulses used was similar to that used for pattern # 7 in Fig 4.9.

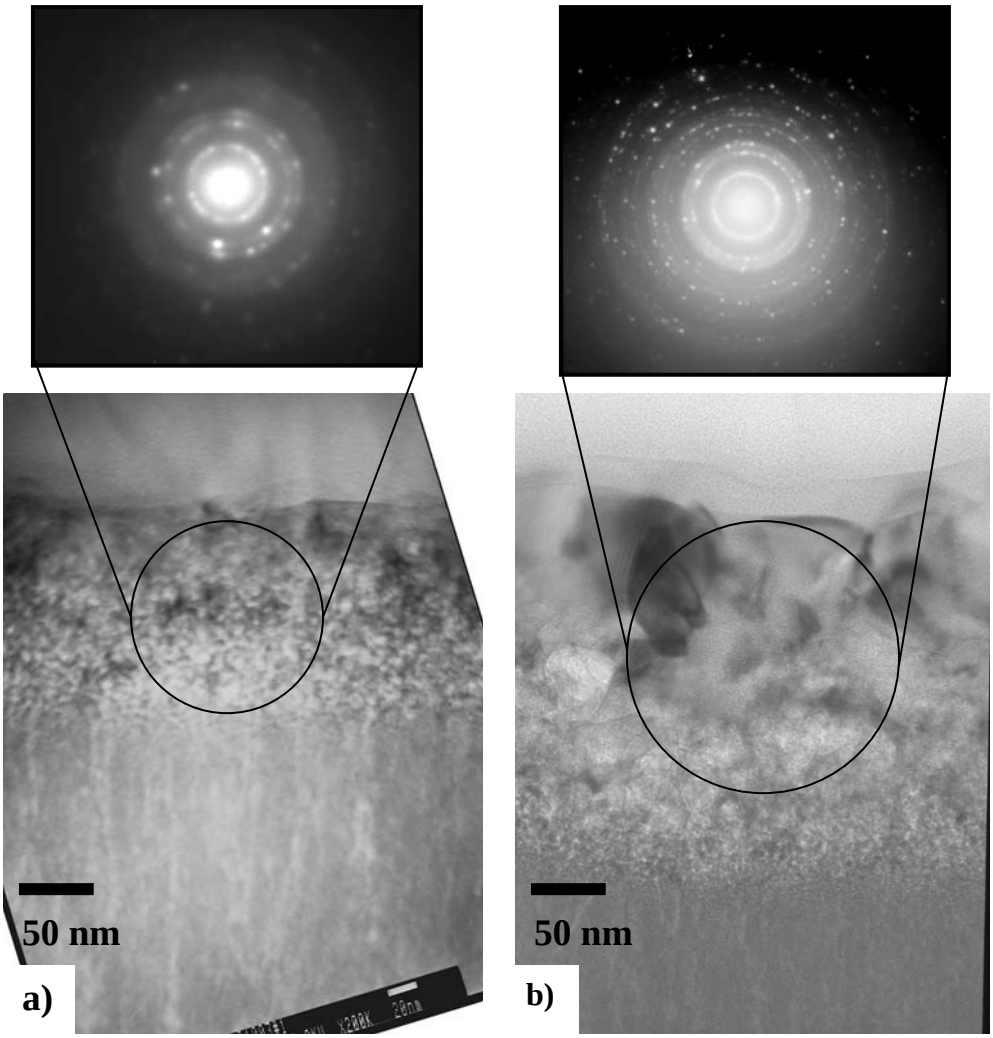

Figure 4.13: Higher magnification of poly-Si region in Fig. 4.12 where step-wise crystallization was used a). SAD pattern of specified region is also shown. For comparison, the near surface region of a film irradiated using a single high energy pulse is shown in b), along with the corresponding SAD pattern.

E_D pulse. Both films contain very small grains (< 5 nm) close to the a-Si:H, poly-Si interface. At the surface however, the grain sizes observed in 4.13b are up to ~100 nm or higher. In contrast, step-wise irradiation produced grains no more than ~30 nm at the surface (a). The difference in grain size is also reflected in the SAD patterns shown for the poly-Si regions. The SAD patterns show sharper rings for the sample

exposed to one high E_D pulse (indicating larger grains), compared to the more diffuse rings (and less diffraction spots) observed for the step-wise crystallization sample.

4.5 Discussion of effects of various laser treatments

To understand the different morphologies that result from different laser treatments, it is useful to take a more detailed look at the laser-induced phase changes occurring at the surface. Cerny et al, provide a theoretical model for laser crystallization of a-Si that is consistent with the different microstructures and experimental results observed in this thesis [98]. At a single pulse above E_{th}, the absorbed radiation first heats the material until the temperature is high enough to melt a thin layer near the surface. As this molten layer begins to solidify as poly-Si, a latent heat of crystallization L_{pc}, is released. However L_{pc} is larger than the latent heat of melting of a-Si $L_{m,a}$, and therefore the underlying a-Si material begins to melt. This new molten layer is extremely undercooled compared to the poly-Si (on top), so that it resolidifies as fine grained poly-Si. These phase transitions essentially result in the propagation of a liquid-Si/poly-Si interface into the underlying a-Si material. Once the laser energy is completely absorbed, further propagation of the interface takes place only due to the release of latent energy (L_{pc} - $L_{m,a}$). Thus a fine grained poly-Si layer will exist at the final position of the interface, with large grained material on top [84,98].

Fine grained poly-Si material is visible in TEM cross-sectional images (Figures 3.6, 3.7 and 4.13). For samples irradiated using a step-wise crystallization sequence, (Fig 4.12 and 4.13a), a much smaller ratio of large-grain to fine-grain

material exists. In addition, the total thickness of the poly-Si regions is generally larger for samples irradiated with only a single pulse at $E_D > E_{th}$. These differences can only be explained by the fact that the thermal properties of the a-Si:H surface change with each successive pulse during a step-wise crystallization sequence. At energies just above E_{th}, a thin molten layer forms, but grain growth is not extensive since the surface temperature and melt duration is relatively low. In addition, since the laser energy is quickly absorbed, only minimal propagation of the *l*-Si/poly-Si interface (due to L_{pc} - $L_{m,a}$) will occur, so that the fine-grained poly-Si region will exist just below the initial surface position. With each successive laser pulse, the maximum position of the interface is pushed farther into the film as the fine-grained region melts and resolidifies. However the material above this fine-grained interface does not have sufficient energy to grow into large grains (as in Figure 4.13b), due to a change in thermal properties of the surface. Namely, we may infer that the thermal conductivity is higher in poly-Si relative to a-Si, as a natural consequence of more ordering and less phonon scattering [98]. Thus, the heat absorbed in the upper region is more quickly dissipated, and the shorter melt duration does not allow for extensive grain growth. At the end of the step-wise sequence, the upper grains are still larger than the underlying fine-grained material, but never grow as large as that observed for a single high E_D density pulse.

We speculate that the low R_a values observed using step-wise crystallization, are due to a combination of slow grain growth (as described above), in addition to a slow rate of H out-diffusion. Previously, Toet et al reported excimer laser-induced roughness of approximately 7 nm for PVD grown a-Si (i.e., ~0 at% H) [92].

However roughness values as low as 1.1 nm have been achieved in this thesis for a-Si:H. Thus, rapid H out-diffusion is not solely to blame for laser-induced surface roughness. For films with nonzero H concentrations, explosive H out-diffusion will lead to increased roughness. Our results show that by substantially reducing the energy density increment in the pulse sequence, the roughness can be reduced such that ($R_a^{\text{exposed}} \approx R_a^{\text{as-deposited}}$). It appears the energy density increment necessary to avoid explosive H evolution decreases as the initial H content of the film is increased. For the low deposition temperatures used in our study (~ 50 ºC), a concentration of up to (40 at %) is expected, compared to (5 at%) for 250 ºC, which is a typical-a-Si:H deposition temperature, used in the TFT industry [99].

4.6 Conclusions

We explored different techniques to reduce roughness in excimer laser irradiated a-Si:H surfaces for use in a dry lithography process. A direct dependence of roughness on the single pulse energy density was demonstrated and explained by the fact that smaller grains will result from lower energy densities. Reducing the single pulse E_D alone however, does not reduce R_a to acceptable levels. In contrast to other studies, multiple exposures at a fixed energy density do not reduce R_a for the films in this study. Among other differences, the initial thickness of the a-Si:H films in those studies is significantly less and full melting of the film occurs upon laser irradiation. Therefore, smoothing techniques reported elsewhere either cannot be used, or must be modified for the films in our study.

The step-wise laser crystallization technique proved to be the most promising as R_a values as low as 1.1 nm were achieved. These roughness values satisfy the requirement, $R_a^{\text{exposed}} \approx R_a^{\text{as-deposited}}$. Here, a step-wise crystallization sequence using a pulse energy density increment of ~5 mJ/cm^2 was required to produce sufficiently low R_a values. This is compared to an increment of up to ~150 mJ/cm^2 used elsewhere [84,96]. IR absorption was used to indirectly monitor the H evolution during the crystallization sequence, and TEM images were obtained to image the resulting near surface morphology. Our data suggests that the observed reduction in roughness is due to smaller crystallites in addition to a slow rate of H evolution. We conclude then, that the energy density increment required to avoid explosive crystallization of a-Si:H films has a strong dependence on the initial H content. Due to our experimental set up, it is difficult to accurately determine whether the edge roughening (seen in exposed patterns), is caused solely by vibration of the sample holder or if it is also due to spatial coherence effects described in section 4.4. However it will be shown in the next chapter, that this edge roughness is drastically reduced after the Mesa-etch (pattern transfer) step.

Chapter 5

Pattern Transfer via ECR plasma etching

5.1 Introduction

The reticulation of planar thin films is a fundamental processing step for fabrication of various microelectronic devices. In our particular study, reticulation or "mesa-etching" is required to define and isolate mesas for use in infrared-imaging focal plane arrays. To carry out this crucial step, a lithographically defined pattern is "transferred" to underlying active device layers.

For pattern transfer, the advantages of dry plasma-etching over conventional bromine-based wet-etching have recently been recognized [100]. NVESD uses a procedure based on Ar/H_2 gas chemistries within an electron cyclotron resonance (ECR) etching system. The particular gas chemistry used here aids in overcoming complications with ternary alloys such as HgCdTe [26,101,102]. The ECR reactor allows for highly anisotropic etching, which is required for state of the art detector structures. For example, it is estimated that a 20 μm pitch, two-color, triple layer structure will require an etch depth of 15 μm with a trench spacing of 5 μm [103].

Thus far, ECR etching studies at NVESD have focused primarily on conventional resists. Etch selectivity, plasma parameters, resist type and the effects of initial feature geometries have been studied in great detail. While certain questions still remain (particularly in the area of plasma induced damage and etch loading effects [104]), a wealth of knowledge has been gained through these studies. Etch

depths exceeding 15 μm (with 3 μm trench spacing) have been achieved through the development of advanced hardened resists in combination with optimized plasma parameters [105]. In essence, this work demonstrated the usefulness of ECR plasma processing for next-generation HgCdTe focal plane arrays.

Very little work has been performed on ECR etching using a-Si:H dry resists. This chapter presents some initial attempts to address the most fundamental aspects of the pattern transfer process including, etch selectivity and plasma-induced roughness. Patterns are etched into underlying CdTe and HgCdTe films, and the resulting profiles are examined using various techniques. Issues affecting faithful pattern transfer such as "etch bias" are discussed and compared to ECR etching using conventional organic resists. We also investigate a separate plasma-etch procedure to selectively remove residual a-Si:H from mesa surfaces after desired etch depths have been achieved. If successful, this procedure would eliminate the need to reduce laser-induced roughness at the mesa surfaces. Unresolved issues discussed in this chapter reflect the fact that more experimental work is needed to better understand various aspects of ECR pattern transfer using a-Si:H resists.

5.2 Experimental Procedure

a-Si:H films were deposited via PECVD to thicknesses up to 1200 nm. Other deposition parameters were fixed at 3 W rf power, 50 °C substrate temperature, and an overall pressure of 500 mTorr. The SiH_4 gas concentration was fixed at 6.5% in argon (the standard for deposition throughout most of this thesis). The a-Si:H resists were grown on epitaxial layers of either CdTe or HgCdTe/CdTe on Si(211)

substrates. MBE growth of these films on Si(211) substrates was discussed in section 2.1 and more details can be found in the literature [16-18,41-44].

Excimer laser irradiation was carried out in vacuum at 10^{-7} Torr after deposition of the a-Si:H layer. Patterns were generated using a single pulse with energy density above the crystallization threshold E_{th}, while others were created using the step-wise crystallization procedure (see section 4.4). The patterns were developed in the PECVD chamber, using the standard H_2 plasma etch parameters described in the previous chapters. In-situ thickness monitoring via He-Ne laser interferometry was essential to ensure complete removal of unirradiated a-Si:H prior to further processing.

After full resist development samples were mesa-etched in the ECR reactor using process parameters adopted for etching CdTe or HgCdTe films through conventional organic resists. Flow rates of 80 sccm argon and 20 sccm hydrogen were used to establish a 4:1 argon to hydrogen ratio, with an overall process pressure of 2 mTorr. Other ECR process parameters for CdTe/HgCdTe etching include an input microwave power of 300 W, and an rf power (to the substrate) of 120 W. The input rf power produces a DC-bias potential which influences the contribution of Ar+ bombardment to the etch process [105].

The chemical species at the near surface of the etched samples were examined using Auger electron spectroscopy (AES). The samples were examined via profilometry and imaged using a scanning electron microscope (SEM) with an attachment for energy dispersive x-ray analysis (EDX). In addition, cross-sectional TEM was used to examine the microstructure of a-Si:H resists subjected to ECR

plasma etching. AES was carried out on a Phi 5802 Scanning Auger system operated at 5 KeV and SEM/EDX analysis was performed using a CamScan Maxim 2040SL operated at 40 KeV. Cross-sectional TEM samples were prepared as mentioned in section 2.6.2.2, with the exception that lower ion-milling voltage (2-3 KV), lower beam current (1 mA), and a smaller beam angle (9°) were used to minimize damage to the II-VI epilayers. TEM analysis was carried out on a JEOL 4000-FX operated at 300 KV. It should be noted that due to the type of experiments carried out in this chapter, totally in-vacuum processing and analysis were not performed. Thus the effects of oxidation and contamination should be considered during the analysis of etch profiles.

5.3 Pattern Transfer and Etch Selectivity

5.3.1 Mesa etching in CdTe films

Our first series of experiments was aimed at determining ECR etch selectivity between a-Si:H resists and CdTe, and also to demonstrate faithful pattern transfer. A 300 nm thick a-Si:H film was deposited on a CdTe/Si(211) wafer and several patterns were generated using single pulses at approximately 50 mJ/cm^2. After H plasma development, the sample was cleaved so that each pattern was separated onto single pieces. The cleaved pieces were each etched in the ECR for selected times. Figure 5.1 shows the CdTe etch depth (step height), and a-Si:H resist thickness vs. ECR etch time as estimated from SEM images. The simulated lines represent the expected CdTe depth and resist thickness based on known etch rates. The CdTe etch depth

increased linearly to approximately 2.5 μm for patterns etched up to 4 min and essentially remained constant for the pattern etched for 8 min. Conversely, the a-Si:H was completely removed after 4 min or less. The linear trend (for the first 4 min), implies similar ECR etch rates for a-Si:H and the laser-induced poly-Si top layer. In other experiments, ECR etch rates of 0.07 and 0.05 μm/min were measured for c-Si and a-Si:H resists, respectively. Thus, the etch rate for the poly-Si top layer is probably very similar or slightly higher than that for a-Si:H. In addition, the slope of

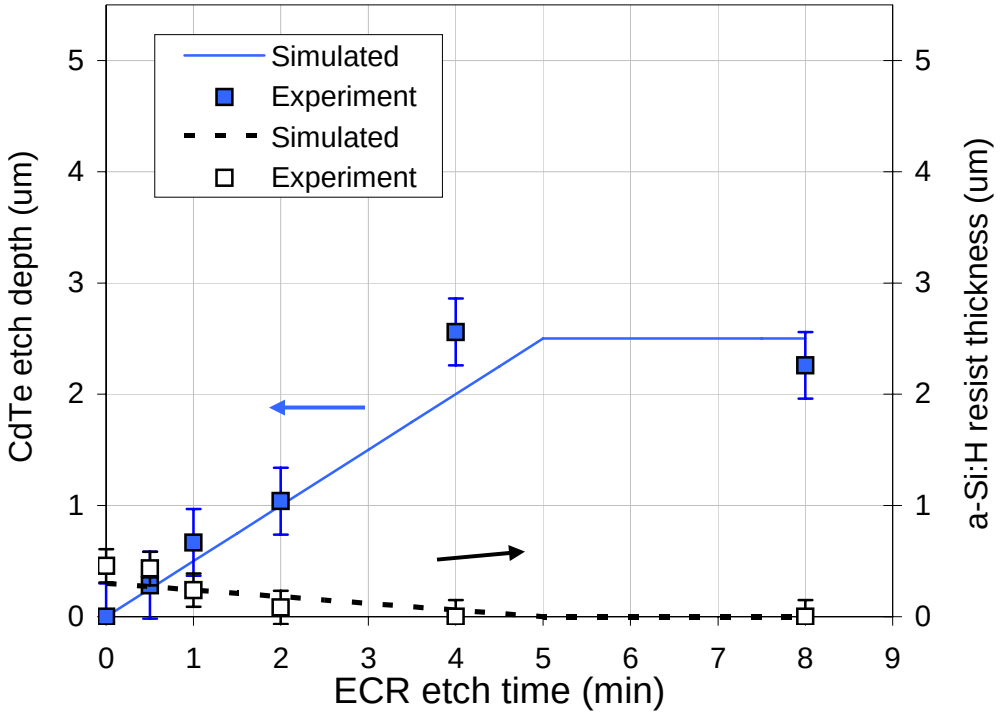

Figure 5.1: CdTe etch depth (step height) and a-Si:H resist thickness vs. ECR etch time. The lines represent simulated depths and thicknesses expected based on known erosion rates. The patterns were originally generated using a single 50 mJ/cm^2 laser pulse. Note that each data point represents a different pattern etched for a selected duration.

the line for the experimental data, shows a CdTe etch rate (~0.5 μm/min) which is similar to that previously determined [24]. Therefore, the etch selectivity between CdTe and a-Si:H is nominally 8:1.

To confirm the point at which complete resist removal occurred for samples in Fig 5.1, Auger analysis was performed. Figure 5.2 shows AES spectra from mesa regions of samples ECR etched for a) 0 min, and b) 4 min. A strong Si peak (~75-90 eV) is observed in a), indicating the presence of the resist. Oxygen and Carbon peaks are also present, suggesting that oxidation and contamination occurred upon exposure to air. This spectrum was essentially the same as that observed for samples ECR etched for 0.5, 1 and 2 min. In b), Cd and Te peaks appear while the Si peak is no longer present. A similar spectrum was obtained for the sample etched for 8 min. This data confirms that full removal of the ~300 nm thick a-Si:H resist probably occurs at just under 4 min ECR plasma etching. While C contamination can occur upon exposure to air, the reason for a stronger C peak in Figure 5.2b (compared to 5.2a) is not understood. However, a clear dependence of C contamination on ECR etch time was not observed.

Experiments were also performed to evaluate the extent to which laser-induced roughness at patterned surfaces is transferred to the underlying film after ECR etching. a-Si:H resists were grown to 450 nm, and irradiated using a single pulse of E_D = 65 mJ/cm^2 (pattern A), and also using the step-wise crystallization procedure discussed in section 4.4, (pattern B). The patterns were developed in the PECVD chamber and the resulting resist masks were etched in the ECR reactor for 7

a)

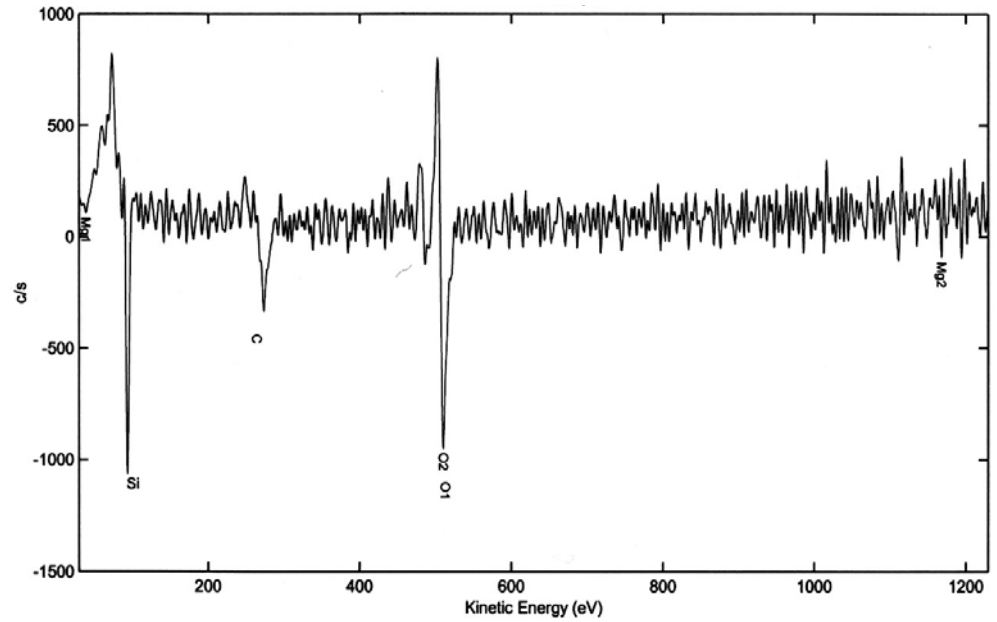

b)

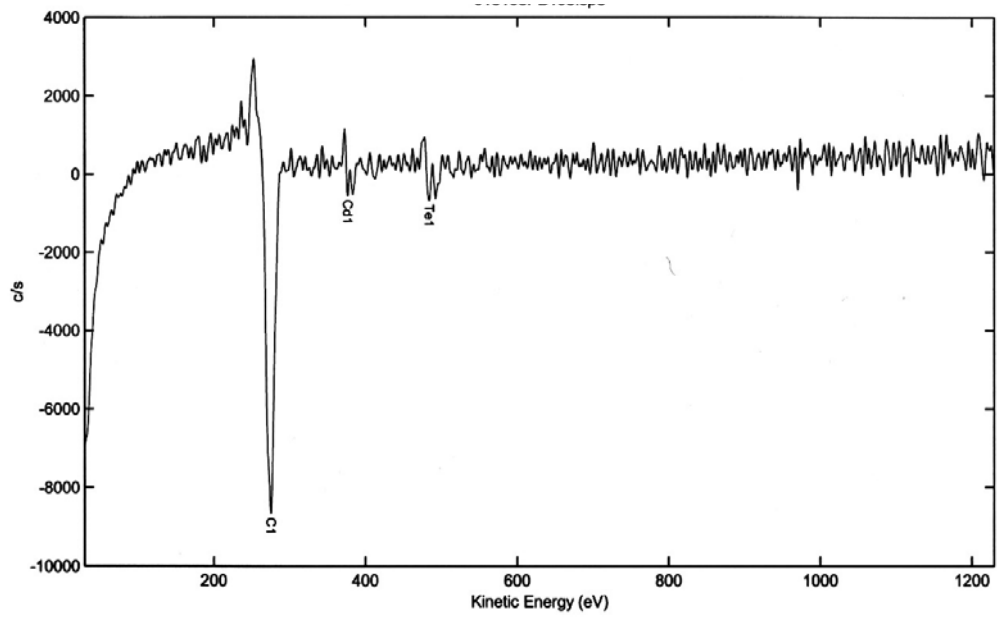

Figure 5.2: AES spectra from mesa surfaces of patterns from figure 5.1. Spectra shown for samples ECR etched for a) 0 min, and b) 4 min.

min to insure full removal of the resist during pattern transfer to an underlying CdTe film. The results are summarized in Table 5.1 below:

	Pattern A	Pattern B	Trench
R_a (nm) [Developed]	11.4	3.0	1.4
R_a (nm) [ECR etched]	59.5	12.4	5.0
thickness (μm) [Developed]	0.58	0.447	
thickness (μm) [ECR etched]	2.83	3.257	

Table 5.1: Surface Roughness (R_a) for patterns; as-developed, and ECR etched for 7 min. Pattern thicknesses (ie. total depth) before and after etching are also shown. Pattern A was generated using a single 65 mJ/cm^2 laser pulse. Pattern B was generated using step-wise crystallization. Typical roughness values from trench surfaces (CdTe) are also given.

ECR etching increased the roughness (R_a), for pattern A and B by a factor of approximately 5 and 4 times, respectively. For the Trench (i.e. unexposed regions), R_a increased from 1.4 to 5.0 nm after ECR etching. Thus, any pre-existing roughness in the as-developed patterns, or on the CdTe surface (trenches), is exacerbated during the ECR plasma etch. This is not surprising. Ar+ bombardment during etching leads to a highly anisotropic plasma process but also induces a certain level of physical damage. The combination of Ar+ bombardment and the more isotropic-like etching from atomic H, appears to suppress undesirable features in patterns generated via step-wise crystallization. Figure 5.3b shows the surface profile for a feature in pattern B (see table 5.1), after ECR etching. Note that the edge roughening typically observed for patterns generated using step-wise crystallization (see Fig 4.8) is no longer present. For comparison, Figure 5.3a shows the surface profile for the same feature in pattern A, which exhibits much higher R_a.

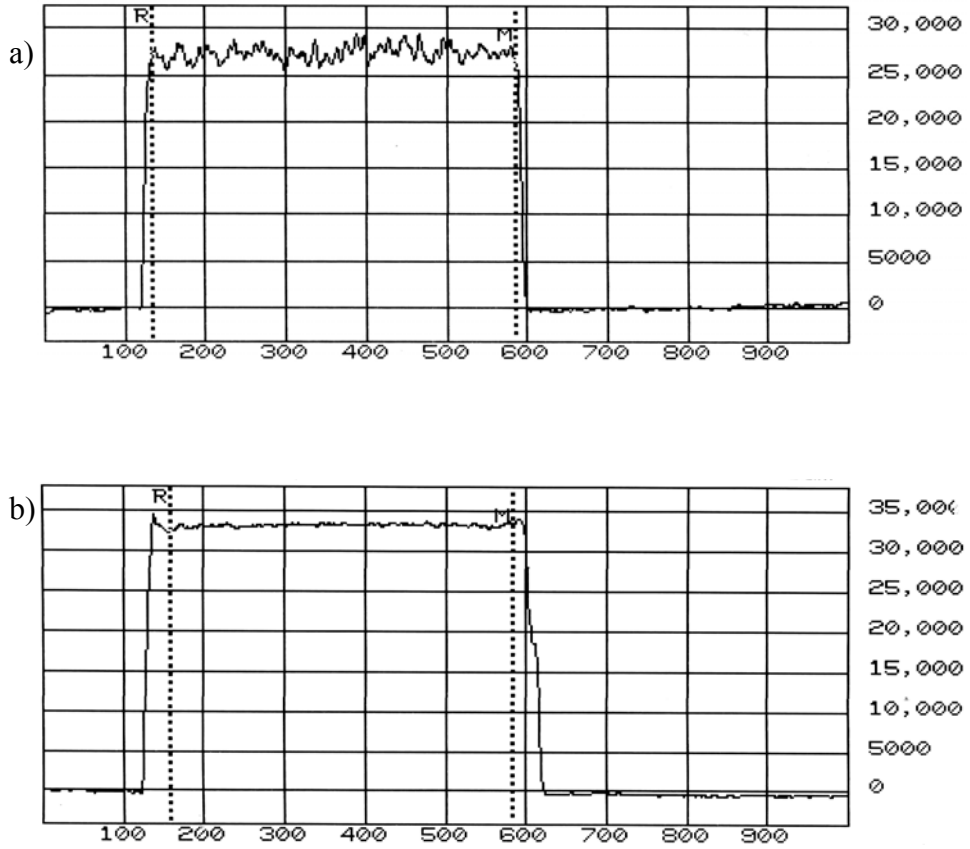

Figure 5.3: Surface profiles for identical features from a) pattern A, and from b) pattern B, after ECR etching into a CdTe epilayer. Units of the horizontal and vertical axes are in microns and angstroms, respectively. See table 5.1 for description of laser treatment used in patterns A and B .

Faithful pattern transfer is also affected by a phenomenon known as etch bias [61], which is schematically illustrated in Figure 5.4. The diagram shows that etch bias is caused by lateral erosion of the resist during pattern transfer. The effect acts to distort the final pattern after the etch process is completed. To investigate this effect, a nominal 1.2 μm thick a-Si:H resist layer was patterned, developed and then ECR etched for 7 min using typical processing parameters. The etch bias ($w_f - w_i$) as

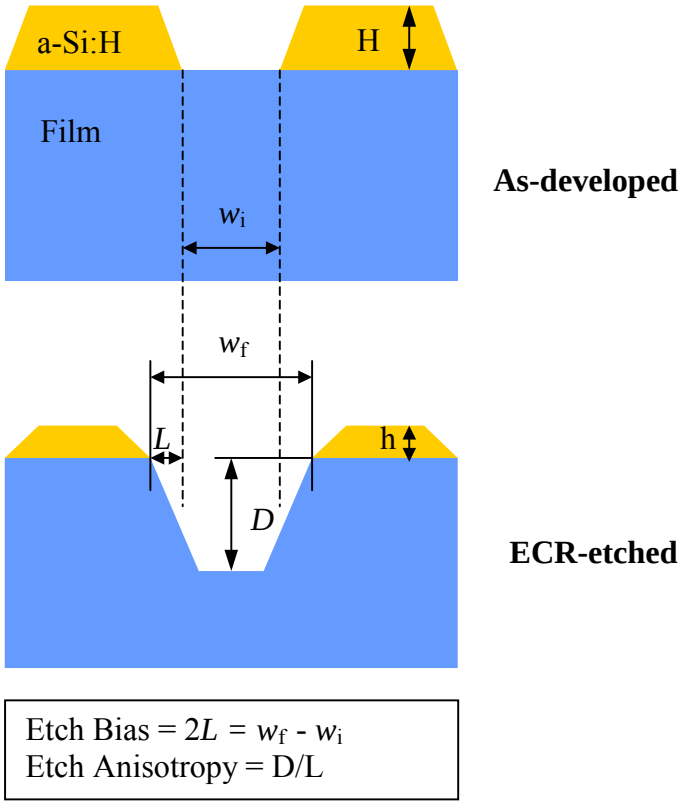

Figure 5.4: Schematic illustration of etch bias due to lateral resist erosion. The dashed lines represent the nominal position of the feature. The calculation for etch bias and etch anisotropy is also shown.

measured under an optical microscope, was estimated to be no more than 1 μm, for a ~4.5 μm deep trench. In fact, smaller values were measured by imaging the etched profiles via SEM, but it was not verified whether the samples were cleaved precisely enough to give accurate lateral measurements. On the other hand, SEM was useful for determining the degree of anisotropy and vertical resist erosion. Figure 5.5 shows SEM cross-section images of a feature after development (a) and after ECR etching (b). With an etch depth of 4.4 μm and an etch bias that is most likely < 1 μm, the

a.

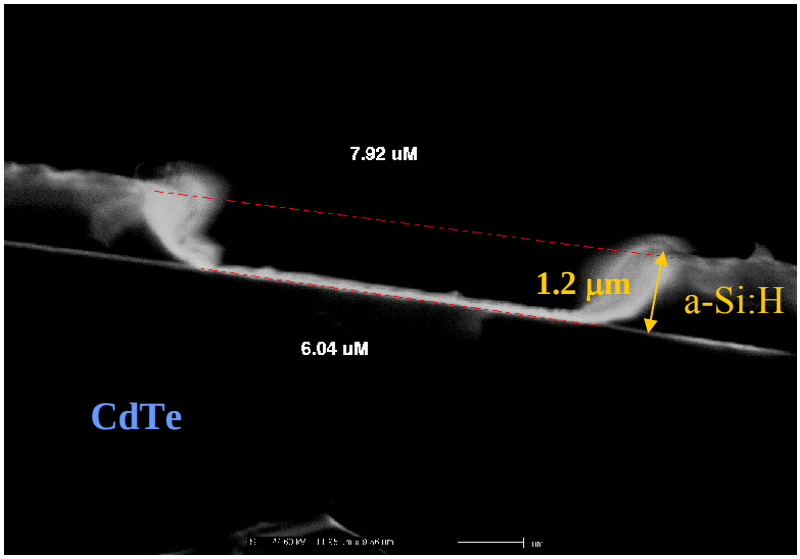

b.

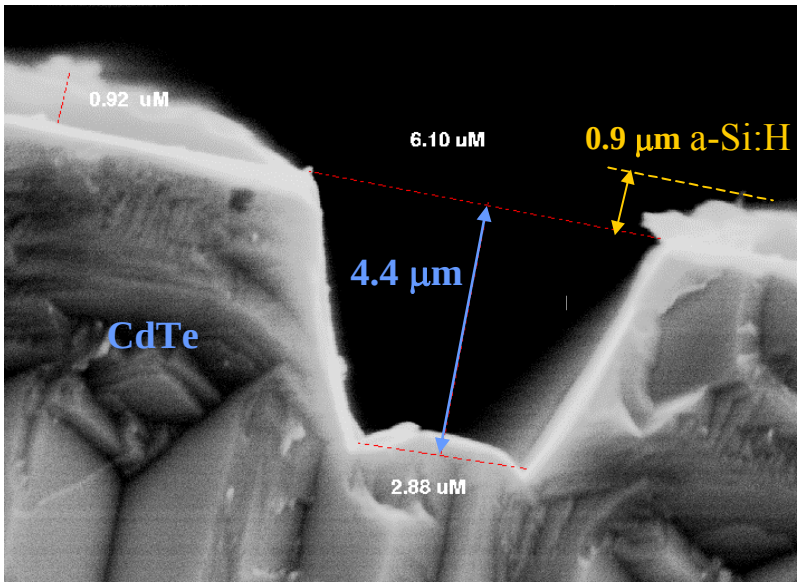

Figure 5.5: SEM cross-section images from as-developed patterns (a) and after ECR etching (b). Resist dimensions and CdTe etch depth are indicated. The trench width at the top of the CdTe Mesa was measured at 6.1 µm, but the accuracy of lateral dimensions could not be verified.

etch anisotropy (D/L) is at least 8.8. In comparison, for a 1.2 μm thick conventional organic resist, the etch bias and etch anisotropy are 3.4 μm and 0.94 respectively, for a 1.6 μm etch depth in CdTe [61]. For faithful pattern transfer and high aspect ratios, low etch bias and high etch anisotropy are desirable. Thus, the values obtained for a-Si:H resists, indicate a dramatic improvement over those measured for conventional organic resists.

The formation of rounded trench surfaces (Fig 5.5b) is observed for conventional resists and is well understood. This effect can be explained (see Figure 5.6 below), by considering the resist and film sidewall angles. First, due to an angular distribution of the incident plasma etchants, the etch rate will always be higher at resist feature edges. This means that even for feature edges that are initially

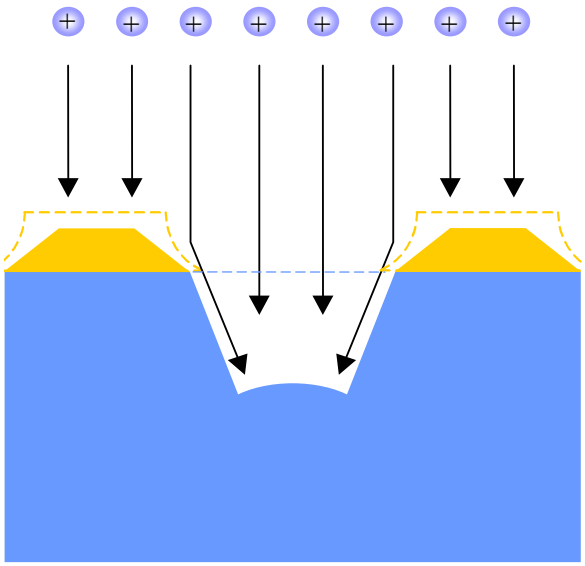

Figure 5.6: Schematic illustration of trench "bottom rounding" mechanism during ECR etching [61]. The initial resist sidewall angle plays a crucial role, deflecting impinging ions toward the corner of trenches. The dashed lines indicate the shape of the a-Si:H resist sidewalls prior to ECR etching, as is evident in Figure 5.5.

90º, resist sidewall angles eventually decrease during the etch process. The impinging plasma ions collide with the resist sidewalls and are deflected into the thin film. This causes a situation where the plasma ion density and hence the local etch rate is greater in the corners of the trench than in the center, and "bottom rounding" occurs. The a-Si:H resist sidewalls prior to ECR etching appear concave due to the isotropic nature of the plasma-development process (Figure 5.5a). The angle actually increases from 0 to 90° from the base of the resist wall, to the top. After ECR etching however, the resist wall appears convex, and the angle is no more than 20°. Note also that the CdTe sidewall angle is approximately 70°. Thus initial resist sidewall angles can influence the observed resist bias, in addition to causing trench-bottom rounding. These factors must be considered during the design of an etch process to achieve the correct feature sizes in the final product.

5.3.2 Mesa etching in HgCdTe films

Most of our mesa-etch experiments were initially performed using CdTe epilayers, since the intent was only to demonstrate pattern transfer and compare a-Si:H resist characteristics to conventional organic resists. Once fundamental aspects of the pattern transfer process were studied, mesa-etch experiments using the more complex HgCdTe films were to be the focus. So far, little work has been done on pattern transfer into HgCdTe films using a-Si:H resists. In our first experiment, a ~300 nm a-Si:H film was deposited on $Hg_{0.7}Cd_{0.3}Te$/CdTe/Si(211) and several patterns were generated using single pulses at approximately 43 mJ/cm^2. The low energy fluence was used here in attempts to achieve low R_a values. It should be

mentioned that this experiment was performed before the step-wise laser irradiation technique had been adopted for generating patterns. After pattern development, the sample was cleaved so each pattern could be ECR etched for different times (as in Figure 5.1). Figure 5.7 shows the HgCdTe etch depth and a-Si:H resist thickness at different etch times as estimated via SEM and profilometry. The data suggests that the a-Si:H is completely removed after 2 min ECR etching. This was confirmed by Auger spectra from the mesa surface, which showed Hg, Cd, and Te peaks, while a peak from Si was not present. Previous experiments have shown that HgCdTe etches twice as fast as CdTe under optimum ECR processing conditions [24]. Indeed, the slope of the line measured through the first two minutes is slightly over 1, compared to the initial slope in Figure 5.1, which is ~0.5. This confirms the factor of two difference in etch rate between HgCdTe and CdTe, and implies a 16:1 etch selectivity for HgCdTe and the a-Si:H resist. A very low etch depth was observed at 8 min (not shown) but was explained by the fact that the HgCdTe layer (originally ~ 5.5 μm thick) is completely removed, so that etching through the underlying CdTe layer had commenced. This was confirmed by Auger spectra, which revealed only Cd, and Te peaks. What remained unclear, is why an etch depth of only 2.5 μm was achieved. For the resist thickness used in this experiment, a HgCdTe etch depth of 4-5 μm was expected.

A likely reason for the discrepancy is non-uniformity of the initial a-Si:H resist pattern. Figure 5.8 below shows EDX spot analysis and line scans from mesa surfaces ECR etched for a) 0 and b) 1 min. The EDX line scans were obtained by recording x-ray photons from the Si-Kα, Hg-Mα, Cd-Lα, and Te-Lα transitions, as a

function of distance along the sample cross-section. Note the sharp Si signal disappears after only 1 min of ECR etching, suggesting the a-Si:H resist is completely removed. Unfortunately, the EDX data is further complicated by the possibility of overlapping signals. Namely, the Si-Kα (K-L_{II}) and Hg(M_{IV}-N_{III}) transitions generate

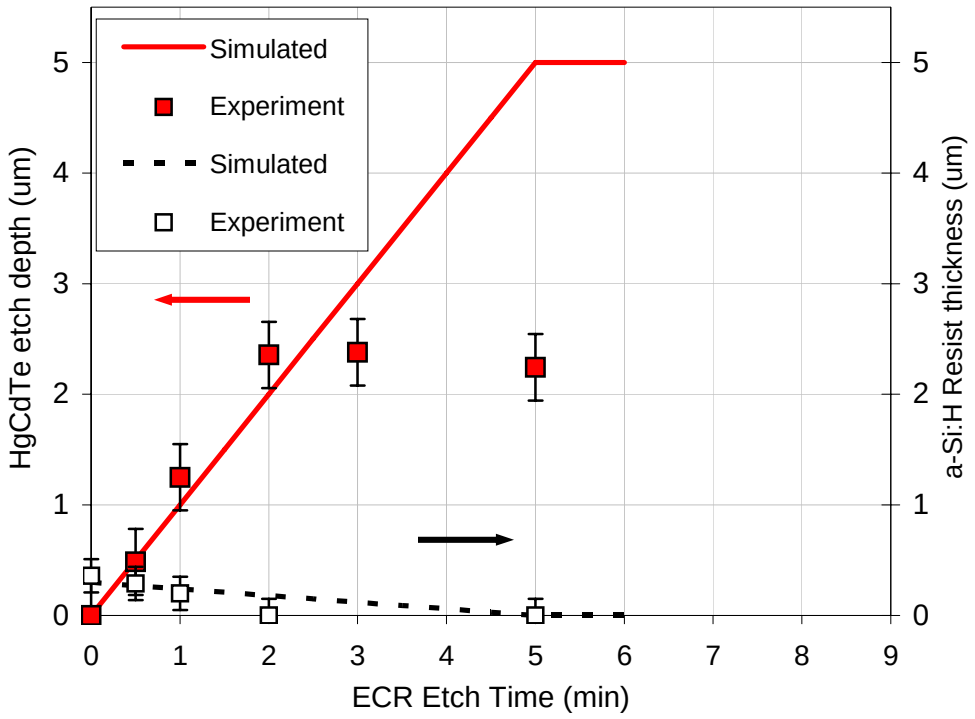

Figure 5.7: HgCdTe etch depth (step height) and a-Si:H resist thickness vs. ECR etch time. The lines represent simulated depths and thicknesses expected based on known erosion rates. The patterns were originally generated using a single 43 mJ/cm^2 laser pulse. Note that each data point represents a different pattern etched for a particular duration.

a) 0 min (spot analysis)

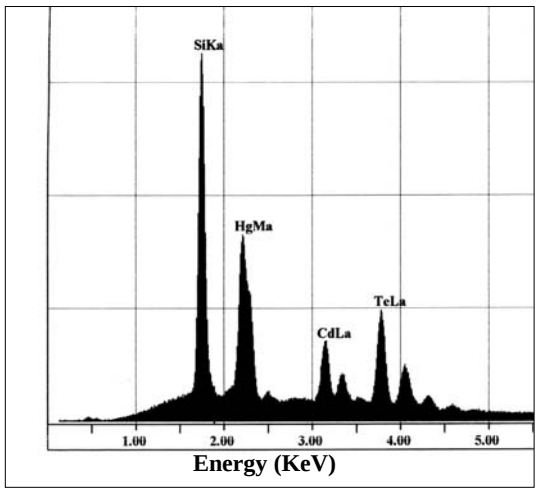

b) 1 min (spot analysis)

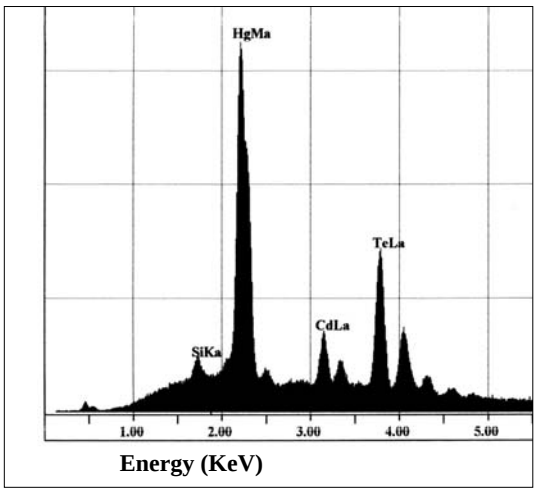

c) 0 min (line scan)

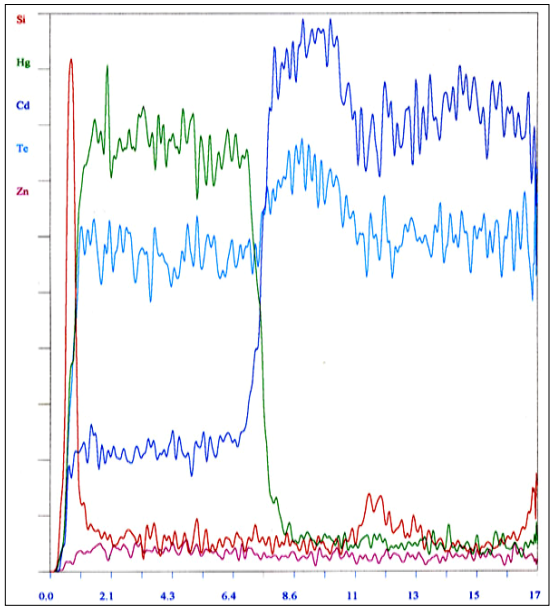

d) 1 min (line scan)

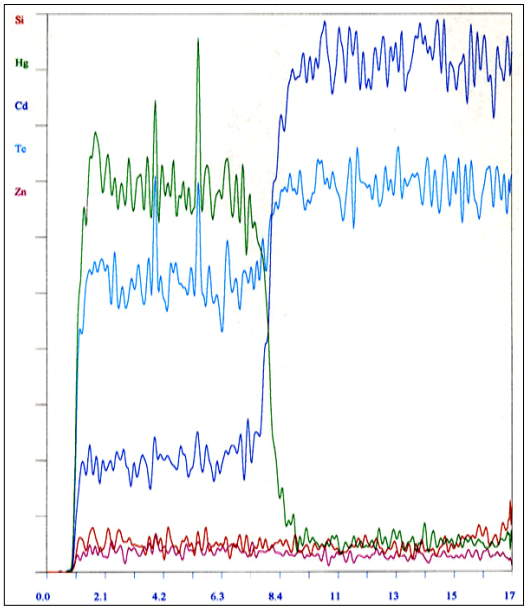

Figure 5.8: EDX spot analysis and line scans from mesa surfaces of patterns in fig 5.7. Data shown for samples ECR etched for a) 0 min (as-deposited), and b) 1 min. EDX line scans were obtained by recording x-ray photons from the Si-Ka, Hg-Ma, Cd-La, and Te-La transitions, as a function of distance along the sample cross-section. Vertical axes in all plots are arbitrary units of Intensity. Horizontal units of lower plots are in microns measured from top of film (0 μm) to film/substrate interface (17 μm).

photons that differ in energy by only ~0.06 KeV, beyond the resolution limit of EDX (~0.15 KeV) [106,107,108]. However, AES was also performed and the data indicated the presence of both HgCdTe and a-Si:H for the sample etched for 1 min. This is inconsistent with the data shown in Figure 5.7, which indicates 2 min was required for full resist erosion. These differences imply significant non-uniformity of the patterned surface. Excimer laser-exposure had been carried out with very low pulse energy densities (~43 mJ/cm^2) in attempts to minimize surface roughness. It should be mentioned that this particular experiment was performed early in the project, before the step-wise crystallization method had been adopted for achieving low surface roughness. We speculate that the low E_D produced non-uniform patterns. Most likely this non-uniformity was exacerbated during ECR plasma etching. Evidence of this can be seen in Figure 5.9, which shows a low resolution SEM image of the pattern ECR etched for 1 min.

5.4 Investigating an a-Si:H strip-etch process

We have also investigated an approach to pattern transfer that is more similar to the method used for conventional organic photoresists. That is, instead of completely removing the resist during pattern transfer, a separate etch step may be used to remove the remaining resist from mesa surfaces after desired etch depths in the underlying film are achieved. While this would add one more step to our vacuum lithography process, there are several potential advantages here. First and foremost, a two-step pattern transfer technique would make the issue of surface roughness obsolete, as the top profile would no longer be transferred to the film underneath. We

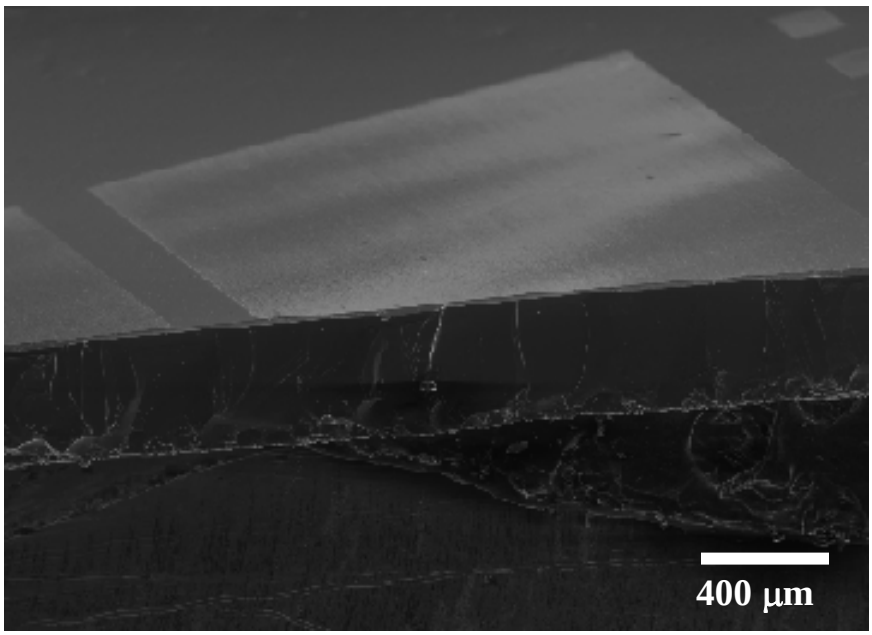

Figure 5.9. Low-resolution SEM image showing the top surface and edge of a pattern ECR etched for 1 min into an underlying HgCdTe layer. The apparent non-uniformity is likely due to the low laser fluence originally used to generate the pattern.

would also eliminate the possibility of transferring pattern non-uniformity (observed in the previous section). From a manufacturing point of view a two-step pattern transfer process is more robust, in that run-to-run variation in etch rate (caused by many factors), need not be reflected in the end product [109]. Thus an a-Si:H resist vacuum compatible "strip-etch" process could be very advantageous. Finding a feasible gas-chemistry for this plasma process however, is no simple task. Ideally the plasma should etch the a-Si:H resist with sufficient selectivity to avoid etching or damage of underlying or adjacent layers. While several plasma etch-chemistries for all forms of Si have been successfully demonstrated [110], their effects on II-VI compounds such as HgCdTe have not been studied. The most logical choice for a

starting point was a pure H_2-based plasma, which is already used during the a-Si:H development process, following laser patterning.

Our first experiments were performed using the PECVD chamber in attempts to etch off a-Si:H resist remaining after ECR etching in CdTe films. Parameters for the H-plasma used here, were identical to that used for the resist development process. However, the initial thickness and ECR etch times were selected so that the a-Si:H should be stripped after the PECVD H-plasma etch. Unfortunately, these first experiments were largely unsuccessful in that the roughness and etch depths (before and after strip-etching) remained the same. In fact, it is probable that some a-Si:H redeposition occurred during the H-plasma process as evidenced by the change in color. It was noted that oxidation or contamination may have prevented the success of these initial experiments, since venting was required to obtain profilometry measurements. Despite these uncertainties, it was decided that further a-Si:H strip etch experiments should be carried out using an ECR plasma, primarily to take advantage of its larger range of control parameters during the etch process.

We started with ECR plasma parameters similar to that for cleaning Si wafers (i.e., removing native oxide and hydrocarbons). Among other factors, this includes relatively low dc biasing, to reduce ion bombardment of the surface. Recall that H etchant atoms are primarily generated due to dissociation of H_2 molecules by Ar ions formed within the plasma zone. In the absence of Ar, less H atoms will be generated, thereby leading to lower etch rates. For a successful a-Si:H strip process, the lower etch rates must be tolerated in order to minimize etching, or damage of the II-VI material. SEM images from this experiment are shown in Figure 5.10. The micro-

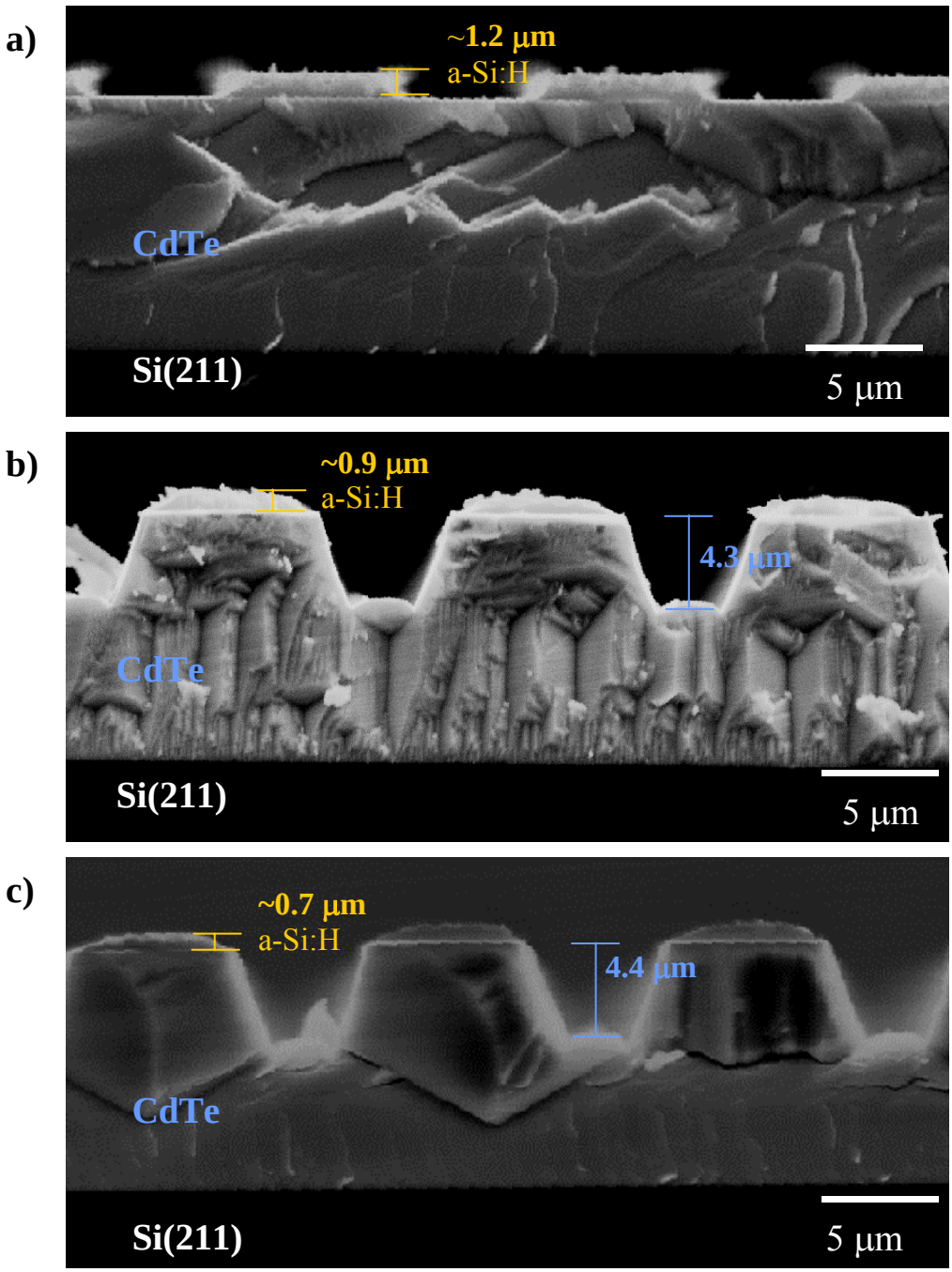

Figure 5.10: SEM micrographs showing; a) an as-developed a-Si:H pattern, b) after ECR mesa etching for 7 min, and c) after a 60 min H_2 only etch. The measured 2:1 selectivity for a-Si:H and CdTe (b and c) suggests it is possible to design a strip-etch process where the resist is completely stripped while roughly maintaining the desired etch depth.

graphs show, a) an as-developed a-Si:H layer on a CdTe film, b) after a 7 min ECR mesa-etch, and c) after a 60 min ECR H_2-strip etch. ECR plasma parameters used for the strip etch include 40 W rf power (to the substrate), 30 sccm H_2 flow rate and a 1 mTorr process pressure. During the etch, approximately 200 nm a-Si:H was removed from the mesa surface while the CdTe etch depth increased by ~100 nm, indicating a "strip-etch" selectivity of 2:1. Note that this particular experiment was designed so that a-Si:H etch rates could be measured. While we have not yet demonstrated full a-Si:H stripping using the ECR H_2-plasma procedure, Figure 5.10 suggests that it can be done.

TEM analysis was performed to determine whether the ECR mesa-etch process might alter the resist microstructure so as to influence the etch rate under H only plasmas. It was speculated that crystal grains from the laser induced poly-Si top layers may be incorporated into the underlying amorphous material during ECR plasma etching. This might effectively reduce the a-Si:H etch rate during subsequent H_2 plasma strip-etching. To investigate this possibility, cross-section TEM analysis was performed. Figure 5.11 shows a TEM BF image from a mesa edge after ECR etching for 7 min. The laser induced poly-Si top region is completely etched and does not appear to have been incorporated into the a-Si:H resist. This is confirmed by the SAD pattern which shows only diffuse rings, indicating amorphous material.

Other factors probably lead to the low etch rates observed for a-Si:H strip etching. In the case of PECVD H_2-strip etching, it is speculated that the residual a-Si:H resists had oxidized after ECR mesa-etching and removal from the vacuum system. With the poly-Si top layer removed, the underlying a:Si:H surface is severely

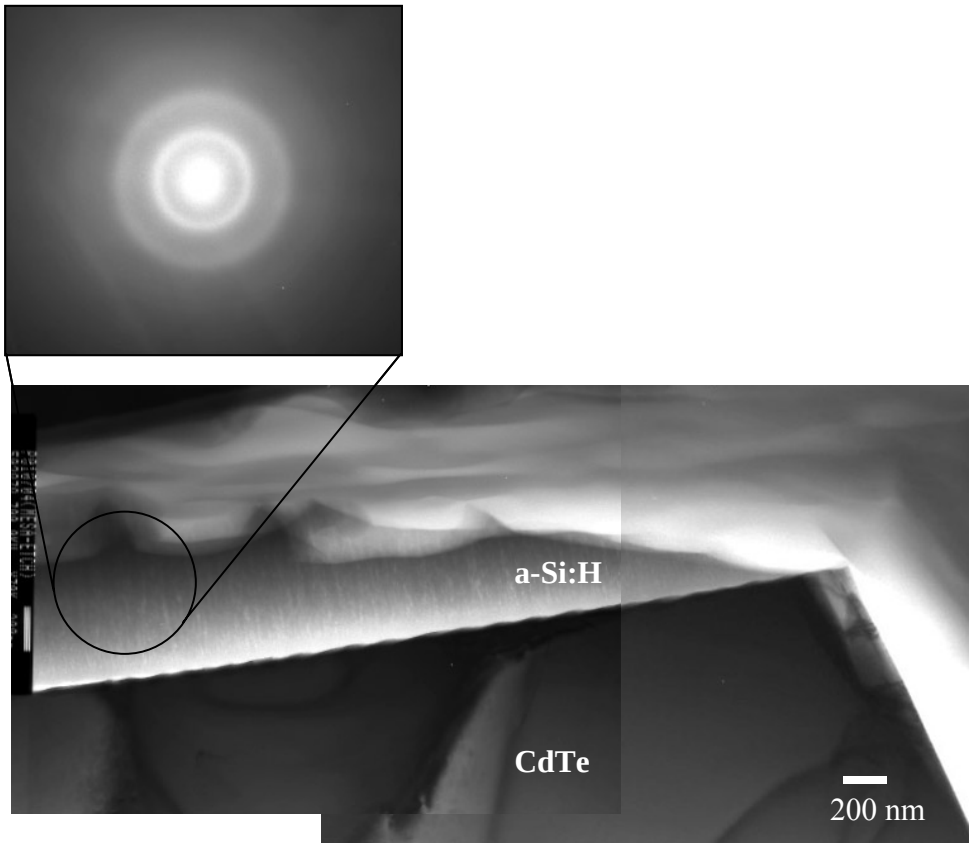

Figure 5.11: Cross-section TEM micrograph of a feature edge after ECR mesa etching for 7 min. The a-Si:H thickness was measured at 800 nm in the image but is actually ~900 nm in the center of the mesa. The selected area diffraction pattern from the upper a-Si:H region does not indicate the presence of poly-Si grains.

roughened (as seen in Fig 5.11) and would promote extensive oxidation upon exposure to air due to the overall increase in surface area. This surface would then become very resistant to the H_2 plasma etch process performed in the PECVD reactor. In-vacuo experiments are needed to confirm this speculation.

The low etch rates (~0.5 Å/s) observed for a-Si:H strip etching using the H_2-only ECR plasma, may be due to the fact that H_2 is injected into the reactor below the

plasma zone, so that a smaller number of H atoms are generated and available to etch the a-Si:H. It is expected that further experimentation with several etch parameters (H flow rate, pressure…etc) will lead to a more effective ECR H_2-plasma etch process.

5.5 Conclusions

We demonstrated the transfer of patterns in a-Si:H resists, to underlying II-VI epilayers using an ECR plasma etching system. For underlying CdTe films, a nominal etch depth of 2.5 μm was achieved using an initial a-Si:H thickness of only 300 nm. Other experiments indicated an etch selectivity of at least 8:1 for the resist and CdTe. Important aspects of pattern transfer including roughening, etch bias, and anisotropy, were also investigated. It was observed that roughness at the patterned surfaces (regardless of the particular laser treatment used) was increased by four to five times after ECR etching through the resist and into a CdTe film. However for patterns generated using step-wise crystallization, the edge roughening (observed in chapter 4) was essentially removed. This occurs due to an angular distribution of the plasma etchants, thereby leading to higher etch rates at feature edges. This angular distribution is also partially responsible for etch bias and anisotropy during the pattern transfer process. We measured an etch bias of less than 1 μm and an anisotropy of 8.8 for a ~4.5 μm deep trench using a 1.2 μm thick a-Si:H resist. In comparison, for a 1.2 μm thick conventional organic resist, the etch bias and etch anisotropy are 3.4 μm and 0.94 respectively, for a 1.6 μm etch depth in CdTe. Thus, for high anisotropy and

low etch bias, a-Si:H layers are a dramatic improvement over conventional organic resists. Note that the etch bias, and anisotropy are also affected by the initial slope of the developed a-Si:H resist at the trench opening. For further improvement we plan to explore a more anisotropic development process by using an ECR H_2 plasma procedure.

For pattern transfer into underlying HgCdTe film, an etch selectivity of 16:1 was estimated based on the slope (depth vs. time) measured through the first 2 min. However an etch depth of only 2.5 μm was achieved, though 5 μm was expected based on previous data. Discrepancies found in AES, EDX, and profilometry could only be caused by severe pattern non-uniformity. The discrepancy observed here was attributed to the low laser fluence originally used to generate the pattern. More study is needed to confirm etch selectivity of the resist for HgCdTe, and also to understand other aspects of the pattern transfer process.

Finally, we also demonstrated an ECR H_2-etch procedure that might be used to selectively strip residual a-Si:H from mesa surfaces after the mesa-etch procedure. Process parameters were employed which produced a 2:1 selectivity between residual resist and a CdTe film. This suggests a properly designed etch process can be used to completely strip the a-Si:H, while leaving the underlying film relatively unaffected. More work is needed here to further explore various process parameters, and to look for possible plasma-induced damage.

Chapter 6

Effects of the a-Si:H resist process on HgCdTe films.

6.1 Introduction

Among the controversies surrounding the vacuum lithography a-Si:H resist process, is the question of whether adverse effects are produced in the underlying film. The processing of II-VI semiconductors is already challenging because the materials tend to be soft, brittle, and thus easily damaged. HgCdTe in particular is also relatively sensitive to temperature and stress. As mentioned in chapter 1, an 80 ºC temperature limit is generally established for post-processing of HgCdTe since Hg out-diffusion may occur at higher temperatures [111]. While the temperature for a-Si:H resist deposition and development does not exceed 50 ºC, concerns have been raised about the possibility of stress at the HgCdTe near surface. That is, will the deposition of a thin a-Si:H layer produce enough stress to cause defect formation in the underlying material? However implausible, this question deserves some attention due to the fragile nature of HgCdTe.

A greater and more plausible concern has also been raised about possible damage due to excimer laser patterning. That is; is the absorption of excimer laser radiation sufficient to cause damage to the underlying HgCdTe epilayer? While the absorption depth for the 248 nm light used here is probably under 10 nm for a-Si [112], a single pulse generates a peak power density over 1 MW/cm^2 due to the short excimer pulse width (20 ns). This high power density produces a temperature field

that extends beyond the absorption depth, heating material much deeper into the surface. In fact, Cerny et al calculated a heat diffusion length of 1000 nm using a numerical simulation for irradiation of a-Si by a XeCl excimer laser [98]. This establishes a real possibility that a significant and potentially damaging temperature field could reach the HgCdTe surface following irradiation of the a-Si:H resist.

In this chapter, a preliminary investigation of the effects of the resist process on HgCdTe is presented. The study has been limited thus far to processes that take place within the vacuum lithography system, including a-Si:H deposition, laser exposure and H_2 plasma development. Structural characterization of HgCdTe films is carried out using double crystal x-ray diffraction rocking curves and transmission electron microscopy.

6.2 Effects of resist deposition

Using standard PECVD deposition conditions (section 2.2.1), a-Si:H was grown to ~350 nm on a $Hg_{0.55}Cd_{0.45}Te$/CdZnTe substrate. The a-Si:H resist thickness chosen here, is a value that would allow a 5 μm etch depth in HgCdTe after pattern transfer via ECR plasma etching. This etch depth would be suitable for fabrication of a 2nd generation IRFPA device. It should be noted that an *x* value of 0.45 is associated with material for short-wave infrared (SWIR) detection, which typically has lower defect densities than LWIR or MWIR detector material. It was decided that this material gave the best opportunity for monitoring process-induced changes in microstructure. X-ray data including a DCRC-FWHM map of the HgCdTe/CdZnTe

wafer was obtained before and after cleaving into several pieces. X-ray DCRC data was also obtained after a-Si:H deposition and after complete H_2 plasma removal.

Figure 6.1 summarizes the x-ray data from a representative sample. The (422) rocking curves overlap perfectly. The accompanying table (6.1) shows the measured x-ray FWHM for the (422) peak. An instrumental error of < 1 arcsec is typically observed when a scan is repeated several times. However, the data was obtained by attempting to scan as accurately as possible, the same sample area prior to and after each process step. X-ray FWHM wafer maps have shown variations of over 5 arcsec within a 2 mm area in similar samples. Thus the observed differences in FWHM in table 6.1 are well within the statistical error expected from the experiment. This confirms that a-Si:H deposition (or etching), does not induce significant strain or dislocations in the bulk of the underlying HgCdTe material. It is acknowledged however, that the x-rays penetrate several microns into the HgCdTe layer and would not necessarily reveal damage at the near surface. Still, even if near surface damage exists due to a-Si:H deposition and etching, it would not be a major concern. HgCdTe material below unirradiated regions of the resist (as was examined here), would eventually be removed during ECR mesa etching. Therefore it is actually ECR plasma induced damage that is the real concern regarding the HgCdTe near surface. This issue is being addressed in other studies. On the other hand, the potential damaging effect of excimer laser patterning is a greater concern and is discussed in the next section.

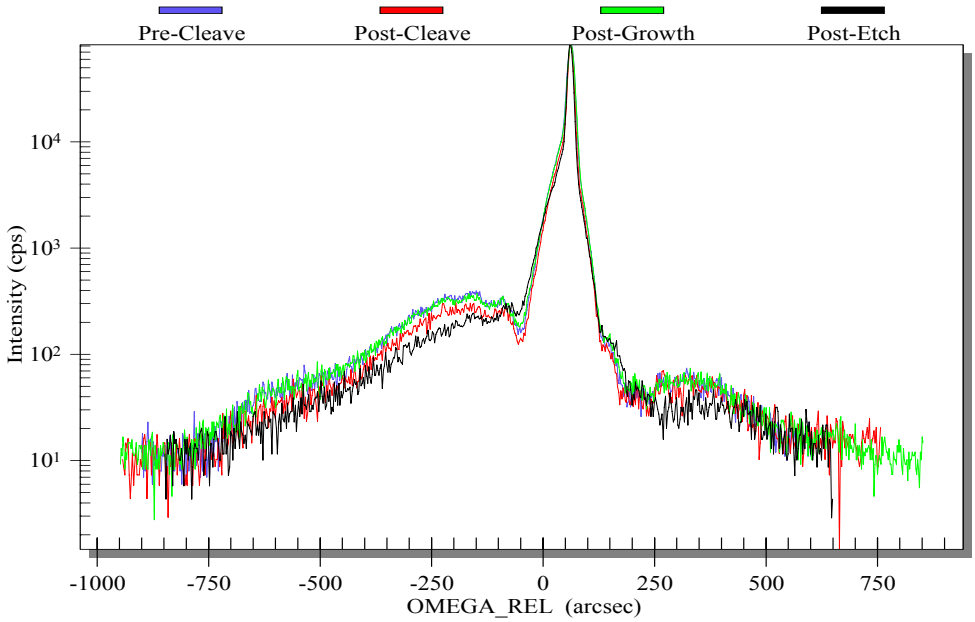

Figure 6.1: X-ray DCRC (for the (422) reflection) for a representative SWIR HgCdTe sample: before cleaving, after cleaving, after a-Si:H deposition (post-growth) and after H_2 plasma removal of the a-Si:H layer (post-etch).

	Pre-Cleave	Post-Cleave	Post-Growth	Post-Etch
FWHM (arc-sec)	16.8	15.2	17.0	15.0

Table 6.1: DCRC FWHM data for the scans shown in Figure 6.1.

6.3 Effects of excimer laser patterning

To understand the concerns regarding possible HgCdTe damage due to the laser exposure process, it is instructive to briefly review the mathematical model of laser-induced phase changes in a-Si proposed by Cerny and Prikryl [98]. The authors simulated the irradiation of a-Si on a quartz substrate by a XeCl laser (λ = 308 nm, pulse width = 28 ns). Material properties of a-Si and liquid Si including specific heat, (c), density (ρ), and thermal conductivity (K), was obtained from various sources [113-115]. For poly-Si however, the same data was not available and thus certain estimates were used. For example, the "equilibrium explosive crystallization temperature," T_{xc} was chosen to be equal to the melting temperature of a-Si. That is $T_{xc} = T_m^{a-Si}$ = 1200 K or 927 ºC [116]. Figure 6.2 shows the calculated a-Si surface temperature (a), and substrate temperature (b) caused by various incident energy densities. An a-Si layer thickness of 100 nm was used in the simulation. The initial spikes in (a) for energies above 50 mJ/cm^2 are due to a fast release of latent heat and indicate the onset of explosive crystallization. Note that this occurs at T_m^{a-Si}. At $E_D \geq$ 150 mJ/cm^2, the entire a-Si film melts, as indicated by the plateau. In Fig 6.2(b) it is evident that a substantial temperature rise occurs at the substrate even for energies below the threshold for full melting of the film and even below the threshold for explosive crystallization. At 50 mJ/cm^2, the substrate sees a peak temperature higher than 600 K (or 327 ºC). In addition, the authors calculated a heat-diffusion length, l_H = 1000 nm using the relationship,

$$l_H = \sqrt{\frac{K}{\rho c} t_p} \qquad \text{(eq 6.1)}$$

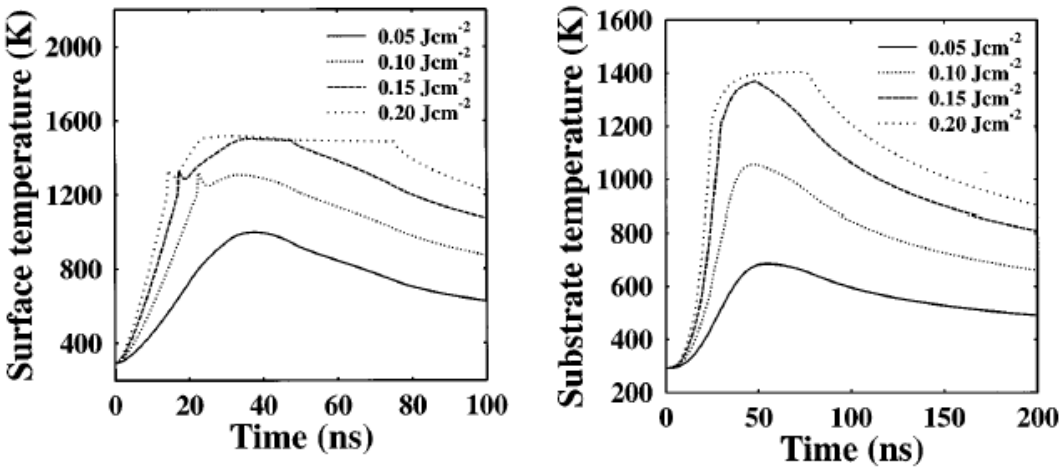

Figure 6.2: Numerical simulation of the time histories of an a-Si surface and substrate surface temperatures following laser irradiation at various energy densities. An a-Si thickness of 100 nm was used in the simulation. Reprinted from Cerny and Prikryl [98].

where K is the thermal conductivity, and t_p is the time interval.

The implications for the a-Si:H films in our study are the following: Despite the small absorption depth of the laser radiation (~10 nm for $\lambda = 248$ nm), and despite the fact that the entire a-Si:H resist layer is *not* melted, the possibility of a significant rise in substrate temperature cannot be ignored. The $Hg_{1-x}Cd_xTe$ melting point is about 950 ºC [1], and probably decreases for smaller x values since $T_m^{HgTe} = 670$ ºC. The possible melting of the HgCdTe near surface is not the only concern however. Due to the high vapor pressure of Hg, any rise in temperature (above 80 ºC) may lead to Hg out-diffusion. Hg deficient films have been associated with the precipitation of Te grains, which are typically incoherent with respect to the surrounding lattice [117]. The experiment described below is designed to examine the possibility of such

microstructural changes in the HgCdTe near surface due to laser induced heating of the a-Si:H layer.

As in the previous section, a 350 nm thick a-Si:H layer was deposited onto a $Hg_{0.55}Cd_{0.45}Te$/CdZnTe substrate. After deposition, excimer laser irradiation was carried out in vacuum at 10^{-7} Torr using a single ~65 mJ/cm^2 pulse. Note that this is sufficient energy to crystallize the surface and to allow for full development of the a-Si:H resist (see Figure 3.5). To examine the effects of the exposure process on the HgCdTe near surface, cross-section TEM analysis was performed. However, a meaningful analysis requires examination of two additional samples, including a HgCdTe sample that is not subjected to any further processing and one that is directly exposed to a 65 mJ/cm^2 pulse. Analysis of the first sample provides a benchmark for the ideal HgCdTe near surface. Analysis of the second sample provides a benchmark for the maximum structural damage due to absorption of laser energies typically used throughout this thesis. The results are presented in Figures 6.3-6.5. A cross-section BF TEM image of an unprocessed HgCdTe film (i.e., no a-Si:H deposition and/or laser exposure) is shown in Fig 6.3. A SAD pattern is shown in the inset and indicates the <110> zone axis, which is used during the analysis. The contrast observed < 100 nm below the surface (in the low-magnification image) is due to a high *x*-value cap layer, which is typically deposited at the end of the MBE growth process. The high-resolution image of the near surface shows high crystalline quality and an almost atomically flat profile. Fig 6.4 shows an image of a HgCdTe surface that is directly exposed using a single 65 mJ/cm^2 pulse (carried out in vacuum at ~10^{-7} Torr). Here, a highly defective region is clearly visible extending approximately 75

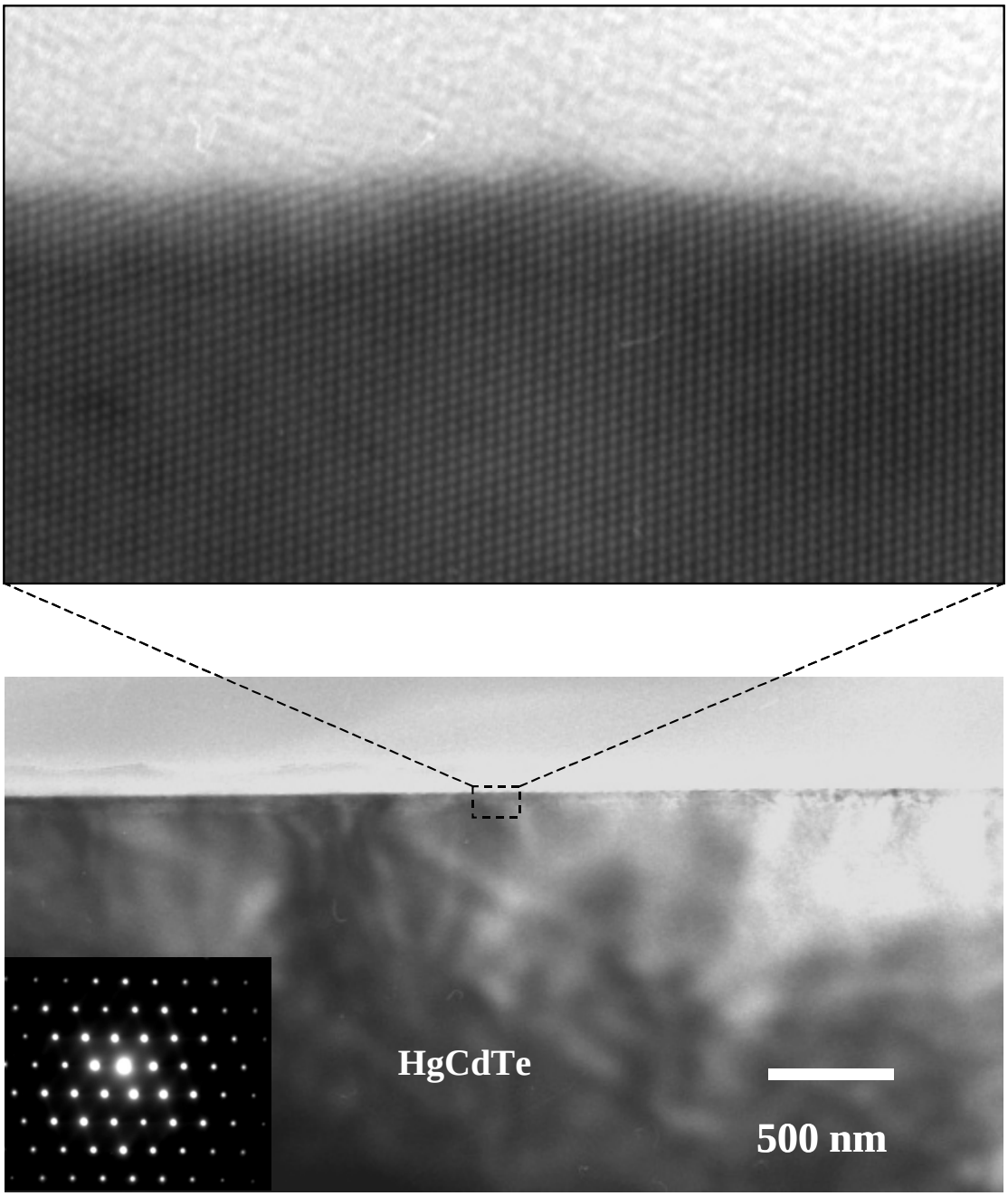

Figure 6.3: X-section BF TEM image (lower) from the surface of an unprocessed HgCdTe film. High crystalline quality is confirmed by the (110) SAD pattern (inset), and also by the high resolution image (upper).

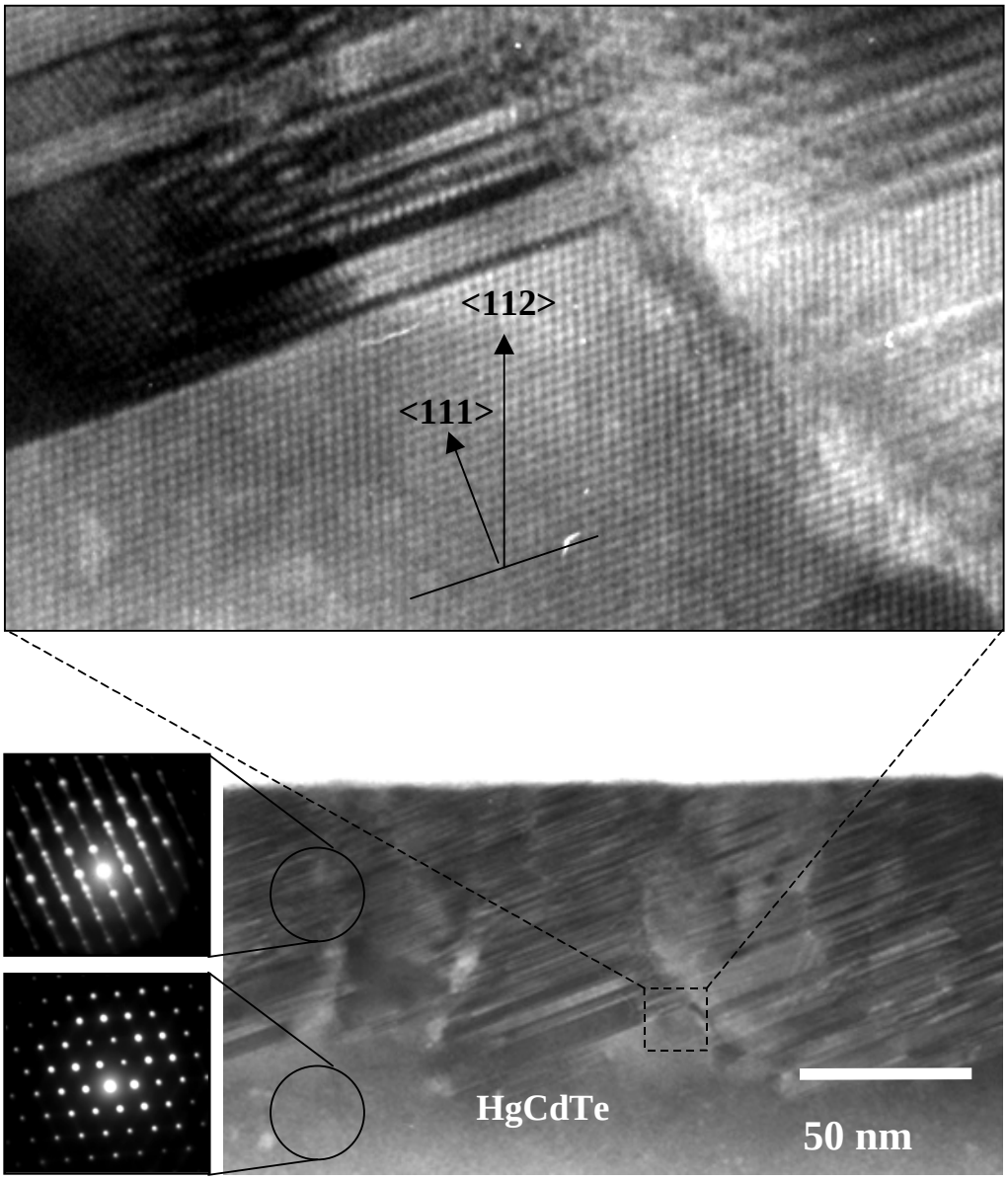

Figure 6.4: X-section BF TEM image (lower) from the surface of a HgCdTe film that was directly exposed to a 65 mJ/cm^2 laser pulse. SAD patterns indicate respective structures from defective (upper) and unaffected (lower) region. The HR image (top) shows a high density of defects including stacking faults and twining where the twin boundary is along a (111) plane. The unaffected HgCdTe lattice structure is also seen just below the damaged region.

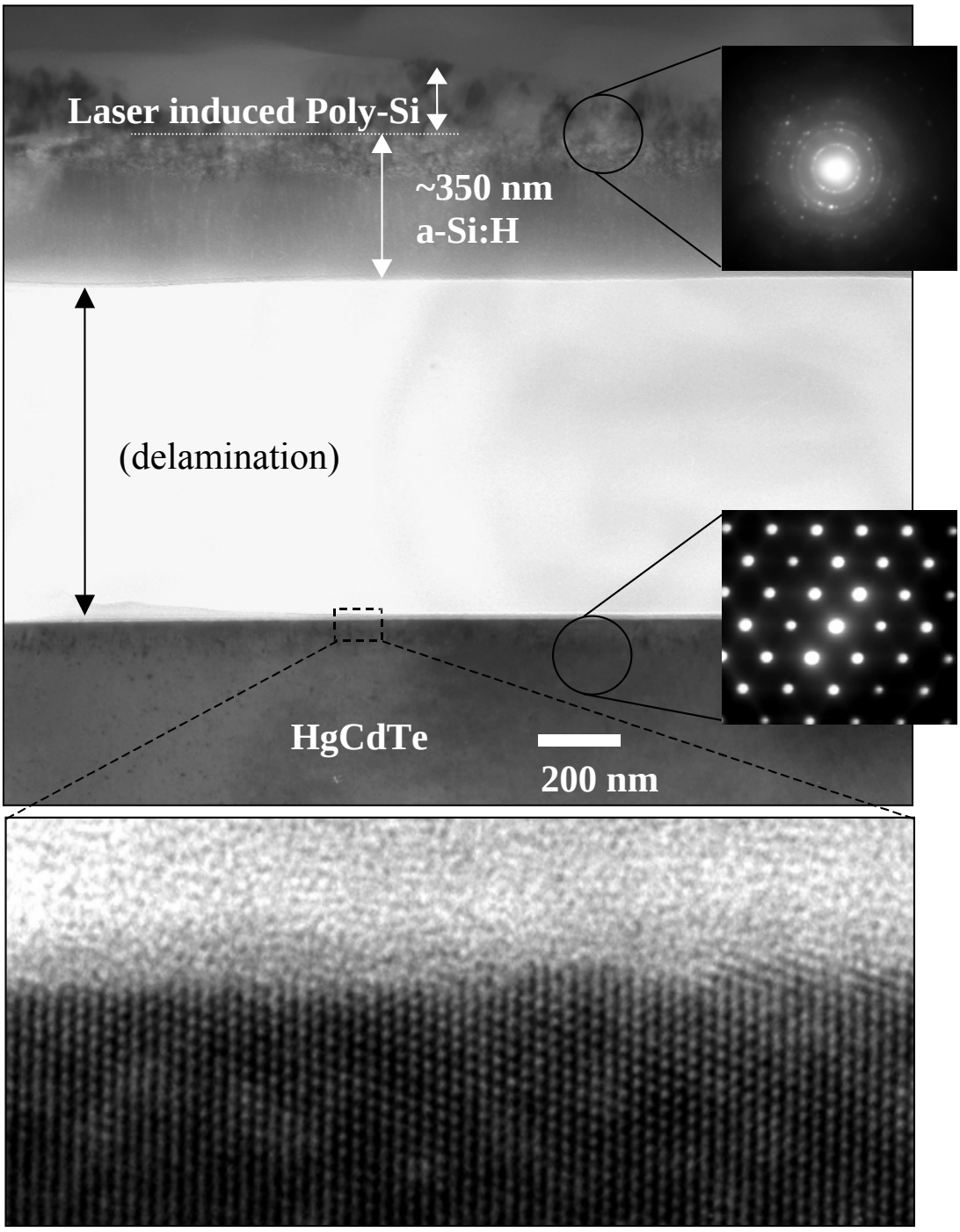

Figure 6.5: X-section BF TEM image (top) from an a-Si:H layer that was deposited on a HgCdTe film and exposed using a single 65 mJ/cm^2 laser pulse. SAD patterns indicate respective structures from laser-induced poly-Si (upper) and near surface HgCdTe region (lower). The HR image (bottom) shows high quality single crystal structure in near surface HgCdTe region.

nm below the surface. The region is heavily twinned, and shows a high density of {111} stacking faults (confirmed via the SAD pattern A). The high resolution image from the selected region indicates a distinct boundary between the defective area and the underlying material, which maintains its structure. This is also confirmed in SAD pattern B. Finally, Fig 6.5 shows the image from an a-Si:H layer that was deposited on the HgCdTe film and then exposed using a single 65 mJ/cm^2 pulse. The upper SAD pattern indicates a polycrystalline region at the surface of the a-Si:H resist, confirming laser exposure has been performed. It is also evident, that the a-Si:H layer has been delaminated (unintentionally) at some point during processing. However, there is strong evidence to assert that this delamination occurred after ion milling which is the final step in TEM sample preparation (section 2.6.2.2). The low resolution image shows a relatively flat and undisturbed surface and more importantly, contrast from the low *x*-value cap layer (< 100 nm thick) is evident. Thus, we may confidently state that despite the apparent delamination, near surface HgCdTe material has not been removed. As such, the lower SAD pattern and high resolution image suggest no microstructural changes due to laser exposure of the resist layer. There is no defective near surface region as seen in Fig 6.4, and the observed crystalline quality is identical to that shown in Fig 6.3.

The results show that the laser fluences, and a-Si:H resist thicknesses used for lithographic patterning in this work, will *not* result in microstructural damage to an underlying HgCdTe (x = 0.45) epilayer. In addition, questions regarding certain thermophysical properties of the a-Si:H resist compared to pure a-Si may be qualitatively answered. Firstly, the thermal diffusion length (l_H) for the a-Si:H films

in this thesis must be smaller than that for pure a-Si. The value of l_H = 1000 nm determined for a-Si from numerical simulations would clearly exceed the 350 nm thick resists in our study, resulting in unacceptable temperature fields at the HgCdTe near surface. Going back to eq. 6.1, this may be due to a-Si:H having a smaller thermal conductivity, *K*. In turn, a smaller *K* might be explained by the fact that the existence of H tends to reduces the average network coordination [49], thereby reducing the connectivity of the amorphous network and reducing heat flow. A smaller *K* can also be expected in our case, due to the known columnar structure of the a-Si:H resist (due to Ar dilution during deposition). Large voids would act as insulating gaps and also contribute to reduced heat flow.

6.4 Conclusions

In summary, a preliminary investigation of the effects of the a-Si:H resist process on HgCdTe films was carried out. To determine whether the deposition process produces stress in the underlying film, x-ray DCRC was carried out. DCRC FWHM measurements showed that no measurable strain or change in crystal quality is incurred due to the resist deposition (or plasma removal) process. To examine the possibility of HgCdTe near surface damage due to the combination of a-Si:H resist deposition and laser-induced heating of the resist layer, x-section TEM analysis was performed. The results showed that the damage observed due to direct laser exposure of HgCdTe, is not observed when exposure takes place through a thin (350 nm) a-Si:H overlayer. Due to both the small absorption length of excimer radiation and an evidently small thermal diffusion length in our a-Si:H material, the exposure process

does not result in HgCdTe near surface melting or significant Hg out-diffusion which would lead to obvious microstructural changes. Note that a much thinner resist layer would probably not provide enough "insulation" to protect the underlying HgCdTe material during laser exposure. A minimum resist thickness required to avoid damage of the HgCdTe film has not been determined. However thinner resist layers would be used only if required for a predetermined HgCdTe etch depth, in which case, a lower energy density would be required for lithography.

Chapter 7

Summary and Future Work

In this work, an investigation of a-Si:H for a novel dry lithography technology was carried out. The process has been used to pattern and develop pixels in HgCdTe and CdTe thin films, but could potentially be used for the lithography of other semiconductors as well. The significance of this work has been the increased understanding of the a-Si:H dry lithography procedure. The use of laser induced poly-Si etching masks has been demonstrated along with the use of a step-wise crystallization procedure for eliminating undesirable surface roughness. A potential strip-etch technique was also demonstrated as an alternative to simultaneous pattern transfer and resist removal. In addition, controversies surrounding the possible damage induced by the a-Si:H dry lithography process has been partially addressed via x-ray and TEM analysis.

Prior to this work, a proof of concept had been carried out where MWIR HgCdTe diodes were successfully fabricated but were below state of the art. However, the need for all-vacuum compatible lithography of HgCdTe prompted further study and development of the a-Si:H resist technique. Among other changes, resist deposition via Ar-diluted SiH_4 precursors was adopted to improve upon the original technique, by reducing undesirable gas phase particulates and creating a more environmentally benign process. The effects of argon dilution (in the depositing gas) on PECVD a-Si:H films, and on its use in this dry lithography technology were

investigated in chapter 3. Excimer Laser patterning was performed in different ambients and using different energy fluences prior to hydrogen plasma development. IR absorption spectra were also used to estimate the relative H content in a-Si:H films deposited from different Ar/SiH_4 mixtures. It was concluded that lithographically definable patterns in material deposited with Ar-diluted SiH_4 could not be realized by UV enhanced oxidation due to a lack of H passivation in the deposited resist. It was demonstrated that the resists could be patterned via laser induced melting and crystallization. The laser induced poly-Si patterns showed a development etch selectivity of over 1000:1 (during hydrogen plasma etching), but the observed surface roughness (R_a~15-30 nm) created another problem. The process was originally designed such that pattern transfer and resist removal should occur in a single etching step, so that roughness would inevitably be replicated (if not enhanced) in the underlying device layer. In this dissertation, two possible techniques (chapter 4 and chapter 5.4) were investigated for overcoming this problem.

In chapter 4, techniques for reducing the roughness in laser induced poly-Si surfaces were explored with the specific goal of satisfying the requirement: $R_a^{\text{exposed}} \approx R_a^{\text{as-deposited}}$. The stringent requirements of our lithographic process (due to the fragile nature of II-VI materials), precluded the use of roughness reduction methods found in the literature. Nonetheless a modified step-wise crystallization technique was demonstrated and shown to consistently produce poly-Si patterns with low roughness. IR absorption data indicated that step-wise crystallization proceeds via slow hydrogen desorption of the a-Si:H film and helped explain why much lower energy density increments were required for the films in our study. Namely, a-Si:H with higher

initial hydrogen content (due to low temperature deposition), will require smaller increments in energy to avoid explosive dehydrogenation (and roughness) of the film. On the other hand X-section TEM also showed much smaller grain sizes for films treated by the step-wise crystallization procedure. It was concluded that low roughness is due to both of these factors.

An alternate method for addressing the issue of undesired pattern roughness was also demonstrated. The addition of a separate plasma step to strip the resist after mesa etching was investigated as a means to eliminate surface roughness. In chapter 5 a potential technique for etching the residual a-Si:H resist (after mesa etching) was investigated. Here an ECR plasma consisting of pure H injected below the established "ECR" zone, was employed to selectively remove a-Si:H from mesa surfaces. An a-Si:H/CdTe etch selectivity of approximately 2:1 was observed via SEM micrographs. The key process parameter here was probably the low rf power to the substrate (40 W) in order to reduce ion bombardment and significant etching of the II-VI material. Since H radicals etch Te, (in addition to the resist) it appears that a trade off exists between high selectivity and short process time. A relatively long process time (60 min) was required for the strip-etch experiment described in chapter 5, where approximately 200 nm of the resist was removed. However the plasma recipe is still under development and optimization of various parameters are expected to improve the technique. Future work will also be carried out to determine to what extent the HgCdTe or CdTe surface is damaged by the ECR plasma.

Fundamental aspects of ECR pattern transfer (mesa etching) using a-Si:H resists was also investigated in chapter 5. Here, etch selectivities of approximately

8:1 and 16:1 for CdTe/a-Si:H and HgCdTe/a-Si:H, respectively, were estimated. Due to a low etch rate in the ECR Ar/H_2 plasma, the resists showed high etch anisotropy and low etch bias in comparison to a conventional organic resist. This suggests that features with deep trenches and high aspect ratios needed for next generation IRFPAs could be fabricated using our dry-lithography technology.

A preliminary investigation of the effects of the a-Si:H resist process was presented in chapter 6. DCRC XRD showed no evidence of stress induced defects in a HgCdTe film after deposition and H etching of a 350 nm thick a-Si:H layer. In numerical simulations for laser crystallization of pure a-Si (with similar E_D), high temperature fields were predicted at the substrate surface [98]. In our case a HgCdTe "substrate" would potentially be damaged by these high temperature fields. X-section TEM analysis of HgCdTe surfaces were performed after excimer laser irradiation with typical energy densities. High-resolution images showed no evidence of near surface damage, suggesting that the effective thermal diffusion length in our a-Si:H material is shorter than the film thicknesses. These results confirm that the dry lithography process does not induce structural damage to the underlying material. It has not however, been confirmed that the surface stoichiometry (of the HgCdTe film) remains the same throughout the process. This is an important aspect that will be investigated via in situ surface analysis in the near future.

The further study, evaluation and development of the a-Si:H dry resist technology will require substantial surface analysis. Our dry-resist technology promises to be clean and free of contaminants, and thus in-vacuo surface analysis must be performed after every process step involved. HeNe laser interferometry is

used for endpoint detection during hydrogen development etching, but Auger analysis can confirm full development and also etch uniformity. In addition to AES, XPS will also help to examine HgCdTe surface stoichiometry after hydrogen development of the resist, and after the ECR plasma strip procedure. Finally, the full benefits of the a-Si:H dry resist process cannot be realized without significant testing of HgCdTe PV diodes fabricated using the technology. This will involve full device fabrication and hybridizing to a ROIC to enable characterization such as *I-V* curves, R_0A vs. temperature, and quantum efficiency. Future collaborations with an NVESD contractor will help to fill this knowledge gap.

References

1. P. Norton, *Opto-Electronics Rev.* **10**(3), 159 (2002).
2. R. Gaughan, *Photonics Spectra*, p. 78 (Nov, 2003).
3. M.C. Tamargo, *II-VI Semiconductor Materials and Their Applications* (Ann Arbor: Taylor & Francis, 2002) p. vii.
4. P. Mitra, F.C. Case, and M. B. Reine, *J. Electron. Mater*. **27**, 510 (1998).
5. C. Kittel, *Introduction to Solid State Physics. Seventh Ed*., (New York: John Wiley & Sons Inc. 1996) p. 201.
6. R. Dalven, *Introduction to Applied Solid State Physics. 2nd Ed*., (New York: Plenum Press, 1990) p. 191.
7. M.A. Kinch, *J. Electron. Mater*. **29**, 809 (2000).
8. T.J. de LYON, A. Roth, O.K. Wu, S.M. Johnson, and C.A. Cockrum, *Appl. Phys. Lett.* **63**, 818 (1993).
9. M.C. Tamargo, *II-VI Semiconductor Materials and Their Applications* (Ann Arbor: Taylor & Francis, 2002) p. 5-6.
10. T.J. de LYON, J.E. Jenson, M.D. Gorwitz, C.A. Cockrum, S.M. Johnson, and G.M. Venzor, *J. Electron. Mater*. **28**, 705 (1999).
11. J.B. Varesi, A.A. Buell, J.M. Peterson, R.E. Bornfreund, M.F. Vilela, W.A. Radford, and S.M. Johnson., *J. Electron. Mater*. **32**, 661 (2003).
12. J.M. Arias, J.G. Pasko, M. Zandian, L.J. Kozlowski, and R.E. DeWames, *Opt. Eng*., **33** 1422 (1994).
13. J.M. Arias, J.G. Pasko, M. Zandian, J. Bajaj, L.J. Kozlowski, R.E. DeWames, and W.E. Tennant, *Proceedings of the Society for Photo-Optical Instrumentation for Engineers*, Edited by H.K. Pollehn and R.S. Balcerak, **2228** p.210 (SPIE, Bellingham, WA, 1994).
14. J. Bajaj, J.M. Arias, M. Zandian, J.G. Pasko, L.J. Kozlowski, R.E. DeWames, and W.E. Tennant, *J. Electron. Mater*. **24**, 1394 (1995).
15. D.D. Edwall, M. Zandian, A.C. Chen, and J.M. Arias, J. Electron. Mater., 26 493 (1997).
16. H. Wei, Ph.D. Thesis, University of Maryland, College Park, MD (1998) p. 141.

17. N.K. Dhar, C.E. Wood, A. Gray, H.Y. Wei, L. Salamanca-Riba, and J.H. Dinan, *J. Vac. Sci. Technol. B,* **14** (3) (1996).
18. N.K. Dhar, C.E. Wood, *J. Appl. Phys.* 78 (7) (1995).
19. M.A. Lieberman and A.J. Lichtenberg, *Principles of Plasma Discharges and Materials Processing* (New York: John Wiley & Sons, Inc, 1994) pp. 1-5.
20. C.Y. Chang and S.M. Sze, *ULSI Technology* (New York: McGraw-Hill Inc, 1996) p. 329.
21. C.A. Musca, J.M. Dell, L. Faraone, J. Bajaj, T. Pepper, K. Spariosu, J. Blackwell, and C. Bruce, *J. Electron. Mater*. **28**, 617 (1999).
22. E.P.G. Smith, L.T. Pham, G.M. Venzor, E.M. Norton, M.D. Newton, P.M. Goetz, V.K. Randall, A.M. Gallagher, G.K. Pierce, E.A. Patten, R.A. Coussa, K. Kosai, W.A. Radford, L.M. Giegerich, J.M. Edwards, S.M. Johnson, S.T. Baur, J.A. Roth, B. Nosho, T.J. De Lyon, J.E. Jensen, and R.E. Longshore, *J. Electron. Mater*. **33**, 509 (2004).
23. P. O'Dette, G. Tarnowski, V. Lukach, M. Krueger, and P. Lovecchio, *J. Electron. Mater*. **28**, 821 (1999).
24. A.J. Stoltz, M.R. Banish, J.H. Dinan, J.D. Benson, D.R. Brown, D.B. Chenault, and P.R. Boyd, *J. Electron. Mater*. **30**, 733 (2001).
25. Private Communication.
26. J.N. Johnson, L.A. Almeida, J.D. Benson, J.H. Dinan, and M. Martinka, *J. Electron. Mater*. **27**, 657 (1998).
27. R.E. Hollingsworth, C. Dehart, L. Wang, J.N. Johnson, J.D. Benson, and J.H. Dinan. *J. Electron. Mater*. **27**, 689 (1998).
28. C.Y. Chang and S.M. Sze, *ULSI Technology* (New York: McGraw-Hill Inc, 1996) p. 341.
29. M. Mullenborn, K. Birkelund, F. Grey, and S. Madsen, *Appl. Phys. Lett.* **69**, 3013 (1996).
30. N. Kramer, M. Niesten, and C. Schonenberger, *Appl. Phys. Lett.* **67**, 2989 (1995).
31. R.A. Street, Hydrogenated Amorphous Silicon. (Cambridge: Cambridge University Press, 1991) p. 18.

32. T.W. Weidman and A. M. Joshi *Appl. Phys. Lett.* **62**, 372 (1993).
33. M.W. Horn, S.W. Pang, and M. Rothschild, *J. Vac. Sci. Technol. B,* **8** (6), 1493 (1990).
34. M.S. Hagedorn, T.K. Higman, R.T. Fayfield, and J. Chen, *J. Vac. Sci. Technol. B,* **13** (3), 862 (1995).
35. K. Shiralagi and R. Tsui, *Appl. Phys. Lett*. **74**, 886 (1999).
36. M. Ohring, *The Materials Science of Thin Films* (San Diego: Academic Press, 1992) p. 336.
37. S. Sivananthan, P.S. Wijewarnasuriya, F. Aqariden, H.R. Vydyanath, M. Zandian, D.D. Edwall, and J.M. Arias, J. Electron. Mater., **26**, 621 (1997).
38. M.A. Berding, A. Sher, and M. Van Schilfgaarde, J. Electron. Mater., 2**6**, 625 (1997).
39. L.A. Almeida, N.K. Dhar, M. Martinka, and J.H. Dinan, J. Electron. Mater. **29**, 754 (2000).
40. D.B. Fenner, D.K. Biegelsen, and R.D. Bringhans, J. Appl. Phys. **66**, 419 (1989).
41. Million, N.K. Dhar, J.H. Dinan, J. Cryst. Growth. **159**, 76 (1996
42. H. Wei, Ph.D. Thesis, University of Maryland, College Park, MD (1998) p. 11.
43. L.A. Almeida, J.N. Johnson, J.D. Benson, J.H. Dinan, and B. Johs, *J. Electron. Mater*. **27**, 500 (1998).
44. L.A. Almeida and J.H. Dinan, J. Cryst. Growth. **201/202**, 22 (1999).
45. M.A. Lieberman and A.J. Lichtenberg, *Principles of Plasma Discharges and Materials Processing* (New York: John Wiley & Sons, Inc, 1994) pp. 6-11.
46. R.A. Street, Hydrogenated Amorphous Silicon. (Cambridge: Cambridge University Press, 1991) p. 20-21.
47. R.A. Street, J.C. Knights, and D.K. Biegelsen, Phys. Rev. B. **18**, 1880 (1978).
48. J.C. Knights, and G. Lucovsky, CRC Critical Reviews in Solid State and Materials Sciences. **21**, 211 (1980).
49. R.A. Street, Hydrogenated Amorphous Silicon. (Cambridge: Cambridge University Press, 1991) p. 37-39.
50. J.C. Knights, *Jap. J. Appl. Phys.* **18-1**, 101 (1979).

51. M.A. Lieberman and A.J. Lichtenberg, *Principles of Plasma Discharges and Materials Processing* (New York: John Wiley & Sons, Inc, 1994) p. 516.
52. R.A. Street, Hydrogenated Amorphous Silicon. (Cambridge: Cambridge University Press, 1991) p. 30.
53. C.Y. Chang and S.M. Sze, *ULSI Technology* (New York: McGraw-Hill Inc, 1996) p. 363.
54. A. Gallagher and J. Scott, J. Solar Cells. **21**, 147 (1987).
55. M.A. Lieberman and A.J. Lichtenberg, *Principles of Plasma Discharges and Materials Processing* (New York: John Wiley & Sons, Inc, 1994) pp. 4-5.
56. Night Vision Electronic Sensors Directorate 1998 SBIR, Unpublished data.
57. C.Y. Chang and S.M. Sze, *ULSI Technology* (New York: McGraw-Hill Inc, 1996) p. 273.
58. C.Y. Chang and S.M. Sze, *ULSI Technology* (New York: McGraw-Hill Inc, 1996) p. 284.
59. M. Ohring, *The Materials Science of Thin Films, 2nd Ed.* (San Diego: Academic Press, 2002) p. 326.
60. C.Y. Chang and S.M. Sze, *ULSI Technology* (New York: McGraw-Hill Inc, 1996) p. 348.
61. J.D. Benson, A.J. Stoltz, A.W. Kaleczyc, M. Martinka, L.A. Almeida, P.R. Boyd, and J.H. Dinan, *J. Electron. Mater*. **31**, 822 (2002).
62. R.N. Jacobs, A.J. Stoltz, E.W. Robinson, P.R. Boyd, L.A. Almeida, J.H. Dinan, and L. Salamanca-Riba, *J. Electron. Mater*. **33**, 538 (2004).
63. M. Ohring, *The Materials Science of Thin Films, 2nd Ed.* (San Diego: Academic Press, 2002) pp. 576-578.
64. D.B. Williams and C.B. Carter, *Transmission Electron Microscopy* (New York: Plenum Press, 1996) p. 141.
65. G. Thomas and M.J. Goringe, *Transmission Electron Microscopy of Materials* (John Wiley and Sons, 1979).
66. M. Ohring, *The Materials Science of Thin Films* (San Diego: Academic Press, 1992) p. 269-273.

67. H. Wei, Ph.D. Thesis, University of Maryland, College Park, MD (1998) p. 19-20.
68. H. Li, L. Salamanca-Riba, Ultramicroscopy. **88**, 171 (2001).
69. R.N. Jacobs, M.S. Thesis, University of Maryland, College Park, MD (2001) p. 25.
70. M. Ohring, *The Materials Science of Thin Films, 2nd Ed.* (San Diego: Academic Press, 2002) p. 586
71. L.E. Murr, *Electron and Ion Microscopy and Microanalysis 2nd Ed Revised and Expanded* (New York: Marcel Dekker, Inc, 1991) p 305.
72. M. Ohring, *The Materials Science of Thin Films, 2nd Ed.* (San Diego: Academic Press, 2002) pp. 610, 615.
73. M. Ohring, *The Materials Science of Thin Films, 2nd Ed.* (San Diego: Academic Press, 2002) pp. 611, 616.
74. A.A. Langford, M.L. Fleet, B.P. Nelson, W.A. Lanford, N. Maley, *Phys. Rev. B*, **45**, 13367 (1992).
75. G. Lucovsky, R.J. Nemanich, and J.C. Knights, *Phys. Rev. B*, **19** 2064 (1979).
76. J.R. Ferrao and L.J. Basile, *Fourier Transform Infrared Spectroscopy. Applications to Chemical Systems. Vol 1*. (Academic Press: New York 1978) pp. 18-21.
77. M. Ohring, *The Materials Science of Thin Films, 2nd Ed.* (San Diego: Academic Press, 2002) pp. 598.
78. N. Kramer, J. Jorritsma, H. Birk, and C. Schonenberger, J. Vac. Sci. Technol. B **13**, 805 (1995).
79. J.C. Knights, R.A. Lujan, M.P. Rosenblum, R.A. Street, D.K. Biegelsen, and J. Reimer, *Appl. Phys. Lett*. **38**, 331 (1981).
80. R.N. Jacobs, A.J. Stoltz, J.H. Dinan, and L. Salamanca-Riba, *J. Vac. Sci. Technol. B,* **22**(3), 1071 (2004).
81. Internal data (unpublished).
82. R.A. Street, Hydrogenated Amorphous Silicon. (Cambridge: Cambridge University Press, 1991) p. 54.
83. R.T. Collins, M.A. Tischler, and J.H. Stathis, *Appl. Phys. Lett*. **61**, 1649 (1992).

84. P. Lengsfeld, N.H. Nickel, and W. Fuhs, *Appl. Phys. Lett*. **76**, 1680 (2000).
85. L. Wang, J. Li, X. Huang, Q. Li, X. Yin, W. Fan, J. Xu, W. Li, Z. Li, J. Zhu, M. Wang, Z. Liu, K. Chen, *Appl. Surf. Sci.* **165**, 85 (2000).
86. R.A. Street, Hydrogenated Amorphous Silicon. (Cambridge: Cambridge University Press, 1991) p. 26-27, 58-56.
87. R.A. Street, Hydrogenated Amorphous Silicon. (Cambridge: Cambridge University Press, 1991) p. 47.
88. H. Shanks, C.J. Fang, L. Ley, M. Cardona, F.J. Demond, and S. Kalbitzer. *Phys. Stat. Sol. (b)* **100**, 43 (1980)
89. E.C. Freeman and W. Paul, *Phys. Rev. B*. **18**, 4288 (1978).
90. R.A. Street, Hydrogenated Amorphous Silicon. (Cambridge: Cambridge University Press, 1991) p. 26.
91. M.C. Tamargo, *II-VI Semiconductor Materials and Their Applications* (Ann Arbor: Taylor & Francis, 2002) p. 2.
92. D. Toet, P.M. Smith, T.W. Sigmon, T. Takehara, C.C. Tsai, W.R. Harshbarger, and M.O. Thompson, *J. Appl. Phys.* **85**, 7914 (1999).
93. M. Yuki, K. Masumo, S. Takafuji, T. Asakawa, N. Imajyo and M. Kunigita, Proc. 1988 Int'l Display Research Conference, San Diego, (IEEE Publication, New York, 1988) p 220.
94. P. Mei, J.B. Boyce, M. Hack, R.A. Lujan, R.I. Johnson, G.B. Anderson, D.K. Fork, S.E. Ready, and D.L. Smith, *Mater. Res. Soc. Symp. Proc*. **297**, 151 (1993).
95. P. Mei, J.B. Boyce, M. Hack, R.A. Lujan, S.E. Ready, D.K. Fork, R.I. Johnson, and G.B. Anderson, *J. Appl. Phys.* **76**, 3194 (1994).
96. P. Mei, J.B. Boyce, M. Hack, R.A. Lujan, S.E. Ready, D.K. Fork, R.I. Johnson, and G.B. Anderson, *Appl. Phys. Lett.* **64**, 1132 (1994).
97. D.J. Ehrlich, J.Y. Tsao, *Laser Microfabrication, Thin Film Processes and Lithography*, (San Diego: Academic Press Inc, 1989) p. 65-66.
98. R. Cerny, P. Prikryl, *Phys. Rev. B.* **57**, 194 (1998).
99. R.A. Street, Hydrogenated Amorphous Silicon. (Cambridge: Cambridge University Press, 1991) p. 26.

100. E.P.G. Smith, C.A. Musca, D.A. Redfern, J.M. Dell, L. Faraone, *J. Electron. Mater*. **29**, 853 (2000).
101. L.S. Hirsch, Z. Yu, S.L. Buczkowski, T.H. Myers, and M.R. Richards-Babb, *J. Electron. Mater*. **26**, 534 (1997).
102. J.N. Johnson, L.A. Almeida, M. Martinka, J.D. Benson, and J.H. Dinan, *J. Electron. Mater*. **28**, 817 (1999).
103. J.D. Benson, A.J. Stoltz, P.R. Boyd, M. Martinka, J.B. Varesi, L.A. Almeida, K.A. Olver, A.W. Kaleczyc, S.M. Johnson, W.A. Radford, and J.H. Dinan, *J. Electron. Mater*. **32**, 686 (2003).
104. A.J. Stoltz, J.D. Benson, J.B. Varesi, M. Martinka, M.J. Sperry, A.W. Kalecyzc, L.A. Almeida, P.R. Boyd, and J.H. Dinan, *J. Electron. Mater*. **33**, 684 (2004).
105. A.J. Stoltz, J.D. Benson, P.R. Boyd, M. Martinka, J.B. Varesi, A.W. Kaleczyc, E.P.G. Smith, S.M. Johnson, W.A. Radford, and J.H. Dinan, *J. Electron. Mater*. **32**, 692 (2003).
106. M. Cardona and L. Ley, Eds., *Photoemission in Solids I: General Principles.* (Berlin: Springer-Verlag,) with additional corrections, 1978.
107. J.A. Bearden and A. F. Burr, "Reevaluation of X-Ray Atomic Energy Levels," *Rev. Mod. Phys.*, 1967, **39**, 125.
108. J.C. Fuggle and N. Mårtensson, "Core-Level Binding Energies in Metals," *J. Electron Spectrosc. Relat. Phenom.*, 1980, **21**, 275.
109. Private Communication.
110. C.Y. Chang and S.M. Sze, *ULSI Technology* (New York: McGraw-Hill Inc, 1996) p. 354.
111. Private Communication.
112. R. Fedosejevs, and M.J. Brett, *Applied Optics.* **28**, 1877 (1989).
113. P.D. Desai, *J. Phys. Chem*. Ref. Data 15, 976 (1986).
114. S. de Unamuno and E. Fogarassy, *Appl. Surf. Sci.* **36**, 1 (1989).
115. R.F. Wood and G.E. Jellison, *Pulse Laser Processing of Semiconductors* (Orlando: Academic, 1984). p. 165.
116. P. Stolk, Ph.D. thesis, Universiteit Utrecht, (1993).
117. T. Aoki, and D.J. Smith, *Appl. Phys. Lett*. **82**, 2275, (2003).